THE STUDY OF THE PROXIMITY EFFECT IN Mg/Nb MULTILAYERS

A Dissertation

by

LEVICA MARGARET SMITH

Submitted to the Office of Graduate and Professional Studies of
Texas A&M University
in partial fulfillment of the requirements for the degree of

DOCTOR OF PHILOSOPHY

Chair of Committee, Donald Naugle
Committee Members, Joseph Ross
Glenn Agnolet
Haiyan Wang
Head of Department, Grigory Rogachev

May 2018

Major Subject: Applied Physics

ABSTRACT

The proximity effect in multilayers of alternating superconducting and normal materials has been studied extensively over the years on various systems due to its transport properties of the entire system. In this work, Mg/Nb multilayer thin films were investigated through experimental methods and compared to the theoretical calculations. The crystal structured was studied to observe if the films followed the bi-phase diagram.

Firstly, a study of the crystal structure of the films was attempted through X-ray diffraction (XRD) measurements. The XRD images obtained were compared with DFT calculations for Mg/Nb multilayers to check if the films fell into the expected regions of the bi-phase diagram. The XRD results were not conclusive.

Next, the resistivity of all the films was measured to study the superconducting transition temperature of each of the films. The results were compared with calculations using the Cooper-de Gennes proximity effect model. The measured transition temperatures were a good match for the calculations, which points to Cooper-de Gennes being an appropriate model for this system, as long as the films are in the Cooper limit.

The upper critical field of the films was examined both parallel and perpendicular to the film. The angular dependence of the upper critical field was also studied. Comparing the results with the theoretical calculations for 3D and 2D upper critical field, it was found that the films matched the 2D expression for the upper critical field.

To my loving husband and my awesome twin.

ACKNOWLEDGEMENTS

I would like to thank Dr. Naugle for serving as my advisor through the course of my graduate studies and for his advice and support. Many thanks to Daya and Tyler for all their help in the lab, suggestions and advice as well as many great conversations. Thanks to Minh as well for assisting with the measurements. I would like to thank my committee members Dr. Ross, Dr. Agnolet and Dr. Wang for taking the time to serve on my committee. I would like to extend my appreciation to Jin Li of Dr. Zhang's group for depositing the samples for this project, and to Lucia Steinke for running a couple samples in her He3 and DR systems.

I would like to say a special thanks to all my family and friends for all their love and support throughout this long journey.

CONTRIBUTORS AND FUNDING SOURCES

Contributors

This work was supervised by a dissertation committee consisting of Professor Donald Naugle, Dr. Joseph Ross, and Dr. Glenn Agnolet of the Department of Physics Texas A&M University, and Dr. Haiyan Wang of the Department of Materials Engineering of Purdue University.

The films for this project were grown by Jin Li of Dr. Zhang's group of the Materials Science Department. He3 and dilution refrigerator measurements were completed by Lucia Steinke of the Department of Physics.

Funding Sources

Graduate study was supported by fellowships from Texas A&M University and a fellowship from NASA Jenkins' Pre-doctoral Fellowship Program.

TABLE OF CONTENTS

LIST OF FIGURES

LIST OF TABLES

1. INTRODUCTION AND BACKGROUND*†

1.1 Superconductivity

Superconductivity was first observed in 1911 by Kamerlingh Onnes, a few years after he liquefied helium [1-4]. In superconducting metals and alloys, the electrical resistivity drops suddenly to zero when cooled to a specific temperature, known as the critical temperature T_c, also referred to as the transition temperature. Another unique characteristic of superconductors is their behavior in a magnetic field. The magnetic properties cannot be accounted for by the assumption that a superconductor is a normal conductor with zero electrical resistivity, because a bulk superconductor that is in a weak magnetic field will behave as a perfect diamagnet, with zero magnetic induction in the interior [1-6]. Meissner and Ochsenfeld (1933) found that when a sample is placed in a magnetic field in its normal state and then cooled through T_c, the magnetic flux present in the sample is ejected (Figure 1.1). This behavior is known as the Meissner effect [7]. The Meissner effect shows that a bulk superconductor when it is the superconducting state will behave as if the magnetic field is zero inside the sample, and implies that perfect diamagnetism is an essential property of superconductivity. Superconductivity can be destroyed if a sufficiently strong magnetic field, the critical field, is applied. The value of the field needed for the destruction of superconductivity is designated the $H_c(T)$ and is a function of temperature.

There are two types of superconductors: Type I and type II. Both type I and type II superconductors have similar thermal properties in zero magnetic field. The difference between

* Portions of this section are reprinted with permission from "Boundary Effects in Superconductor" by P.G. De Gennes, Rev. Mod. Phys. 36, 225 (1964), Copyright 1964 by the American Physical Society.

† Portions of this section are reprinted with permission from "Theory of the Superconducting Transition Temperature and Energy Gap Function of Superposed Metal Films" by N.R. Werthamer, Phys. Rev. 132, 2440 (1963), Copyright 1963 by the American Physical Society.

the two types is seen in the Meissner effect (Figure 1.2). Type I superconductors exhibit a complete Meissner effect up to their critical field H_c. At H_c, the field penetrates fully, and the superconductor becomes a normal metal. Type II superconductors exhibit a complete Meissner effect up to a lower critical field denoted H_{c1}. At this point, the field starts to penetrate the sample, and the sample is now in a vortex state, depicted in Figure 1.3. In the vortex state, the sample is normal inside the vortices where the field penetrates and superconducting outside the vortices. As more field is applied, the number of vortices grows and the sample is eventually saturated at a second higher critical field H_{c2}, at which point it becomes normal [1, 2, 5].

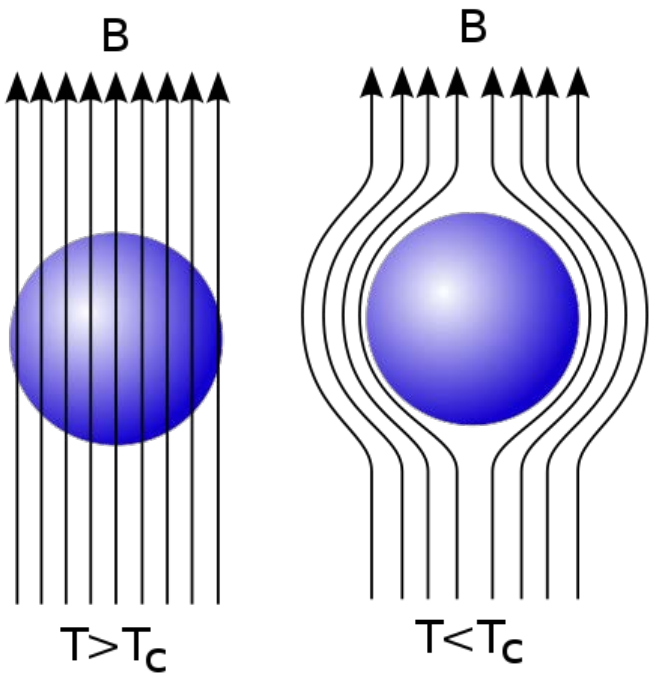

Figure 1.1: Diagram of the Meissner Effect. Magnetic field lines applied to a superconductor above its transition temperature (left) and expelled magnetic field below the transition temperature (right). Reprinted from [8].

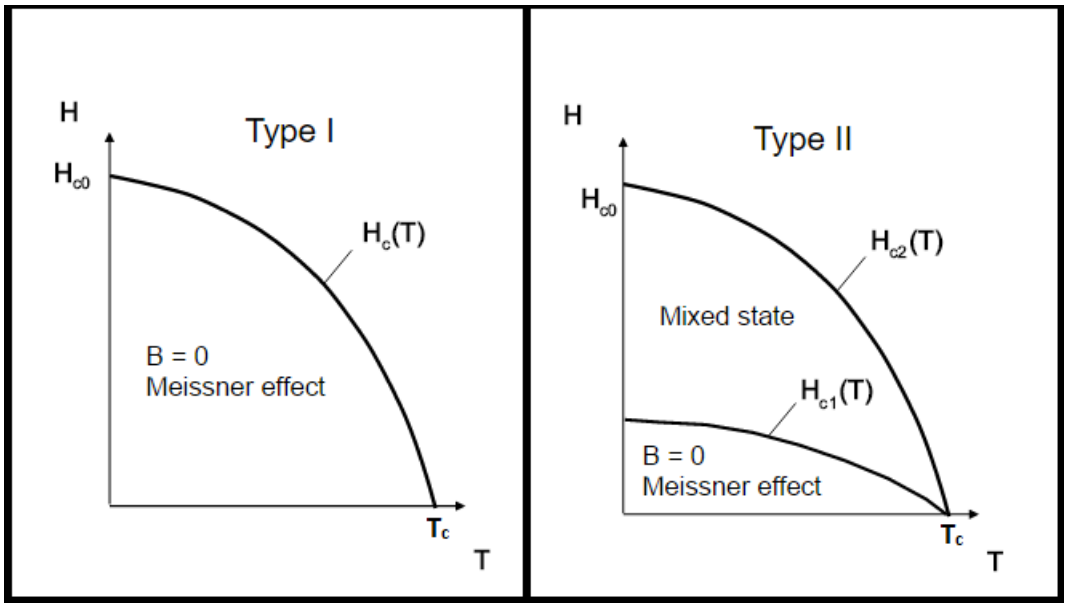

Figure 1.2: Magnetic Phase Diagram. Reprinted from [9].

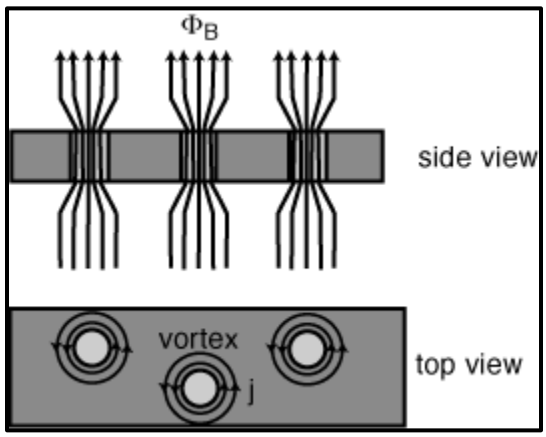

Figure 1.3: Depiction of the Vortex State. Reprinted from [10].

In 1957 Bardeen, Cooper and Schrieffer [11] proposed a theory, now known as the BCS theory, to explain the microscopic origins of superconductivity and the ordering of the electron pairs. The theory can also quantitatively predict the properties of superconductors. Cooper showed that an arbitrarily small attraction between electrons in a metal leads to a paired state of electrons having

a lower energy than the Fermi energy, which indicates that the pair is bound. These pairs, known as Cooper pairs, are formed by electron-phonon interactions where phonons are the quanta of lattice vibration energy. As an electron moves through the ion-lattice, the ions are attracted to the electron and move toward the electron causing a distortion in the lattice around the electron. This distortion creates an area of greater positive charge density around the electron. Another electron at some distance away in the lattice is then attracted to this charge distortion, a phonon. This attraction between electrons due to the displaced ions can overcome the electrons' repulsion to each other due to their negative charge, and cause them to form a Cooper pair. Cooper pairs have slightly lower energy than a single electron and can, therefore, move through the lattice relatively unaffected by thermal vibrations. This effect also causes the electrons to feel little to no resistance when traveling through the lattice, thus making the material a “perfect conductor” [1, 2, 6, 12].

In all superconductors, the entropy decreases noticeably on cooling below the critical temperature, T_c. The entropy of the superconducting state is less than that of the normal state, thus the conduction electrons are ordered at temperatures below T_c and disordered above T_c [1-4]. At temperatures well below the critical temperature, the electronic specific heat of a superconducting metal varies with temperature exponentially, $(C_{el})_S = ae^{-b/k_BT}$ where a and b are constants. This behavior suggests that electrons are excited across an energy gap. The BCS theory accounts for an energy gap which is characteristic, but not universal, of superconductors [1-5]. The Meissner effect [4] implies a magnetic susceptibility $\chi = -1/4\pi$ in the superconducting state. Ohm’s law, $j=\sigma E$, describes electrical conduction in the normal state of a metal. It is assumed that the current density is directly proportional to the vector potential **A** of the local magnetic field in the superconducting state. This leads to a modification of Ohm’s law to explain conduction and the Meissner effect in the superconducting state, **B** = curl **A**, and the constant of proportionality is

written as $-c/4\pi\lambda_L^2$. Here c is the speed of light and λ_L is a constant with the dimensions of length. Thus

$$\mathrm{j} = -\frac{\mathrm{c}}{4\pi\lambda_\mathrm{L}^2}\mathbf{A}\,. \tag{1}$$

Eqn. 1 is the London equation. It is possible to express this another way by taking the curl of both sides to obtain

$$\text{curl j}=-\frac{\mathrm{c}}{4\pi\lambda_\mathrm{L}^2}\mathbf{B}\,. \tag{2}$$

The London equation is written with the vector potential in the London gauge: div A=0, and A_n=0 on the external surface where no external current flows. The London equation leads to the Meissner effect. From a Maxwell equation $curl\,\mathbf{B} = \frac{4\pi}{c}\boldsymbol{j}$. Taking the curl of both sides gives $curl\;curl\,\mathbf{B} = -\nabla^2\mathbf{B} = \frac{4\pi}{c}\,curl\,\boldsymbol{j}$, combine with the London equation, resulting in the relations:

$$\nabla^2\mathbf{B} = \frac{1}{\lambda_L^2}\mathbf{B} \tag{3a}$$

$$\nabla^2\boldsymbol{j} = \frac{1}{\lambda_L^2}\boldsymbol{j}\,. \tag{3b}$$

From these equations, one can assume that fields and currents in superconductors can only exist within a layer of thickness λ_L. These surface currents screen the interior of the superconductor from the applied field.

$\mathbf{B}(r) = \mathbf{B}_0 =$ *constant* is not a solution of equation (3a) unless the constant $\mathbf{B}_0$ is zero. The result follows because $\nabla^2\mathbf{B}_0$is always zero, but $\mathbf{B}_0/\lambda_L^2$ is not zero unless $\mathbf{B}_0$ is zero.

The London penetration depth, λ_L, measures the depth of penetration of the magnetic field. It is a fundamental length characterizing a superconductor. Another characteristic measurement is the coherence length ξ, a measure of the distance within which the superconducting electron density cannot change drastically in an applied magnetic field [1-5]. Both λ_L and ξ are temperature-dependent quantities and their ratio, $= \frac{\lambda_L}{\xi}$, is another way to distinguish between type I and type II superconductor.

1.2 Proximity Effect

There has been significant interest over the years in the study of the superconducting proximity effect. A common type of sample used for studying the proximity effect is layered films of alternating superconducting and normal materials, called bilayers. A bilayer is formed from one layer of each material. A multilayer is a unit of repeated bilayers (Figure 1.4). The proximity effect is possible due to the Cooper pairs being able to maintain their coherence over macroscopic distances from the superconducting material into a normal metal that is in close proximity, as long as there is good electrical contact between the two materials.

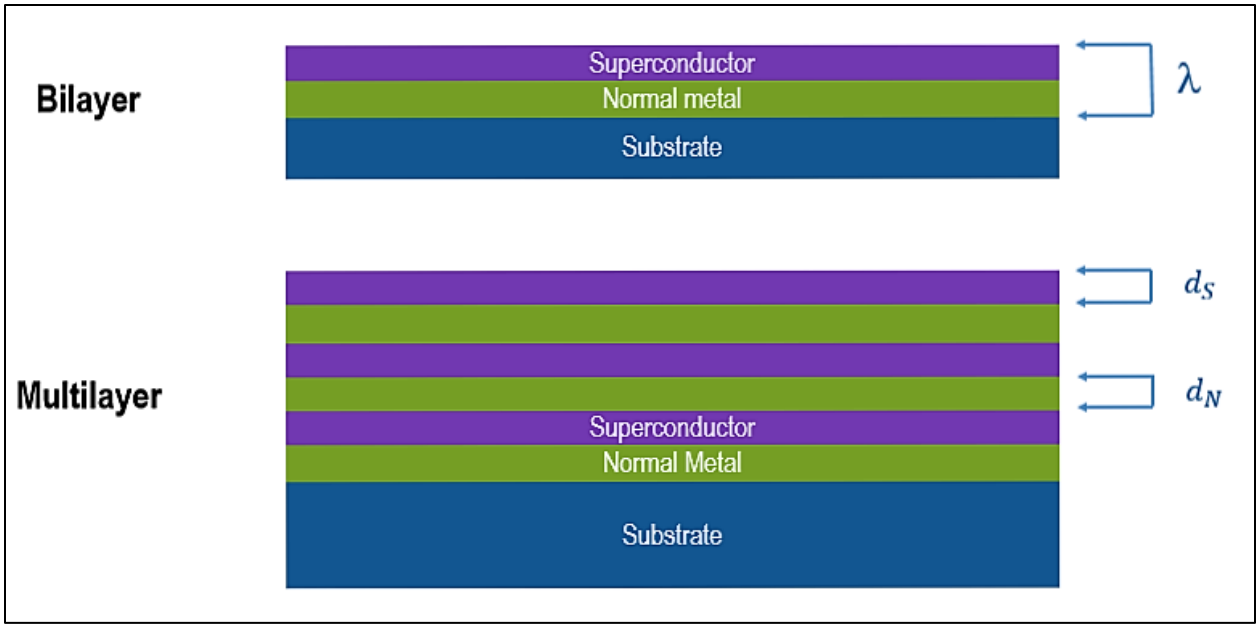

Figure 1.4: A representation of a bilayer and a multilayer. λ is the bilayer thickness, d_N and d_S are the thicknesses of the normal and superconducting metal slabs respectively.

Several authors have composed theoretical explanations of the proximity effect phenomenon [13-19]. The approach that is common among the authors is assuming the superconductivity in the bulk state is characterized by an electron pair correlation with an associated coherence length, and this correlation extends a similar length into a normal metal that is in contact with the superconductor, which has an assumed coherence length in most cases. It then becomes possible that superconducting films of thicknesses, d_S, less than or comparable to the characteristic coherence length of the superconductor, ξ_S, will have their transition temperature lowered by superposition of a normal metal. This lowering should be independent of the normal metal thickness, d_N, when d_N is larger than the coherence length of the normal metal, ξ_N. For d_S much smaller than ξ_S, T_c falls rapidly below experimental detection as d_N approaches ξ_N.

Besides a new T_c, the multilayers also acquire a new upper critical field. When the bilayer thickness is reduced to the nanometer scale, the multilayers exhibit interesting transport and

mechanical properties, as well as structural transitions resulting in the adoption of a crystal structure differing from the bulk form.

Several groups have studied the structure and superconductivity of various multilayers, such as Nb/Zr, Nb/Ta, Nb/Pd, etc., where the bilayer thicknesses (λ) of each metal varied [20-27]. These groups used either the Cooper-de Gennes proximity effect model or the de Gennes-Werthamer proximity effect model to calculate the critical temperature for the multilayers. Both of these models were based on the theory first introduced by Cooper (described in the following sections). A few groups also studied the crystal structure changes that occurred in some of the multilayer systems. They observed stabilization of metastable phases in which the materials adopted a crystal structure different from their bulk [28]. Recently groups have been studying the stabilization of metastable phases in magnesium (Mg) multilayer systems as well as the effects of layering magnesium with niobium (Nb), a type II superconductor, to improve the properties of magnesium. Magnesium, which in its bulk state has a hexagonal closed packed, hcp, crystal structure, has been observed to adopt a body centered cubic, bcc, crystal structure when layered with niobium, when the thicknesses of each are in a certain range. In a bcc crystal structure, Mg's mechanical properties could be improved [29, 30].

For this study, the proximity effect in Mg/Nb multilayer thin films was examined. This multilayer system, while having been studied for improving the properties of Mg, has not been previously studied for the proximity effect. The dependence of the critical temperature and upper critical field of the multilayers on varying the Mg/Nb ratio within the bilayer was investigated. Resistivity and magnetoresistance measurements on a variety of Mg/Nb multilayer compositions were performed with a Quantum Design Physical Property Measurement System (PPMS). A Quantum Design Dynacool helium 3 system was also used for a few resistivity measurements.

X-ray diffraction (XRD) measurements were used to study the crystal structure of the films. The results were compared to previous findings found by the group in reference 29.

In the next few sections I introduce the Cooper proximity effect model, the Cooper-de Gennes proximity effect model and the de Gennes-Werthamer proximity effect model and discuss the significance of each.

1.3 Cooper Model

Cooper considered a simple case [31] where all electron-electron interactions in the normal metal are negligible. The penetration length of the Cooper pairs, K^{-1}, has been determined for two different cases:

1) If the normal metal (N) is "clean", i.e., if the mean free path l_N in N is large compared to the coherence length ξ_N, then the probability amplitude $F = \langle \psi_\uparrow \psi_\downarrow \rangle$ for finding the Cooper pair at distance $|x|$ from the N-S boundary has the asymptotic form

$$F = \phi(x) \exp(-K|x|) \qquad (|x| large) \tag{4}$$

where $\phi(x)$ is a slowly varying function of x and $K^{-1} = \hbar v_N / 2\pi k_B T$ where v_N is the Fermi velocity in the normal metal and T is the temperature. When T goes toward 0, the decrease of F is not exponential anymore, but becomes very slow [6]:

$$F = const. \frac{1}{x + x_1} \tag{5}$$

where x_1 is some distance from x.

2) If N is "dirty" ($l_N < \xi_N$), the pair leakage is controlled by a diffusion process. A diffusion constant is introduced $= \frac{1}{3} v_N l_N$. The probability amplitude formula still holds, but now

$$\xi_N = (\hbar D / 2\pi k_B T)^{1/2} = \left(\frac{\hbar v_N l_N}{6\pi k_B T}\right)^{1/2}. \quad (6)$$

In the limit where both N (normal metal) and S (superconductor) are both "dirty" and thin (compared with ξ_N), Cooper made an argument that each electron spends a fraction of its time in N, $n_N d_N/(n_N d_N + n_S d_S)$.Thus, an average coupling constant can be defined as

$$(\mathrm{nV})_{\mathrm{eff}} = \frac{\mathrm{n_N V_N d_N + n_S V_S d_S}}{\mathrm{n_N d_N + n_S d_S}} \quad (7)$$

where $n_{S,N}$ is the density of states for the metals, and $V_{S,N}$ is the coupling constant [6, 30, 31].

1.4 Cooper-de Gennes Proximity Effect Theory

De Gennes assumed the excitation spectrum of a superconducting system is constructed by the self-consistent field method [13]. He also assumed that the electrons are coupled by a point interaction $-V(r_i)\delta(r_i - r_j)$. This is an appropriate approximation since the range of the exact interaction is of the order of the Fermi wavelength, while the effects take place at a much larger

scale. V(r) will not be the same in the N and S regions. In the S regions, $V=V_S$ is positive (attractive interaction). In the N regions, $V=V_N$ may be either positive or negative, depending on the balance between Coulomb repulsion and phonon induced attraction.

To derive Fermi-type excitations, De Gennes started with the equation for the one-electron operator $\psi_\alpha^+(r)$

$$i\frac{\partial\psi_\alpha^+}{\partial t}(r) = \left[\frac{p^2}{2m} + U(r)\right]\psi_\alpha(r) - V(r) \times \sum_\beta \psi_\alpha^+(r)\psi_\beta^+(r)\psi_\beta(r) \tag{8}$$

where α and β are spin indices and U is the one-electron potential, with different values in the two metals. De Gennes then linearized the last term according to the rule

$$V_n\psi_\alpha^+(r)\psi_\beta^+(r)\psi_\beta(r) \to V_n\langle\psi_\alpha^+(r)\psi_\beta^+(r)\rangle\psi_\beta(r)\,. \tag{9}$$

The only non-vanishing terms come from

$V_n(r)\langle\psi_\downarrow^+(r)\psi_\uparrow^+(r)\rangle = -V_n(r)\langle\psi_\uparrow^+(r)\psi_\downarrow^+(r)\rangle = \Delta^+(r)$, which is the pair potential.

The eigenmodes of the linearized equation are

$$\psi_\uparrow(rt) = \sum_n\left(u_n(r)e^{-iE_nt}\gamma_{n\uparrow} + v_n^+(r)e^{iE_nt}\gamma_{n\downarrow}^+\right) \tag{10}$$

$$\psi_\downarrow(rt) = \sum_n\left(u_n(r)e^{-iE_nt}\gamma_{n\downarrow} - v_n^+(r)e^{iE_nt}\gamma_{n\uparrow}^+\right) \tag{11}$$

where γ is a fermion operator, and the excitation energy E_n is restricted to positive values. $u\ and\ v$ are the eigenfunctions of the following system of equations:

$$Eu = \left[\left(\frac{1}{2m}\right)p^2 + U(r)\right]u + \Delta v \tag{12}$$

$$Ev = -\left[\left(\frac{1}{2m}\right)p^2 + U(r)\right]v + \Delta^{+}u \ . \tag{13}$$

The fermion states g of energy E_n have a thermal equilibrium population given by the Fermi function $f(E_n) = 1/[1 + \exp(E_n/T)]$. This gives

$$\Delta(r) = V(r)\langle\psi_{\uparrow}(r)\psi_{\downarrow}(r)\rangle = V(r) \times \sum_n v_n^{+}(r)u_n(r)[1 - 2f(E_n)] \ . \tag{14}$$

To ensure the convergence of this equation, when the excitation energy ϵ_n is higher than ω_D the local Debye frequency, the interaction V is cut off, in agreement with the BCS theory. The pair potential $\Delta(r)$ is space-dependent for both standard variations of $\Delta(r)$ in an N-S sandwich and in an SNS junction. The space dependence has a significant consequence: the eigenfunctions $u_n(r)$ and $v_n(r)$ are not proportional to the one electron wave functions in the normal state $w_n(r)$ defined by $[p^2/2m\ + U(r)]w_n = \epsilon_n w_n$.

The pair potential $\Delta(r)$ is a natural "order parameter" for the inhomogeneous systems. De Gennes realized that this was not the only possible choice. He determined that one could also use the "condensation amplitude" F(r) defined by $F(r) = \langle\psi_{\uparrow}(r)\psi_{\downarrow}(r)\rangle$. F is the probability amplitude of finding two electrons in the condensed state at point r. There are two important properties in connection with $\Delta\ and\ F$.

(a) Boundary conditions: on an atomic scale, $F(r)$ and $\Delta(r)$ are continuous functions of r. But if the interest is in a larger scale and the interface between two metals is described as a sharp boundary, neither $F\ and\ \Delta$ are continuous on this surface. For dirty systems, the continuous quantity is $F(r)/N(r) = \Delta(r)/n(r)V(r)$, where $n(r)$ is the local density of states at the Fermi level.

(b) The relation between the pair potential and the energy gap E_0: E_0 was defined as the lowest excitation energy of the fermions in the self-consistent field Δ.

When $\Delta(r)$ depends on only one space coordinate X, the energy gap E_0 is equal to the minimum value of $|\Delta(X)|$ in the sample.

Based on Gor'Kov's treatment of superconductivity, $\Delta(r)$ may be written as

$$\Delta(r) = V(r)\sum_{\omega}\int dr'\Delta(r')H_{\omega}(rr') \tag{15}$$

where,

$$H_{\omega}(rr') = T\sum_{\omega}\sum_{nm}\frac{1}{\epsilon_n - i\omega}\frac{1}{\epsilon_m + i\omega} \times w_n^{+}(r)w_m^{+}(r)w_n(r')w_m(r') \tag{16}$$

where $\omega = 2\pi T(v + \frac{1}{2})$ and the sum Σ_{ω}represents the sum over all integers v. The functions w_n are the one-electron wave functions in the normal state. They include the effects of impurity and boundary scattering. From the orthogonality of the real functions

$$\int H_{\omega}(rr')dr' = \sum_n \frac{1}{\epsilon_n + \omega^2}|w_n(r)|^2 = n(r)\int\frac{d\epsilon}{\epsilon^2 + \omega^2} = \frac{\pi}{|\omega|}n(r) \tag{17}$$

where $n(r)$ is the local density of states. The one dimensional Fourier transform, where the pair potential depends only on one space coordinate ($\Delta(X)$), is

$$H_\omega(XX') = \frac{1}{2\pi}\int H_\omega(q)e^{iq(X-X')}dq = \left(\frac{\pi n}{2|\omega|\xi_\omega}\right)e^{-\frac{|X-X'|}{\xi_\omega}} \quad . \tag{18}$$

$\xi_\omega = (D/2|\omega|)^{\frac{1}{2}}$ (where $D = \frac{1}{3}v_F l$, l is the mean free path) gives the range of $H_\omega(XX')$.

The largest range corresponds to $\omega = \omega_0 = \pi T$, $\xi_{\omega_0} = \xi = (D/2\pi T)^{\frac{1}{2}}$, where ξ is the coherence length for the alloy. (The dirty superconductor approximation requires $l \ll \xi$). In a two-layer system, De Gennes assumed that the thicknesses $d_N \; and \; d_S$ of the slabs are much smaller than the respective coherence lengths $\xi_N(T) \; and \; \xi_S(T)$, $d_N \ll \xi_N$ and $d_S \ll \xi_S$. This is the Cooper limit. Then the kernel $H_\omega(XX')$ is essentially constant when $X \; or \; X'$ is varied in one of the slabs. From eqn. (17) and the boundary condition $\left[{n_A}/{(\xi_B + \alpha\xi_A)}\right] = \left[{n_B}/{(\xi_A + \alpha^{-1}\xi_B)}\right]$, $\alpha = {n_A}/{n_B}$, de Gennes derived the following set of equations:

$$d_N H_\omega(NN) + d_S H_\omega(NS) = n_N(\pi/|\omega|), \quad d_N H_\omega(SN) + d_S H_\omega(SS) = n_S(\pi/|\omega|), \tag{19}$$

$$H_{NN}/n_N = H_{NS}/n_S, \quad H_{SN}/n_N = H_{SS}/n_S \; .$$

These give

$$\frac{H_\omega(NS)}{n_N n_S} = \frac{H_\omega(NN)}{n_N^2} = \frac{H_\omega(SS)}{n_S^2} \;\; \frac{\pi}{|\omega|} \frac{1}{n_N d_N + n_S d_S} \quad . \tag{20}$$

Since $\Delta(X)$ will be constant for each slab in the limit,

$$\Delta_N = \sum_\omega V_N T \frac{\pi}{|\omega|} \frac{1}{n_N d_N + n_S d_S} (n_N^2 d_N \Delta_N + n_N n_S d_S \Delta_S) \tag{21}$$

$$\Delta_S = \sum_\omega V_S T \frac{\pi}{|\omega|} \frac{1}{n_N d_N + n_S d_S} (n_N n_S d_N \Delta_N + n_S^2 d_S \Delta_S) \quad . \tag{22}$$

A non-trivial solution for eqns. (21) and (22) is needed. De Gennes considered the result for only the case where the frequency cutoff ω_0 is the same in N and S.

$$T \sum_\omega \frac{\pi}{|\omega|} \rightarrow log \frac{1.14\omega_0}{T} = \frac{1}{\rho} \tag{23}$$

$$T_{cNS} = \frac{\Theta_D}{1.45} exp \left[\frac{-1}{[n(E_F)V]_{eff}} \right] \tag{24}$$

$$\rho = [n(E_F)V]_{eff} = \frac{V_N n_N^2 d_N + V_S n_S^2 d_S}{n_N d_N + n_S d_S} \quad . \tag{25}$$

T_{cNS} is the critical temperature of the bilayer and ρ is the effective attraction parameter 'nV' in the BCS formula for T_c [13]. Qualitative agreement for the Cooper-de Gennes model with experimental data can be obtained as long as one keeps in mind that the formulas are valid only for the Cooper limit, d_S and d_N, both much smaller than the coherence distance, i.e. for very thin films.

1.5 De Gennes-Werthamer Proximity Effect Theory

Werthamer [15] refined the de-Gennes model for films that do not fall into the Cooper limit $d_N \ll \xi_N$ and $d_S \ll \xi_S$. The de Gennes-Werthamer model relates the transition temperature of the bilayer to the bulk parameters of the bilayer constituents. Werthamer adopted the equation of de Gennes and Guyon [14] for the energy gap function at the transition temperature of the sandwich

$$\Delta(\mathbf{r}) = \int d^3r'\, K(\mathbf{r},\mathbf{r}')\Delta(\mathbf{r}') \tag{26}$$

where the kernel K depends on the bulk properties of the sandwich component specified by $\mathbf{r}$ and $\mathbf{r}'$

$$K(\mathbf{r},\mathbf{r}') = N(0)V(\mathbf{r})\left[\ln\left(\frac{1.14\theta_D}{T_c}\right)\delta^3(\mathbf{r},\mathbf{r}') - X(\mathbf{r},\mathbf{r}')\right] \tag{27}$$

$$X(\mathbf{r},\mathbf{r}') = (2\pi)^{-3}\int d^3k e^{i\mathbf{k}\cdot\mathbf{r}}\chi(\hbar v_F l k^2/6\pi k_B T_c) \tag{28}$$

$$\chi(z) = \psi\left(\frac{1}{2}+\frac{1}{2}z\right) - \psi\left(\frac{1}{2}\right) \tag{29}$$

with ψ being the digamma function. Werthamer rewrote the Eqn. (26) as

$$\Delta(\mathbf{r}')\ln\left[\frac{T_c(\mathbf{r}')}{T_c}\right] = \int d^3\mathbf{r}'' X(\mathbf{r}'-\mathbf{r}'')\Delta(\mathbf{r}'') \tag{30}$$

where $T_c(\mathbf{r})$ is the local bulk transition temperature and has been defined by

$$[N(0)V(r)]^{-1} = \ln\left[\frac{1.14\theta_D}{T_c(\mathbf{r})}\right]. \tag{31}$$

Next Werthamer introduced the function $\tilde{X}(r)$,

$$\tilde{X}(r) = (2\pi)^{-3}\int d^3k e^{i\mathbf{k}\cdot\mathbf{r}}\chi^{-1}(\xi^2k^2) \tag{32}$$

with $\xi^2 = \hbar v_F l/6\pi k_B T_c$. Multiplying Eqn (30) on both sides by $\tilde{X}(\mathbf{r}-\mathbf{r}')$ integrating over **r'**,

$$\Delta(\mathbf{r}) = \int d^3\mathbf{r}'\tilde{X}(\mathbf{r}-\mathbf{r}')\ln[T_c(\mathbf{r}')/T_c]\Delta(\mathbf{r}')\,. \tag{33}$$

Werthamer recognized that $\tilde{X}(r)$is just the Green's function for the differential operator $\chi(-\xi^2\nabla^2)$, which enabled him to transform Eqn. (32) into the differential form

$$\chi(-\xi^2\nabla^2)\Delta(\mathbf{r}) = \ln\left[\frac{T_c(\mathbf{r})}{T_c}\right]\Delta(\mathbf{r})\ . \tag{34}$$

Since Eqn. (34) looks very much like a Schrodinger equation, a direct mathematical correspondence can be made with the quantum motion of a particle of energy E in a potential U(**r**). The following substitutions were then made: $U(\boldsymbol{r}) \rightarrow \ln \theta_D / T_c(\mathbf{r})$, $E \rightarrow \ln \theta_D / T_c$, $k^2/2m \rightarrow \chi(\xi^2 k^2)$. Werthamer then focused on the case of two superposed thin films, one a known superconductor,

$$T_c(r) = T_{cS},\ 0 < x \leq d_S \tag{35a}$$

and one a normal, non-superconducting, metal assumed to have a non-vanishing attractive electron-electron interaction, and thus a small but non-vanishing transition temperature,

$$T_c(r) = T_{cN},\ -d_N \leq x \leq 0\ . \tag{35b}$$

Solutions of Eqn. (34) can be written as:

$$\Delta(\mathbf{r}) = e^{\pm i k_S x},\ \ 0 < x \leq d_S\ ,\ \Delta(\mathbf{r}) = e^{\pm i k_N x},\ \ -d_N \leq x \leq 0 \tag{36}$$

where $k_{s,n}$ satisfies

$$\chi(\xi^2 k_S^2) = \ln T_{cS}/T_c\ ,\ \ -\chi(-\xi^2 k_N^2) = \ln T_c/T_{cN}\ . \tag{37}$$

To choose appropriate boundary conditions, Werthamer required that $d\Delta(\mathbf{r})/dx$ vanish at metal-insulator or metal-vacuum surfaces, here at $x = d_S$ and $x = -d_N$. At the metal-metal interface,

$\Delta(\mathbf{r})$ cannot be continuous or have a continuous first derivative because $\Delta(\mathbf{r})$ is proportional to V($\mathbf{r}$) and is thus discontinuous. Conversely, $\Delta(\mathbf{r})/V(\mathbf{r})$ is directly proportional to the Gor'kov Green's function; therefore $d\Delta/\Delta dx$ is continuous. Applying all the boundary conditions led to

$$\Delta(x) \propto V_S \cos k_S(x - d_S)/\cos k_S d_S \ , \quad 0 < x \leq d_S$$

$$\Delta(x) \propto V_N \cosh k_N(x + d_N)/\cosh k_N d_N \ , \quad -d_N \leq x \leq 0 \tag{38}$$

and

$$k_S \tan k_S d_S = k_N \tanh k_N d_N \ . \tag{39}$$

Equations (29), (37), and (39) are sufficient to determine T_c of the N-S sandwich [15].

It can be seen in literature that the Cooper-de Gennes model works well for very thin multilayers due to the use of the Cooper limit in its derivation [20-22]. For multilayer films that do not follow the Cooper limit, de Gennes-Werthamer model appears to work well [23-27].

1.6 Upper Critical Field in Layered Structures

Besides seeing changes in the critical temperature, another interesting study is the behavior of the upper critical field H_{c2} due to the proximity effect [32-43]. The temperature dependence of the perpendicular upper critical field, $H_{c2\perp}(T)$, gives important information about the microstructure and about the nature of superconductivity in layered structures. The temperature dependence of the critical field parallel to the plane of the layers, $H_{c2\parallel}(T)$, shows dimensional crossover behavior.

Due to the decrease of the perpendicular coherence length, $\xi_\perp$, as the temperature is cooled below the critical temperature T_c, $H_{c2\parallel}(T)$ changes its temperature dependence from a three-dimensional (3D) behavior at temperatures near the T_c, to two-dimensional (2D) behavior at temperatures well below the transition. The peculiarities of this crossover strongly depend on the strength and nature of the interaction between the superconducting layers. When $\xi_\perp$ is approximately equal to the thickness of the normal metal, d_N, the 2D-3D crossover occurs. When $\xi_\perp \gg d_N$ the superconducting layers are coupled, and a 3D behavior is expected. If, instead, $\xi_\perp \ll d_N$ the superconducting layers are decoupled, and a 2D behavior is predicted if the coherence length of the superconducting material, ξ_S, is smaller than its thickness d_S.

A popular theory to consider for explaining the behavior of the perpendicular upper critical field in S/N multilayers is the Biagi, Kogan, and Clem (BKC) theory [37]. The expression for $H_{c2\perp}(T)$ is

$$q_S \tan\left(\frac{q_S d_S}{2}\right) = q_N \tanh\left(\frac{q_N d_N}{2}\right) \tag{40}$$

where:

$$q_S^2 = k_S^2 - (2\pi H_{c2\perp})/\phi_0 \tag{41}$$

$$q_N^2 = k_N^2 + (2\pi H_{c2\perp})/\phi_0 \tag{42}$$

$$k_S^2 = 2\pi T y(t_S)/\hbar D_S \tag{43}$$

$$k_N^2 = -2\pi T y(t_N)/\hbar D_N \tag{44}$$

$$t_{S,N} = T/T_{S,N} \tag{45}$$

$$\ln t = \psi\left(\frac{1}{2}\right) - \psi\left(\frac{1}{2} + \frac{y(t)}{2}\right) \tag{46}$$

where $\psi(x)$ is the digamma function. At the critical temperature of the multilayer T_c, $H_{c2\perp} = 0$ and $q_{S,N}^2 = k_{S,N}^2$.

According to the Ginzburg-Landau theory, the parallel critical field near the T_c of a three-dimensional (3D) anisotropic superconductor is given by:

$$H_{c\parallel}(T) = \frac{\phi_0}{2\pi\xi_\parallel(T)\xi_\perp(T)} \tag{47}$$

where ϕ_0 is the superconducting flux quantum and $\xi_\parallel$ and $\xi_\perp$ are the coherence lengths parallel and perpendicular, respectively, to the layers.

Tinkham [35] calculated the parallel upper critical field for a thin two-dimensional (2D) film:

$$H_{c\parallel}(T) = \frac{\sqrt{12}\phi_0}{2\pi\xi_\parallel(T)d_S} \tag{48}$$

where $\xi_\parallel$ and $\xi_\perp$ are given by:

$$\xi_\parallel = \left[\frac{\phi_0}{2\pi H_{c2\perp}}\right]^{1/2} \tag{49}$$

$$\xi_{\perp} = \left[\frac{\phi_0 H_{c2\perp}}{2\pi H_{c2\parallel}^2}\right]^{1/2} . \tag{50}$$

Another way to observe the 3D-2D crossover is to examine the angular dependence of the upper critical field. For a 3D anisotropic superconductor, the angular dependence of H_{c2} is described by [32, 33, 36]

$$H_{c2}(T,\theta) = \frac{H_{c2\perp}(T)}{[(m/M)\sin^2(\theta)+\cos^2\theta]^{1/2}} \tag{51}$$

where,

$$\frac{M}{m} = \left[\frac{H_{c2\parallel}(T)}{H_{c2\perp}(T)}\right]^2 \tag{52}$$

and where θ is the angle between the field direction and the sample normal. The angular dependence for the 2D case is given by [35]

$$\left|\frac{H_{c2}(T,\theta)\cos\theta}{H_{c2\perp}(T)}\right| + \left[\frac{H_{c2}(T,\theta)\sin\theta}{H_{c2\parallel}(T)}\right]^2 = 1 \ . \tag{53}$$

2. SAMPLE FABRICATION AND EXPERIMENTAL TECHNIQUES

2.1 Magnetron Sputtering

One of the most common ways to prepare thin film samples is by the process of sputtering which is a physical vapor deposition (PVD) process used for depositing materials onto a substrate. Deposition occurs in a high vacuum environment by ejecting atoms from the target materials and condensing the ejected atoms onto a substrate.

The samples for this study were prepared via DC magnetron sputtering by a fellow research group. Magnetron sputtering [44-46] is a plasma vapor deposition process (Figure 2.1). Sputtering is a process in which a plasma is created by placing a DC voltage between a target and a substrate. Positively charged ions (typically argon) from the plasma are accelerated by an electrical field applied to the negatively charged electrode, designated the target. The negatively charged target attracts the positive ions at a high velocity. The accelerated ions strike the negative electrode with enough force to dislodge and eject atoms from the target. These atoms are then ejected in a typical line-of-sight distribution from the surface of the target, condense on the substrate and start to form a film. Electrons released during ionization are accelerated to the substrate. They subsequently collide with other plasma atoms, creating more ions and free electrons in the process, which will strike the target, continuing the cycle. The substrate is attached to a rotary unit which spins the substrate at a specified speed. Substrate rotation helps with the uniformity of the deposited films. In general, sputter guns are not directly facing the substrate; they have a certain angle, normally 10 - 30 degree. Rotation speeds of the substrate are 60-100 rpm.

Magnetron sputtering deposition uses a strong transverse magnetic field, normal to the electric field, near the target. This magnetic field causes traveling electrons to spiral along magnetic flux

lines near the target instead of being attracted toward the substrate, which leads to higher sputter rates. The sputtered atoms are neutrally charged and are thus unaffected by the magnetic trap. The advantage of this is that the plasma is trapped to an area near the target. This helps increase the efficiency of the sputtering process, and minimizes both impurities that form in the thin-film and damage to the film caused by stray electrons and ions. Magnetron sputtered films exhibit better adhesion to the substrate than evaporated films due to the higher kinetic energy and lower pressures that can be used.

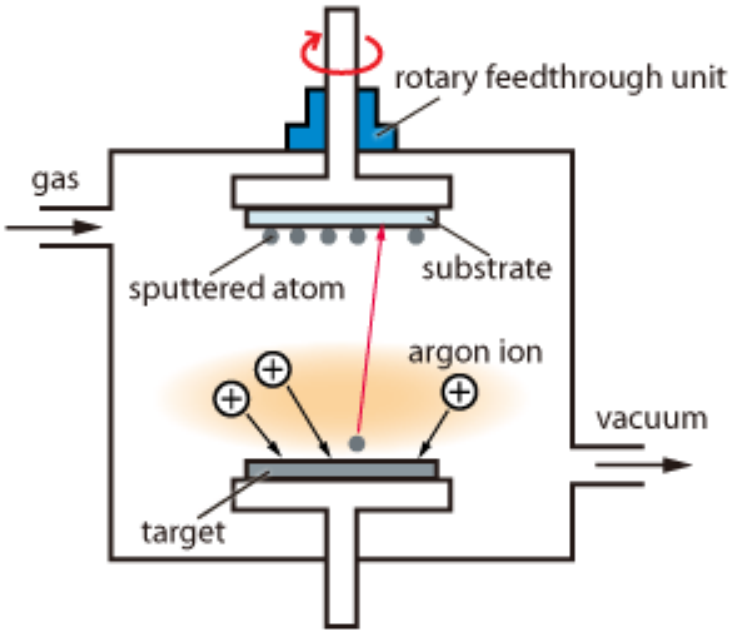

Figure 2.1: Diagram of the sputtering process. Reprinted from [47].

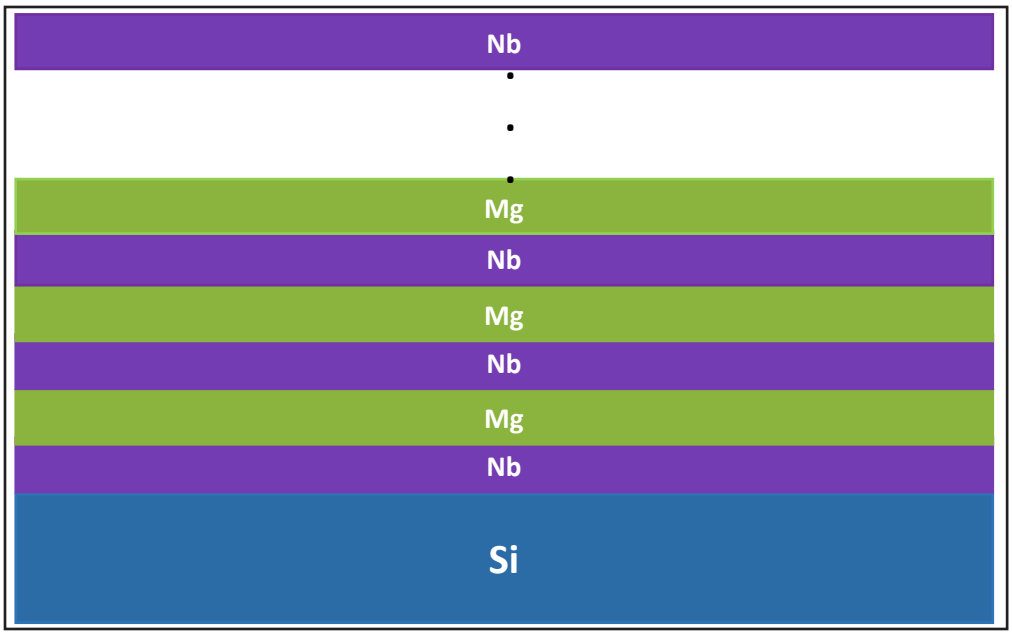

Figure 2.2: A representation of the film growth order.

For this study, multilayer films composed of magnesium and niobium were examined. The individual layer thicknesses varied from 0.20 to 5.00 nm and overall thickness varied from 50.00 to 80.00nm. The four types of substrates used were hydrofluoric (HF) acid etched single crystal silicon Si (111), Si (110), Si (100), and SiO_2 (without HF acid etch). The multilayer films were deposited on the silicon substrates via DC magnetron sputtering at room temperature from pure Mg (99.95%) and Nb (99.95%) targets. A base pressure of better than 8×10^{-8} torr was achieved before deposition, and the argon (Ar) pressure during deposition was 2~3 mtorr. Prior to deposition, all targets were pre-sputtered to clean the surface of the target itself from contamination. Multilayers were deposited by alternately sputtering the two targets, Mg and Nb. The first layer was niobium, then a layer of magnesium was deposited. These two layers were repeated until the final desired thickness was achieved. A 3.00 nm-thick Nb cap layer was then deposited after the deposition of the Mg and Nb layers to help reduce oxidation (Figure 2.2). The

sputter rate (nm/s) was determined before the depositions to control the layer thickness by adjusting deposition time and power. Good uniformity (of the films) was achieved by rotating the stage. Thus the group was able to control the layers very precisely. The deposition rate of a target gradually decreases as the target is gradually used up, and so the sputter rate was monitored from time to time. These films were prepared using a custom-built magnetron sputtering system, shown in Figure 2.3. To determine the sputter rate vs texture, the group used the diagram shown in Figure 2.4 which relates the sputter rate to the energy flux [48]. Thicknesses used for calculations were the thicknesses reported by Dr. Zhang's group. Due to the thinness of the individual layers and the potential crystal structure change there is possibly some error in the reported thicknesses.

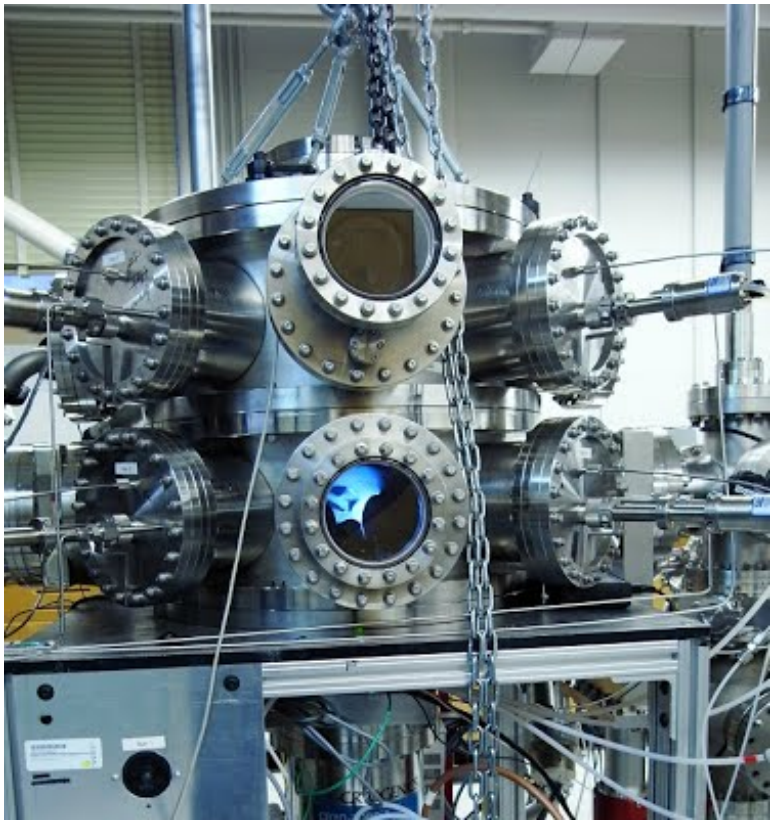

Figure 2.3: DC Magnetron Sputter System belonging to Dr. Zhang's group. Reprinted from [49]

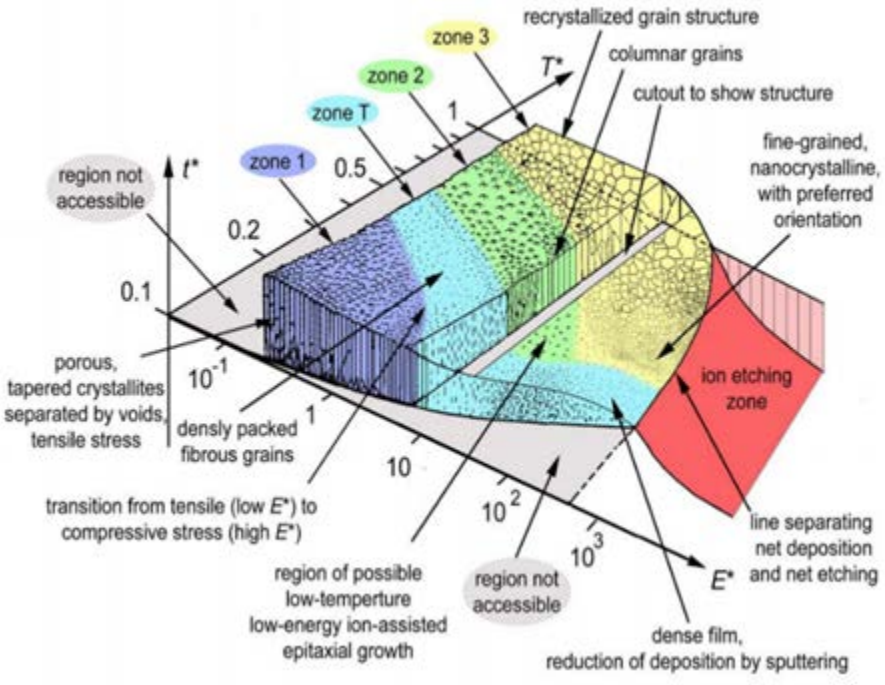

Figure 2.4: Structure zone diagram applicable to energetic deposition as a function of the generalized temperature T^* and the normalized energy flux E^*; t^* represents the net thickness. The boundaries between zones are gradual and for illustration only. Reprinted from [48].

2.2 Sample Preparation

Once the films were deposited onto the Si substrates, I used a diamond scriber pen to cut small rectangular pieces to fit inside the sample puck for measurement. The cut pieces were then covered with a mask and placed inside the in-house evaporation chamber shown in Figure 2.5. A 4nm chromium film was deposited onto the pieces to act as an adhesive layer, then 40nm of silver (Ag) was deposited on top of the chromium to form four contact pads on the samples. This deposition was done by thermal evaporation. Thermal evaporation, a PVD method, occurs when a source material is heated above its melting point via resistive heating. This process must take place in a high vacuum environment to minimize the amount of collisions between gas particles and the

source atoms that are being evaporated. This allows the vapor particles to travel in a straight path until they reach the substrate, where they condense into the film.

The samples were taken out of the evaporator and gold leads were attached. Small squares of indium were pressed to each of the contact pads, gold wires were pressed onto the indium pieces, and then another piece of indium was pressed on top of the wire to secure it.

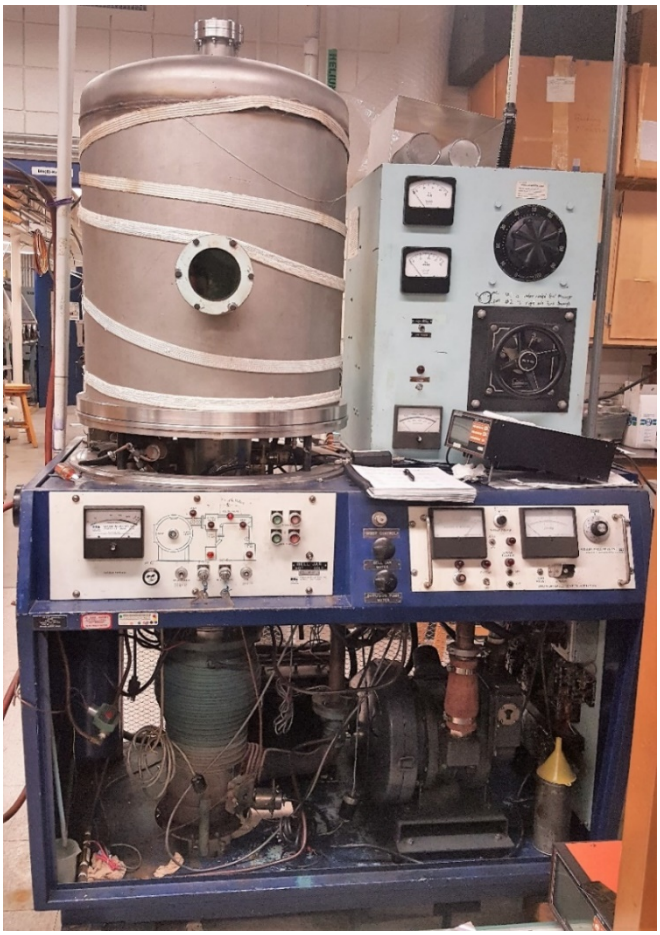

Figure 2.5: In-house Vacuum Technologies Evaporator System

In this study, low temperature resistivity experiments were conducted using a Quantum Design model 6000 Physical Property Measurement System (PPMS), as well as a Quantum Design Dynacool helium 3 system. After leads were attached to the samples, the samples were placed on a PPMS resistivity puck (Figure 2.6a) and the gold wires were soldered to the puck, which was then placed in the PPMS for measurement. To obtain the critical field measurements the samples were attached to a PPMS rotator puck and rotated 0^o to 180^o (Figure 2.6b). Figure 2.7a is an image of the PPMS system in my lab. A schematic of the PPMS is shown in Figure 2.7b.

The PPMS operates in a temperature range of 1.7 Kelvin (K) to 400K with a superconducting solenoid magnet that has a range of ±9 Tesla (T) [50]. To minimize the cryogen boil-off, the liquid helium (He) environment is enclosed in a vacuum jacket with several layers of radiation shields. The probe, which houses the sample chamber where the sample puck is placed for measurement, is composed of several concentric stainless steel tubes and other components (Figure 2.7b). The probe is immersed in the liquid He bath inside the dewar. The outer layer of the probe, an evacuated region filled with reflective superinsulation, isolates the sample chamber from the liquid He bath. Liquid He is transferred to the cooling annulus through a series of capillaries in a controlled fashion to cool the sample space. An electronic control unit monitors the sample temperature with a series of thermometers attached to the sample space; it heats and cools the sample space until the sample temperature stabilizes. A platinum thermometer reads temperatures above 80K, while a negative temperature coefficient (NTC) thermometer reads temperatures below 100K. A weighted average of the two is used in the crossover region. The 9T superconducting magnet is maintained at 4.2K by immersion in liquid helium.

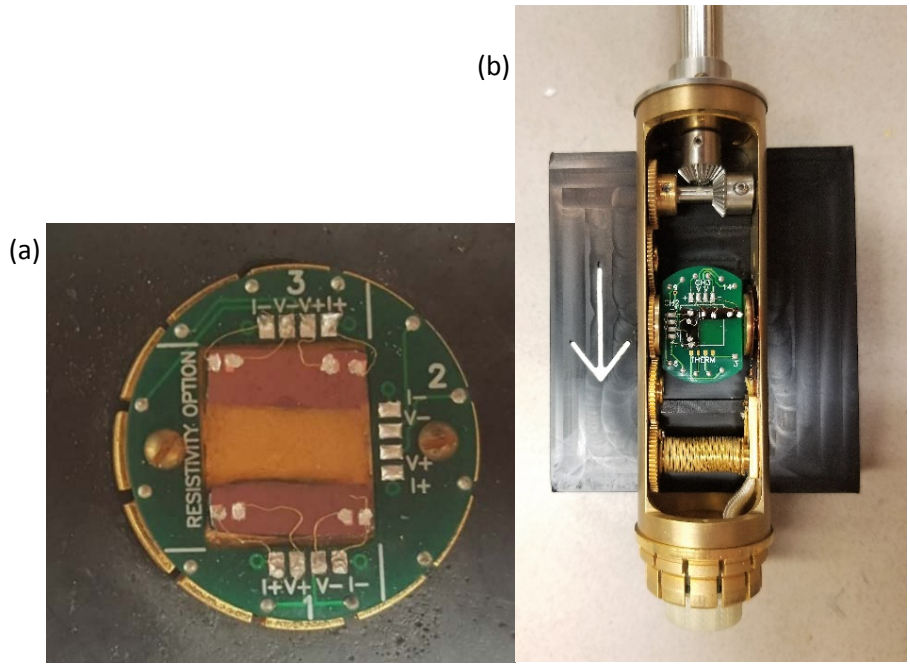

Figure 2.6: (a) Two samples prepared for resistivity measurement on a PPMS resistivity puck. (b) Two samples prepared for angular field dependence on a PPMS rotator puck.

(a)

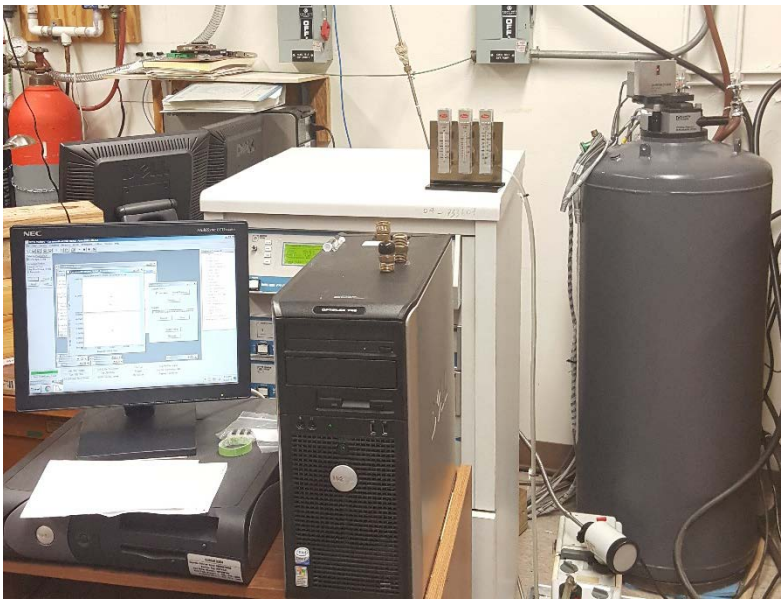

(b)

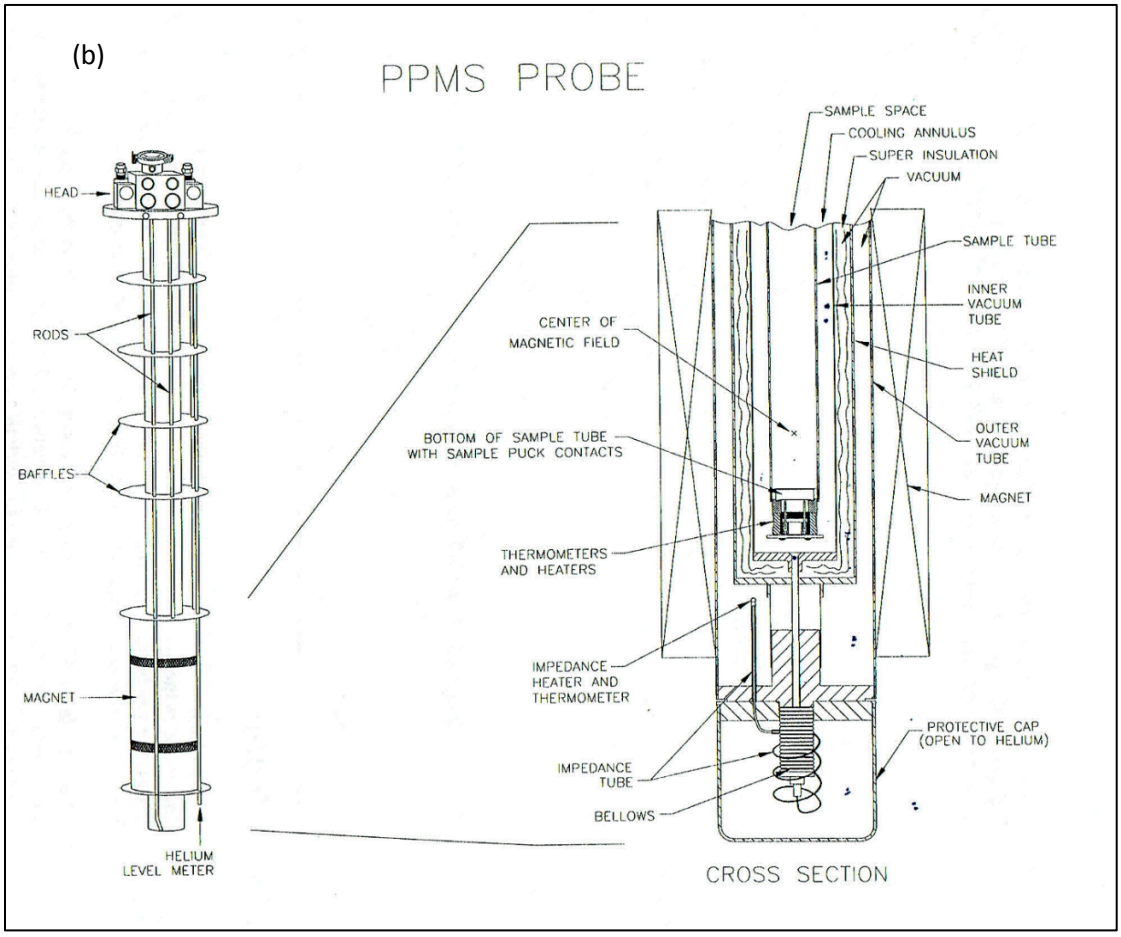

Figure 2.7: (a) Quantum Design PPMS cryostat, control unit, and computer (b) Schematic of the PPMS probe. Reprinted from [50].

2.3 Transport Properties

For resistivity and critical field measurements, the PPMS system uses the standard four point probe method, shown in Figure 2.8. A prepared resistivity sample is shown in Figure 2.6a. In a four point probe measurement, current is passed through the sample via two current leads, and the potential difference across the sample is measured via two separate voltage leads. Thus, the resistance of the contacts has no effect on the measured voltage. Resistance is then calculated by the PPMS using Ohm's Law

$$I = \frac{V}{R} \tag{2.1}$$

where I is the applied current, V is the potential difference, and R is the resistance.

The resistivity of a material ρ, measured in ohm meters $\Omega \cdot m$, is the quantitative measure of how a material opposes the flow of electrons that are under the influence of an electric field ($\vec{E}$), with resistance *R* and current density J. Electrical conductivity, σ, is defined as the inverse of resistivity $\sigma = \frac{1}{\rho}$. Resistivity is not directly measurable but is instead calculated by using the resistance R measured by the PPMS from a film with voltage leads spaced apart by length *L* apart and cross sectional area *A*, giving

$$\rho = \frac{E}{J} = \frac{R \cdot A}{L} \ . \tag{2.2}$$

The cross sectional area was calculated using the reported overall thickness of the films and the measured width of the cut samples. Looking at the representative depiction of the four point prove set up in Figure 2.8, *L* is equal to the distance S_2 depicted, the distance between the voltage leads. The resistance in different types of materials behaves differently with changing temperature.

Above the Debye temperature, the resistivity of a typical metal changes linearly with temperature due to the thermal motion of the ions. This property is often used to calculate the thickness of a thin film of a known metal by measuring the slope of the resistance versus temperature. At much lower temperatures, the temperature dependence is predicted as T^5 due to the electron scattering by phonons or as T^2 due to electron-electron scattering.

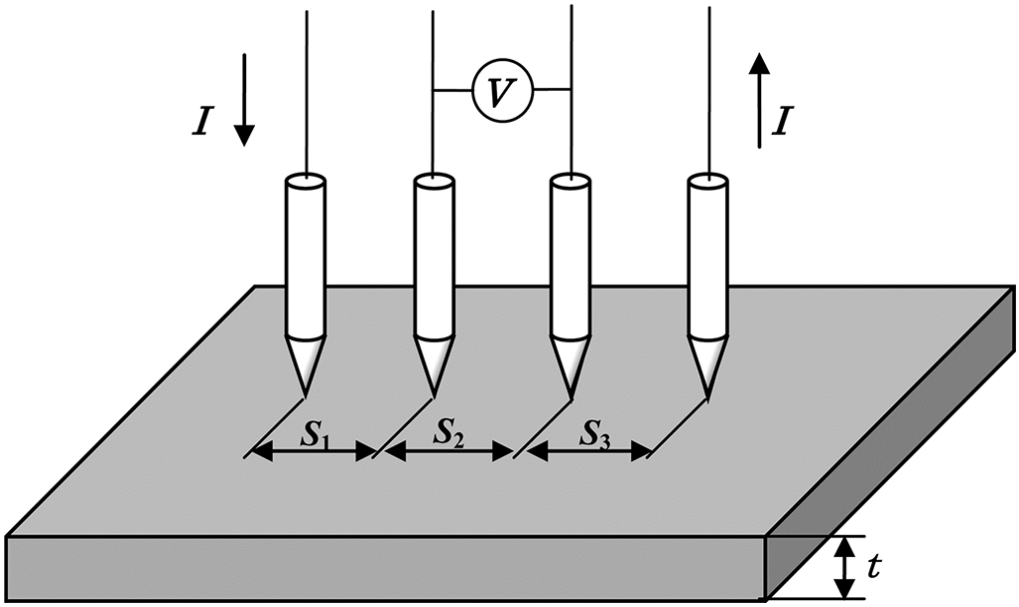

Figure 2.8: Drawing showing four point probe set up for resistivity measurement. Reprinted from [51].

2.4 Microstructural Characterization

Magnesium in bulk form has a hexagonal close packed crystal structure (hcp), and niobium in bulk form has a body centered cubic crystal structure (bcc) (Figure 2.9). X. Zhang's group predicted and experimentally proved a bi-phase diagram for Mg/Nb multilayers with coherent interfaces grown on Si (100). As can be seen in Figure 2.10, there is a region, blue, where bcc magnesium is stable and a region, red, where hcp niobium is stable. The green region is where the

films are both in their bulk crystal structure. Films were studied that fall into each of these three regions for this project.

The effect of this crystal structure change, from a bcc to hcp, on the superconducting properties of niobium was examined through measurements of the transport properties of the Mg/Nb multilayers. To confirm the crystal structure of the layers of the samples, x-ray diffraction (XRD) measurements were performed on all of the films using a Bruker-AXS D8 advanced Bragg-Brentano X-ray powder diffractometer equipped with Cu-Kα source anode, D8 Goniometer, automatic divergence slit, graphite monochromator on the diffracted beam and Lynxeye PSD for detection. The films were exposed to a monochromatic beam of X-rays from a Cu-Kα source, with a wavelength of 1.5406Å.

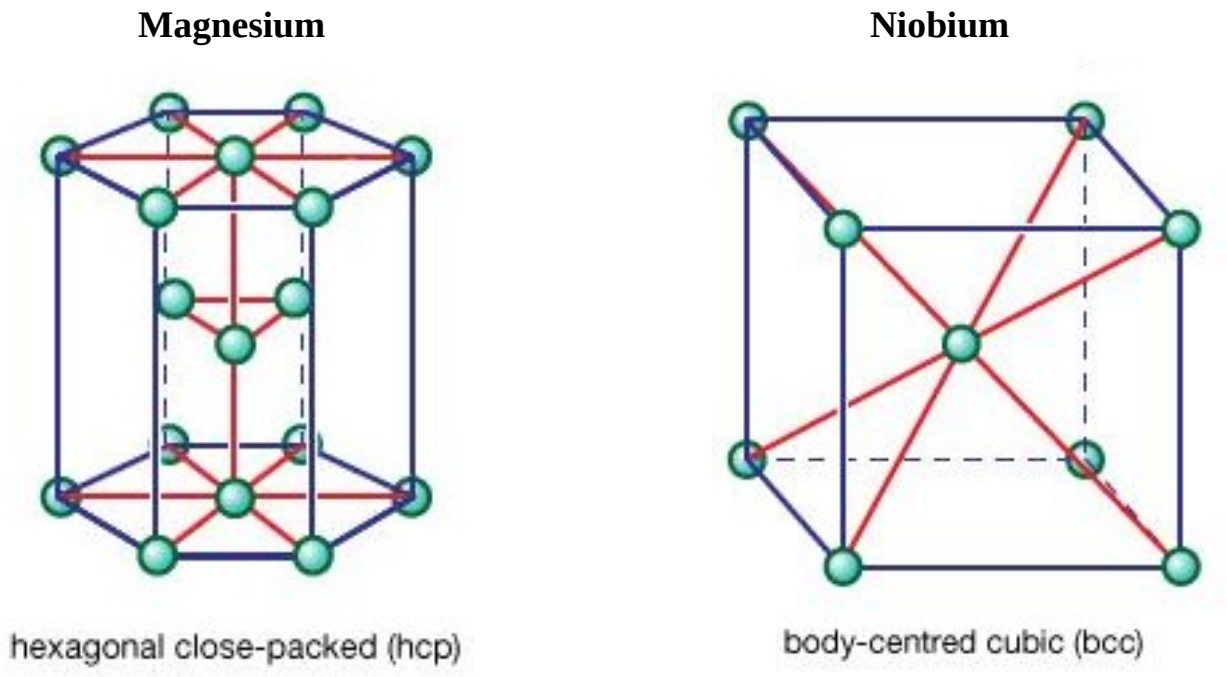

Figure 2.9: The bulk crystal structures of Magnesium and Niobium. Reprinted from [52].

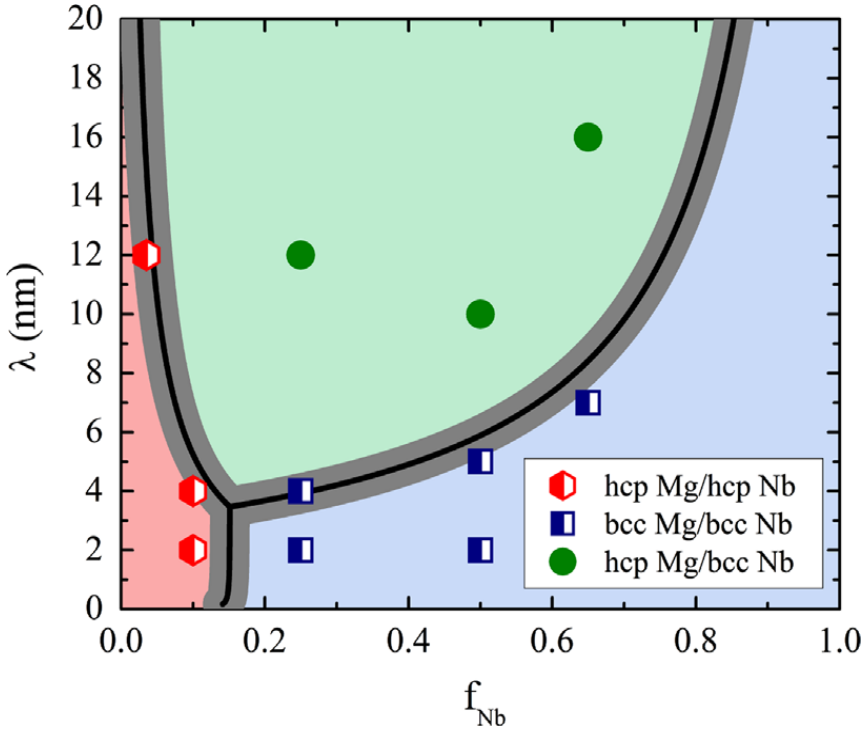

Figure 2.10: The bi-phase diagram is plotted as a function of λ (bilayer thickness) and f_{Nb} (fraction of niobium in the bilayer). Reprinted with permission from [29].

X-ray diffraction analysis [53, 54] is a non-destructive method primarily used for the identification and characterization of compounds based on their diffraction pattern. Bragg's law [55], represented in Figure 2.11, is the basis of X-ray diffraction. Crystalline solids consist of regular arrays of atoms with interplanar spacing characteristic to a given crystal. X-rays, of a certain wavelength, impinging the crystal will be scattered by the atoms of the crystal, and undergo constructive interference when the difference in path lengths is equal to an integer multiple of the wavelength of the incident X-ray. When this constructive interference occurs, a diffracted beam of X-rays will leave the crystal at an angle equal to that of the incident beam. This constructive interference is illustrated in Figure 2.11, by the X-ray paths ABC and A'B'C'. The relationship

between the spacing of the crystal atom planes, the angle of the incident X-ray, and the incident X-ray wavelength is known as Bragg's Law

$$n\lambda = 2d \sin\theta \tag{2.3}$$

where n (an integer) is the "order" of reflection, λ is the wavelength of the incident x-rays, d is the interplanar spacing of the crystal, and θ is the angle of incidence.

X-ray diffraction (XRD) is quite useful in the identification and characterization of crystalline structures by way of Bragg's Law. With XRD, the wavelength and incident angle of the X-rays is known, and by solving the Bragg equation, the spacing between crystal lattice planes is determined. The atomic arrangement in the crystal structure will affect the direction of possible diffractions along with the intensity of the diffracted wave. In a typical XRD setup, a beam of X-rays is directed at the sample, and a detector is used to detect the diffracted beam; the position of the detector and intensity of the beam are used to determine the crystal structure, orientation, and interatomic spacing of the sample.

Thus, using X-ray diffraction, the crystal structure of the samples in this project were studied to see if they followed the bi-phase diagram shown in Figure 2.10. Also of interest was determining if the crystal structure change would have an effect on the proximity effect, or if the proximity effect is strictly governed by the thicknesses of the individual films in the bilayer.

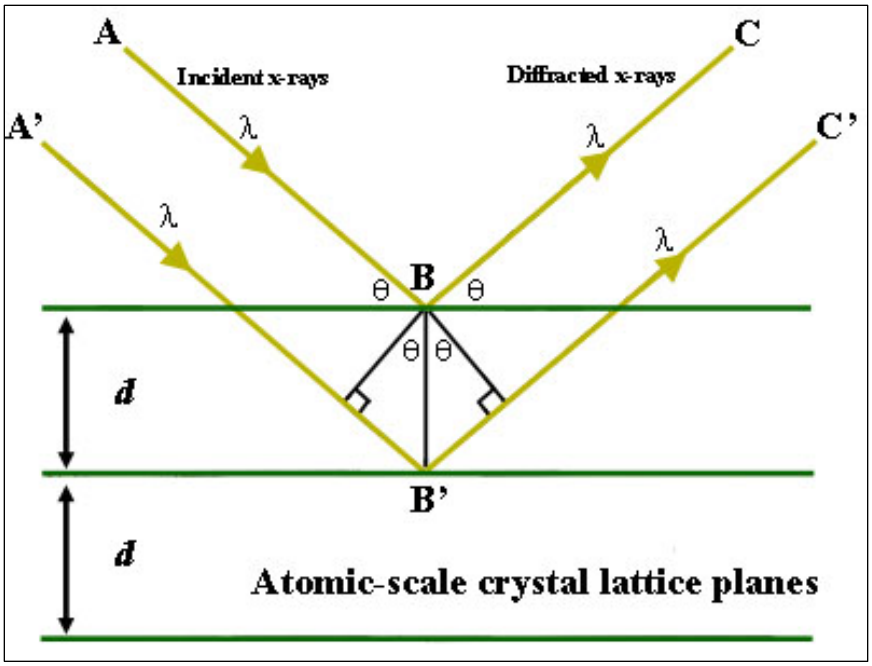

Figure 2.11: A diagram representing Bragg's Law. Reprinted from [56].

3. MATERIAL CHARACTERIZATION[‡]

The crystal structure of the as-deposited Mg/Nb multilayer thin films was examined with XRD. XRD is a useful and non-destructive tool to analyze the microstructure of thin films. This method does not require any sample preparation, and the sample can be quickly scanned. XRD experiments in this study were performed using a Bruker-AXS D8 advanced Bragg-Brentano X-ray powder diffractometer.

The goal was to examine if the samples studied for this thesis fit in with the bi-phase diagram for Mg/Nb multilayers (Figure 2.9) that had been proposed by A. Junkaew et al. [29]. An XRD pattern for three different samples from their study is presented here as a basis for comparison. The XRD was obtained with a Bruker-AXS D8 advanced Bragg-Brentano X-ray powder diffractometer.

[‡] Part of this section, including Figure 3.1, is reprinted with permission from "Tailoring the formation of metastable Mg through interfacial engineering: A phase stability analysis" by A. Junkaew, et al., CALPHAD, 2440 (2014) 145, Copyright 2013 by Elsevier LTD.

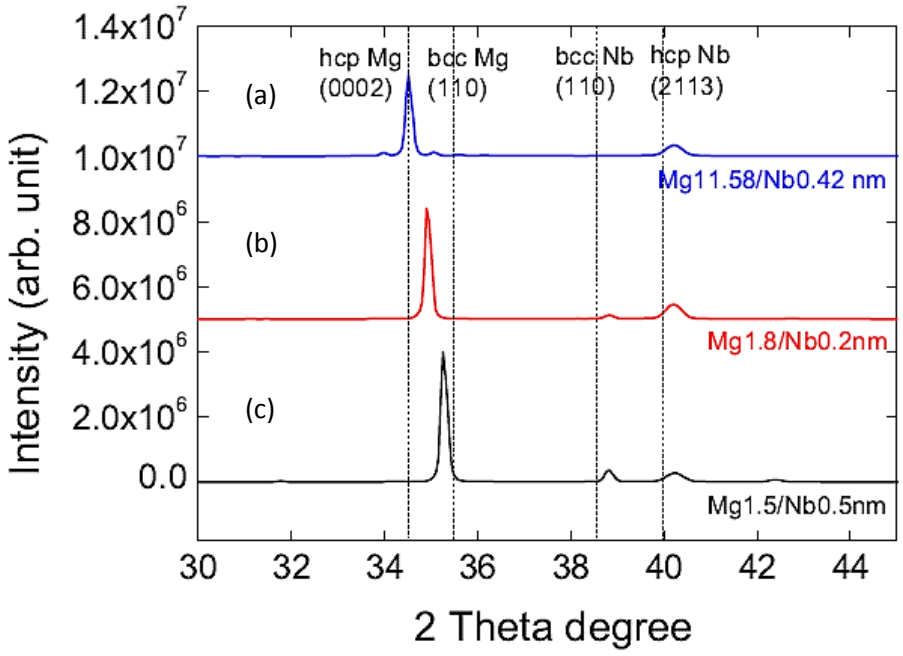

Figure 3.1: XRD profiles of three representative specimens from different regions of the bi-phase diagram. (a) the Mg (11.58nm)/Nb (0.42nm) multilayers, (b) the Mg (1.8nm)/Nb (0.2nm) multilayers, and (c) the Mg (1.5nm)/Nb (0.5nm) multilayers. Reprinted with permission from [29].

Fig. 3.1 shows XRD profiles of three samples, each from a different region in the bi-phase diagram. The dashed vertical lines represent the reference 2θ values of hcp Mg (a=3.2˚A and c=5.19˚A), bcc Mg (a=3.57˚A), bcc Nb (a=3.32˚A) and hcp Nb (a=2.88˚A and c=5.26˚A) obtained from DFT calculations. Mg 11.58nm/Nb0.42nm multilayers (Fig. 3.1(a)) shows coherent Mg and Nb hcp structure. Mg1.8nm/Nb 0.2nm nanolayers (Fig. 3.1(b)) indicates that Mg lattice is slightly distorted and a possible small bcc Nb peak is observed. However, hcp Mg and hcp Nb peaks are dominant. As the fraction of Nb in the bilayer increases, the hcp Mg peak shifts toward the bcc Mg position. The predominant peak in Mg 1.5nm/Nb 0.5nm multilayers (Fig. 3.1(c)) shifted from hcp to bcc Mg position and bcc Nb peak with higher intensity than Fig. 3.1(b) specimen is also shown. However, the hcp Nb peak is still observed indicating a small fraction of hcp lattice exists.

These three specimens correspond to the Mg-rich region of the phase diagram. Instead of aligning epitaxially with bcc Nb, hcp Mg is distorted towards bcc Mg's lattice parameter in Fig. 3.1(b) and (c). For the same bilayer thickness, changing the volume ratio of components has an effect on the magnitude of distortion from the hcp to bcc structures.

All of the following XRD graphs presented are those done for this study. The dashed lines correspond to the reference 2θ values obtained by A. Jankwae et al. through DFT calculations, Table 3.1. Figure 3.2 shows the bi-phase diagram with points (diamonds) added in to represent where the films from this study would be expected to be.

Table 3.1 DFT Calculated Values

X-ray Cu-Kα1 λ= 1.540598	**H K L**	**2θ (degrees)**	**d (Å)**
Nb hcp	0 0 2	34.035	2.63200
	1 0 0	35.992	2.49329
	1 0 1	39.980	2.25331
Mg hcp	1 0 0	32.277	2.77128
	0 0 2	34.536	2.59500
	1 0 1	36.734	2.44461
Mg bcc	1 1 0	35.534	2.52437
	2 0 0	51.131	1.78500
Nb bcc	1 1 0	38.310	2.34759
	2 0 0	55.296	1.66000

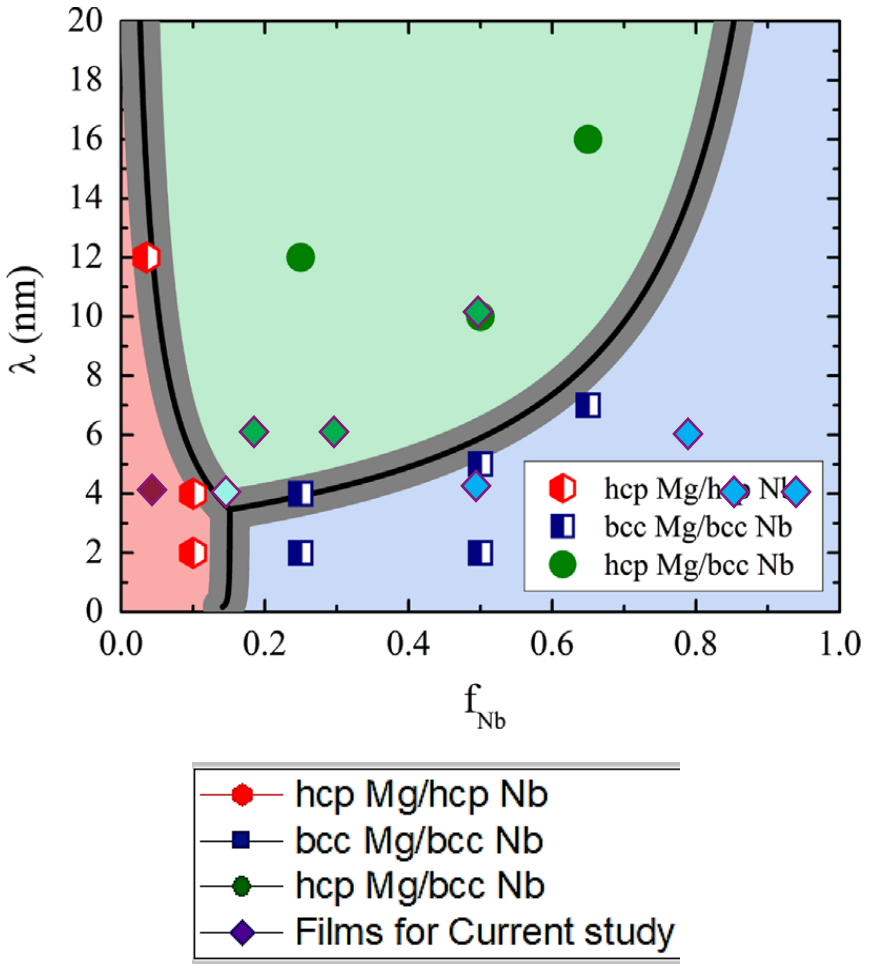

Figure 3.2: The bi-phase diagram is plotted as a function of λ (bilayer thickness) and f_{Nb} (fraction of niobium in the bilayer). The red dots indicate films that Dr. Zhang's group found to have crystal structure of hcp Mg/hcp Nb. The Blue squares indicated films that Dr. Zhang's group found to have bcc Mg/bcc Nb. The green spheres indicate films that Dr. Zhang's group found to have hcp Mg/bcc Nb. The diamond points indicate the films from this study. Adapted from [29].

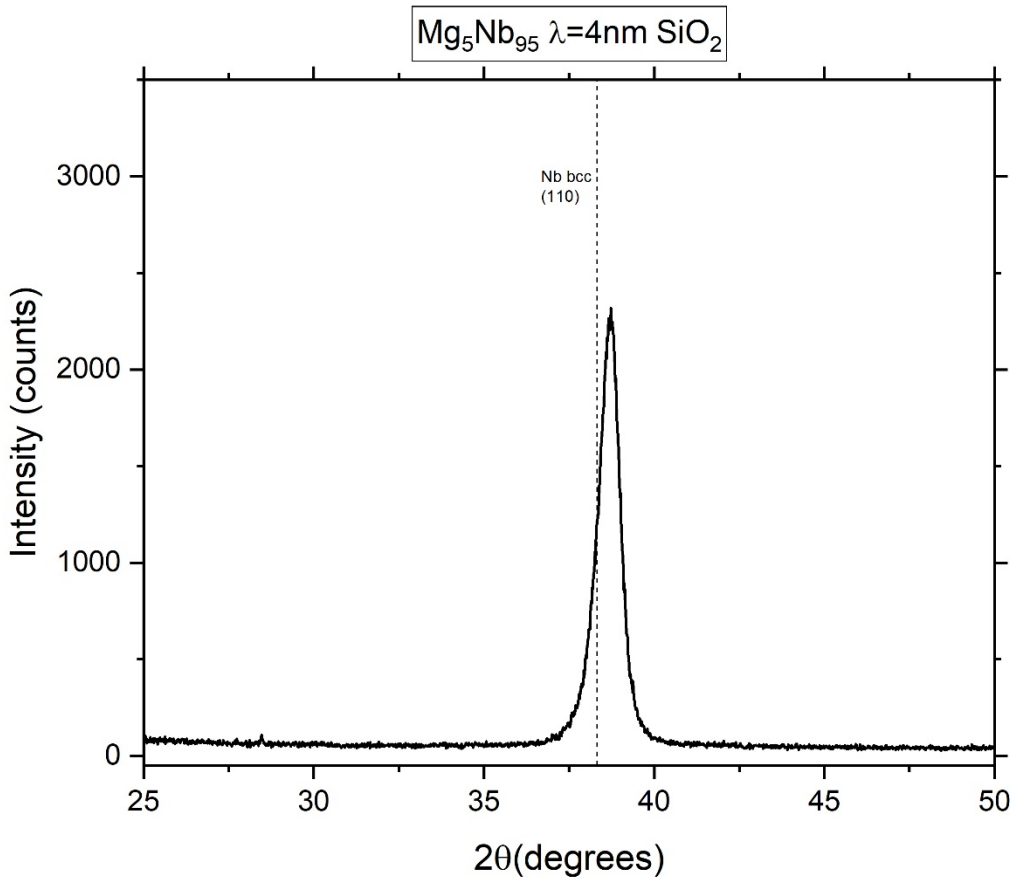

Figure 3.3: Mg(0.2nm)Nb(3.8nm) film on SiO_2 XRD Pattern

Figure 3.3 shows the XRD pattern for the film composition Mg_5Nb_{95}, individual layer thicknesses Mg 0.2nm and Nb 3.8nm. The Nb (110) peak is well pronounced, however, the Mg peak is not present in this scan. This could be due to the orientation of the film during the scan or the very low amount of Mg present in the sample. A bcc Mg peak would be expected from the bi-phase diagram if one did appear.

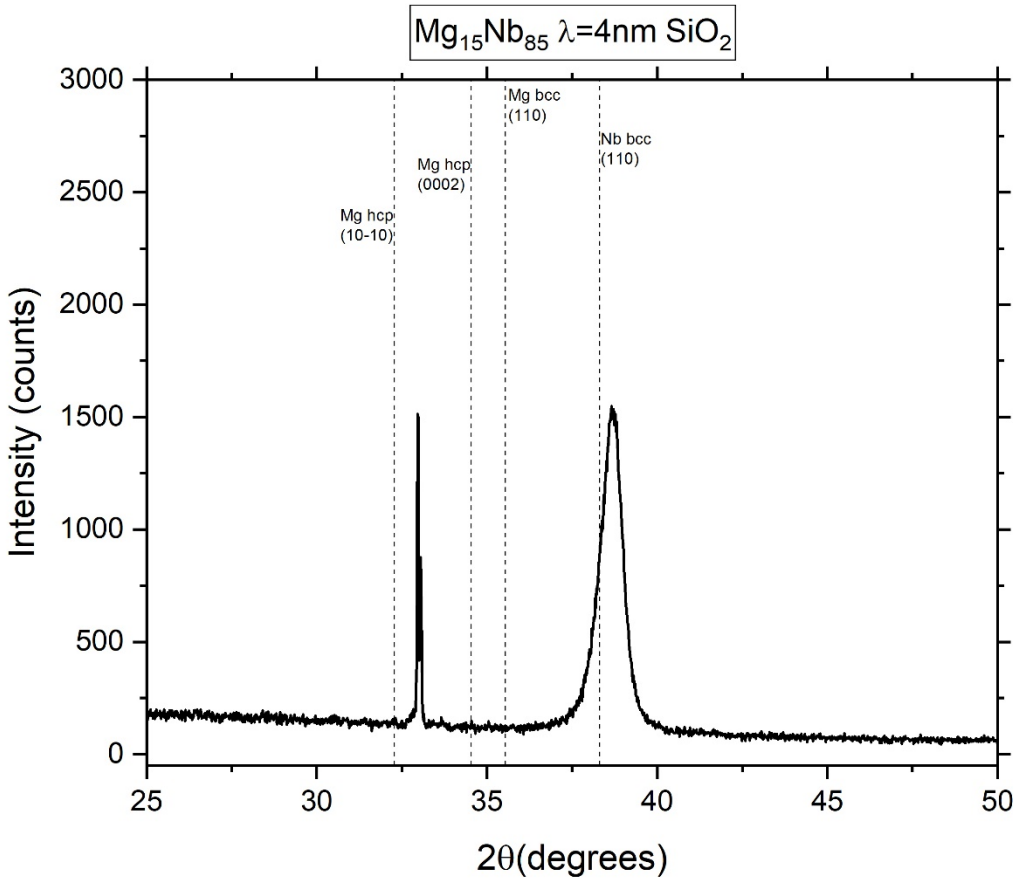

Figure 3.4: Mg(0.6nm)Nb(3.4nm) film on SiO_2 XRD Pattern

Figure 3.4 shows the XRD pattern for the film composition $Mg_{15}Nb_{85}$, individual layer thicknesses Mg 0.6nm and Nb 3.4nm. The Nb (110) peak is well pronounced, as is a peak that could be the Mg $(10\bar{1}0)$ peak, but could also be a Si peak. As with the previous film, based on the bi-phase diagram, a bcc Mg peak was expected, though no evidence of that peak is seen.

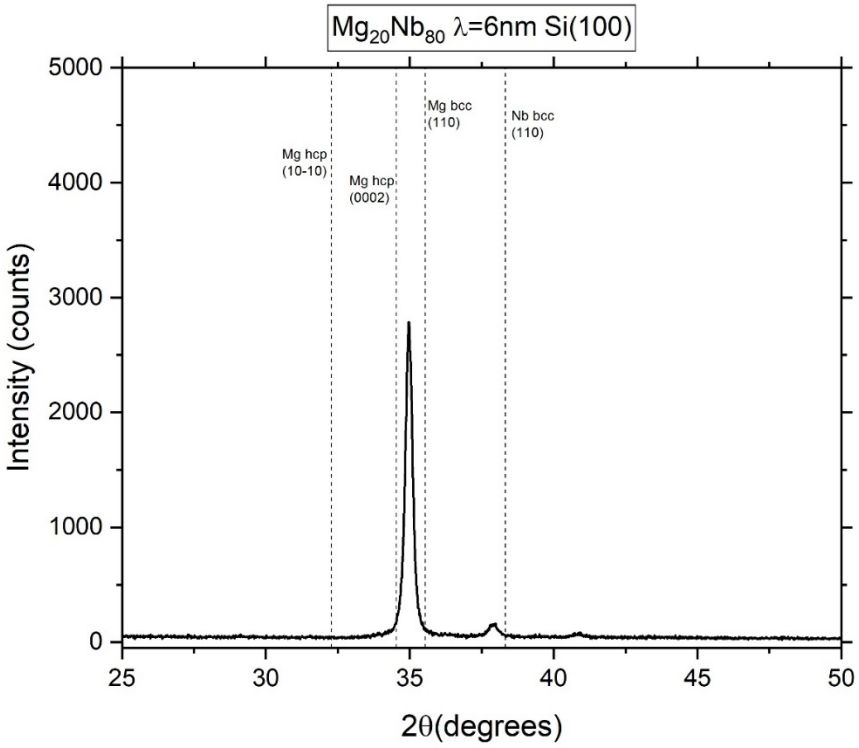

Figure 3.5: Mg(1.2nm)Nb(4.8nm) film on Si(100) XRD Pattern

In Figure 3.5 the Nb (110) peak, for the film Mg(1.2nm)/Nb(4.8nm), is small but apparent. There is a possible small peak close to 42 degrees that could be a Nb peak or Si peak. The Mg (0002) peak is shifted towards the Mg bcc peak position. It was expected that the Mg peak would be shifted closer to the bcc position, or there would be two peaks, one near the hcp peak position and one near the bcc peak position. There is a small peak near 42 degrees which could be a Si peak or a shifted Nb peak. The peaks all appear to be equally spaced. Calculating the integer 'n' for the three peaks visible here with the bilayer thickness being the interplanar spacing d in the Bragg's formula, the following numbers were obtained.

Table 3.2 Calculations for integer n, from Bragg's Law.

2θ	λ (Å)	d (Å)	n
40.82	1.5406	59.64	27
37.865	1.5406	59.35	25
34.958	1.5406	58.99	23

Lambda here is the wavelength of the incident X-rays from the XRD equipment. The n values are equally spaced, which indicates that the film is a superlattice film with repeated layers. If this is true, then the peaks are for the supperlattice film and not the individual materials. For n integer, the bilayer thickness results are not an exact match for the reported thickness, though it is very close. This is not unexpected, as it would be difficult to have the bilayers all be exactly an integer amount. This is seen for all of the following film XRD plots where n was calculated.

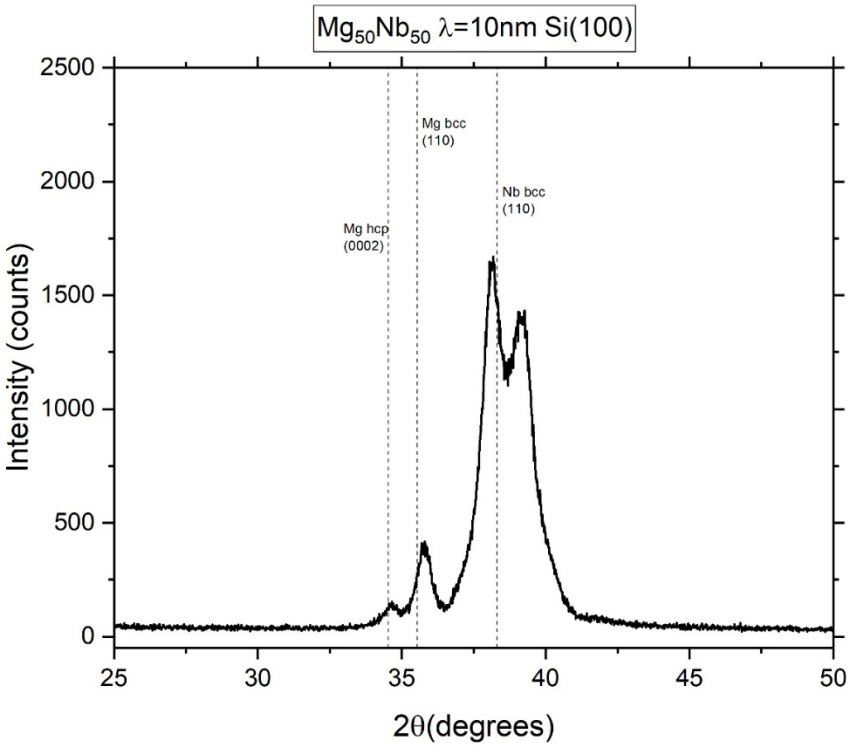

Figure 3.6: Mg(5nm)Nb(5nm) film on Si(100) XRD Pattern

Figure 3.6 shows the XRD pattern for the film composition $Mg_{50}Nb_{50}$, individual layer thicknesses Mg 5.0nm and Nb 5.0nm. The Nb (110) peak is well pronounced, and a satellite peak is quite pronounced as well. The Mg (0002) peak is visible next to a larger peak that is either a (0002) satellite peak or a Mg (110) peak. The (110) peak was not expected based on the bi-phase diagram, only the (0002) peak was expected.

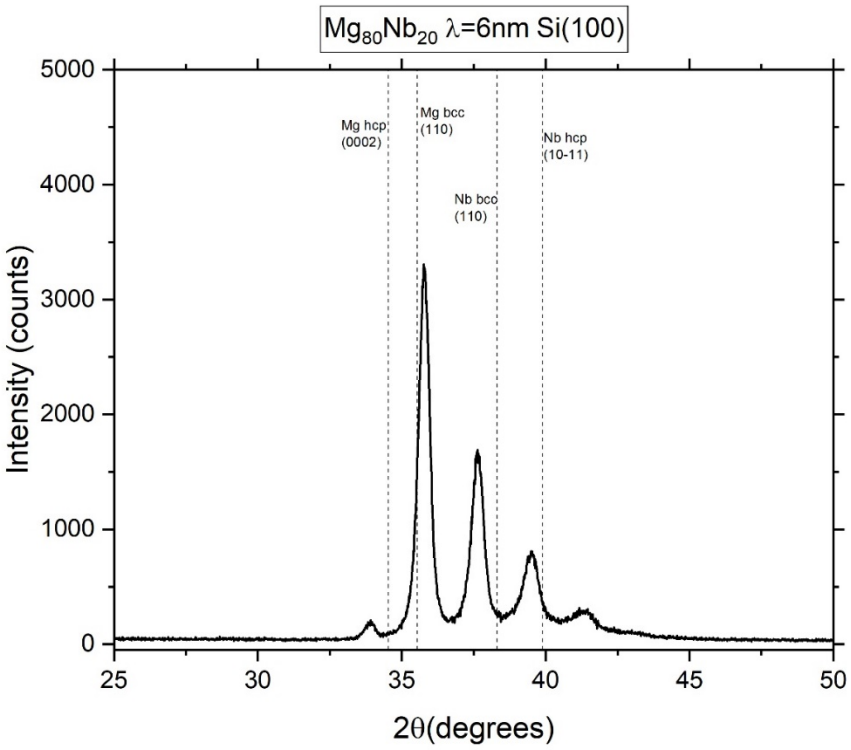

Figure 3.7: Mg(1.2nm)Nb(4.8nm) film on Si(100) XRD Pattern

Figure 3.7 shows the XRD pattern for the film Mg(4.8nm)/Nb(1.2nm). The Nb (110) peak appears to be shifted, and a shifted Nb $(10\bar{1}0)$ peak is visible as well. The Mg (0002) peak is visible next to a Mg (110) peak. It is plausible to expect all of these peaks, as this film falls in an area just above the triple point of the phase diagram. Here again the peaks appear to be equally spaced. Calculating the 'n' for the peaks for this film, the results imply that the observed reflection spacings are due to the superlattice structure of the sample.

Table 3.3 Calculations for integer n, from Bragg's Law.

2θ	λ (Å)	d (Å)	n
41.31	1.5406	58.96	27
39.501	1.5406	59.27	26
37.64	1.5406	59.69	25
35.78	1.5406	60.18	24
33.909	1.5406	60.76	23

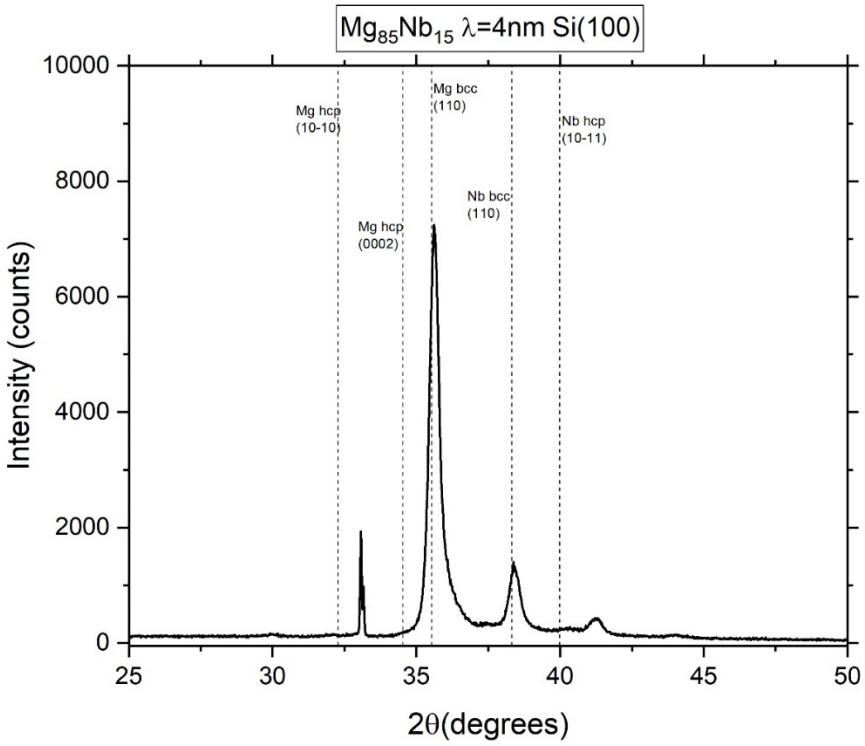

Figure 3.8: Mg(3.4nm)Nb(0.6nm) film on Si(100) XRD Pattern

In Figure 3.8 the XRD pattern for the film Mg(3.4nm)/Nb(0.6nm) is shown. The Nb (110) peak is well defined, and a shifted Nb $(10\bar{1}0)$ peak is visible as well. The small Mg $(10\bar{1}0)$ peak is visible next to a pronounced Mg (110) peak. Once again, it is reasonable to expect to see all of these peaks, as this film falls in an area just below the triple point of the phase diagram. The small

peak around 44 degrees is possibly a Si peak. The peak spacing for this film indicate that this sample also has a superlattice structure.

Table 3.4 Calculations for integer n, from Bragg's Law.

2θ	λ (Å)	d (Å)	n
43.98	1.5406	39.09	19
41.22	1.5406	39.369	18
38.41	1.5406	39.81	17
35.64	1.5406	40.27	16
33.12	1.5406	40.54	15

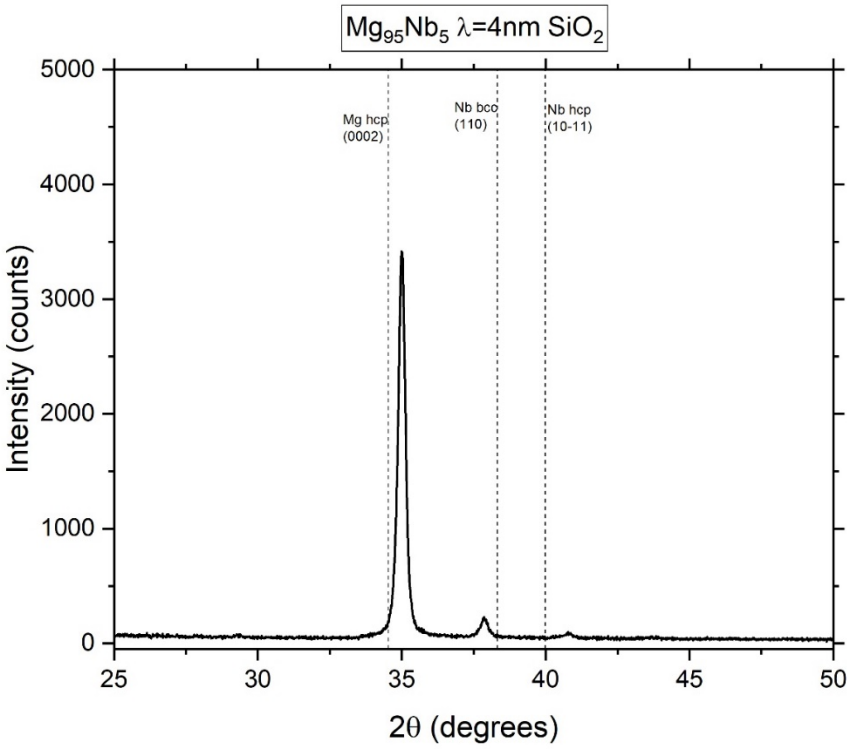

Figure 3.9: Mg(3.8nm)Nb(0.2nm) film on SiO_2 XRD Pattern

Figure 3.9 shows the XRD pattern for the film Mg(3.8nm)/Nb(0.2nm). The Nb (110) peak is still visible, and a Nb $(10\bar{1}0)$ peak is visible as well. The Mg (0002) peak is well pronounced. The spacing is approximately equal between the peaks.

Table 3.5 Calculations for integer n, from Bragg's Law.

2θ	λ (Å)	d (Å)	n
40.777	1.5406	39.80	18
37.87	1.5406	40.36	17
35.01	1.5406	40.97	16

A few of the films from this study fit well with the bi-phase diagram while the others show deviation from the expectation. Further XRD studies should be done as well as TEM analysis to further examine the crystal structure of these films. These will be discussed in Chapter 5.

4. RESULTS AND DISCUSSION

4.1 Resistivity

4.1.1 TAMU Sputtered Mg/Nb Multilayers

The resistivity of the multilayer films was measured to study the superconducting proximity effect on the transition temperature. The first batch of samples for this project was sputtered at Texas A&M University. Copper contact pads were thermally evaporated onto each of the prepared samples from this batch. The compositions listed below[§] were each grown on four substrates – Si(100), Si(110), Si(111) and SiO_2. For each sample, a layer of niobium was first deposited followed by a layer of magnesium. This bilayer was then repeated several times until the desired overall/total thickness was achieved (see Figure 2.2). Finally, a layer of niobium was deposited to form a cap to reduce the oxidation of the samples.

- $Mg_{15}Nb_{85}$ bilayer thickness 4nm (Mg 0.6nm, Nb 3.4nm), 3nm Nb cap, total thickness 51nm
- $Mg_{50}Nb_{50}$ bilayer thickness 4nm (Mg 2.0nm, Nb 2.0nm), 2nm Nb cap, total thickness 50nm
- $Mg_{50}Nb_{50}$ bilayer thickness 10nm (Mg 5nm, Nb 5nm), 3nm Nb cap total thickness 63nm
- $Mg_{70}Nb_{30}$ bilayer thickness 6nm (Mg 4.2nm, Nb 1.8nm), 2nm Nb cap, total thickness 63nm

Presented first is the resistivity for the film composition $Mg_{15}Nb_{85}$ with bilayer thickness 4nm, 12 bilayer repeats, and total thickness 51nm, which includes the Nb cap of 3nm. The individual thickness of Mg is 0.6nm and Nb is 3.4nm.

[§] Three other films were grown, but because they could not be measured with the PPMS system, they are not included as part of this study. The films were: $Mg_{85}Nb_{15}$ bilayer thickness 4nm, Nb cap 1nm, total thickness 51nm; $Mg_{90}Nb_{10}$ bilayer thickness 6nm, Nb cap 1nm, total thickness 61nm; and $Mg_{96}Nb_{4}$ bilayer thickness 12nm, Nb cap 0.5nm, total thickness 61nm.

As can be seen in Figure 4.1(a), the film on the Si (100) substrate behaves like a normal superconducting material with decreasing resistivity as the temperature decreases. There is a slight shift around 200K possibly due to the substrate being slightly conducting at high temperatures or could be stress due to differential expansion. This shift occurred for all four films, listed above, grown on the Si (100) substrate. The transition temperature (T_c) is about 6.4K, highlighted in Figure 4.1 (b).

Next, a look at the same film composition, but on the Si (110) substrate, is shown in Figure 4.2(a). The resistivity, in this case, is three orders of magnitude smaller than the film on the Si (100) substrate. Such low values are unrealistic for resistivity when compared with resistivity values for the other substrates and with other similar films seen in the literature [14, 23, 25]. This irregular behavior was observed on all films deposited on the Si (110) substrate from the first sample/growth batch at TAMU. The reason for this behavior is not currently known. The T_c (Figure 4.2 (b)) is approximately 6.4K as with the film on the Si (100).

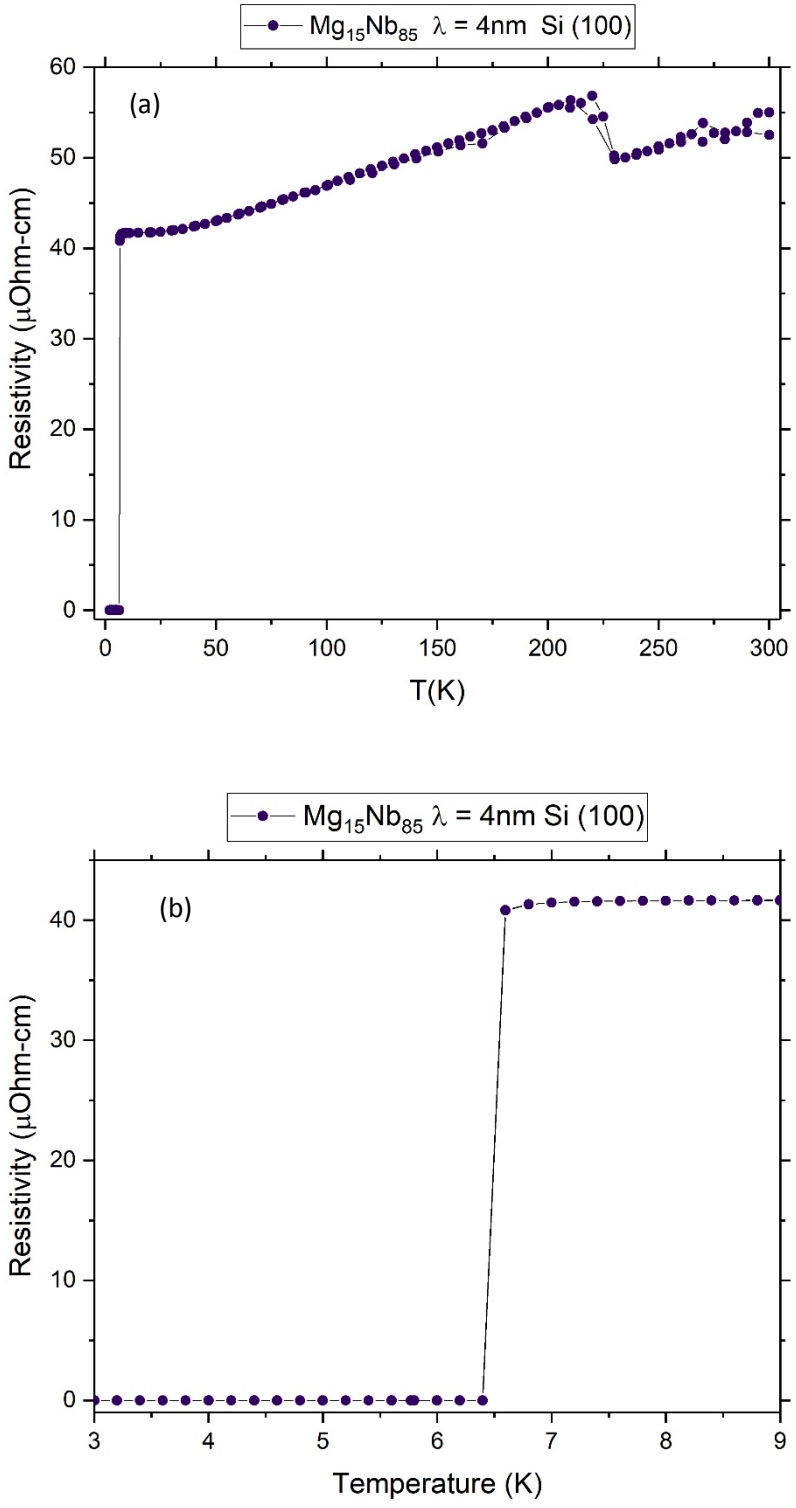

Figure 4.1: (a) Mg(0.6nm)/Nb(3.4nm) film on Si (100). (b) Superconducting transition curve, T_c ~ 6.4K. Sputtered at TAMU.

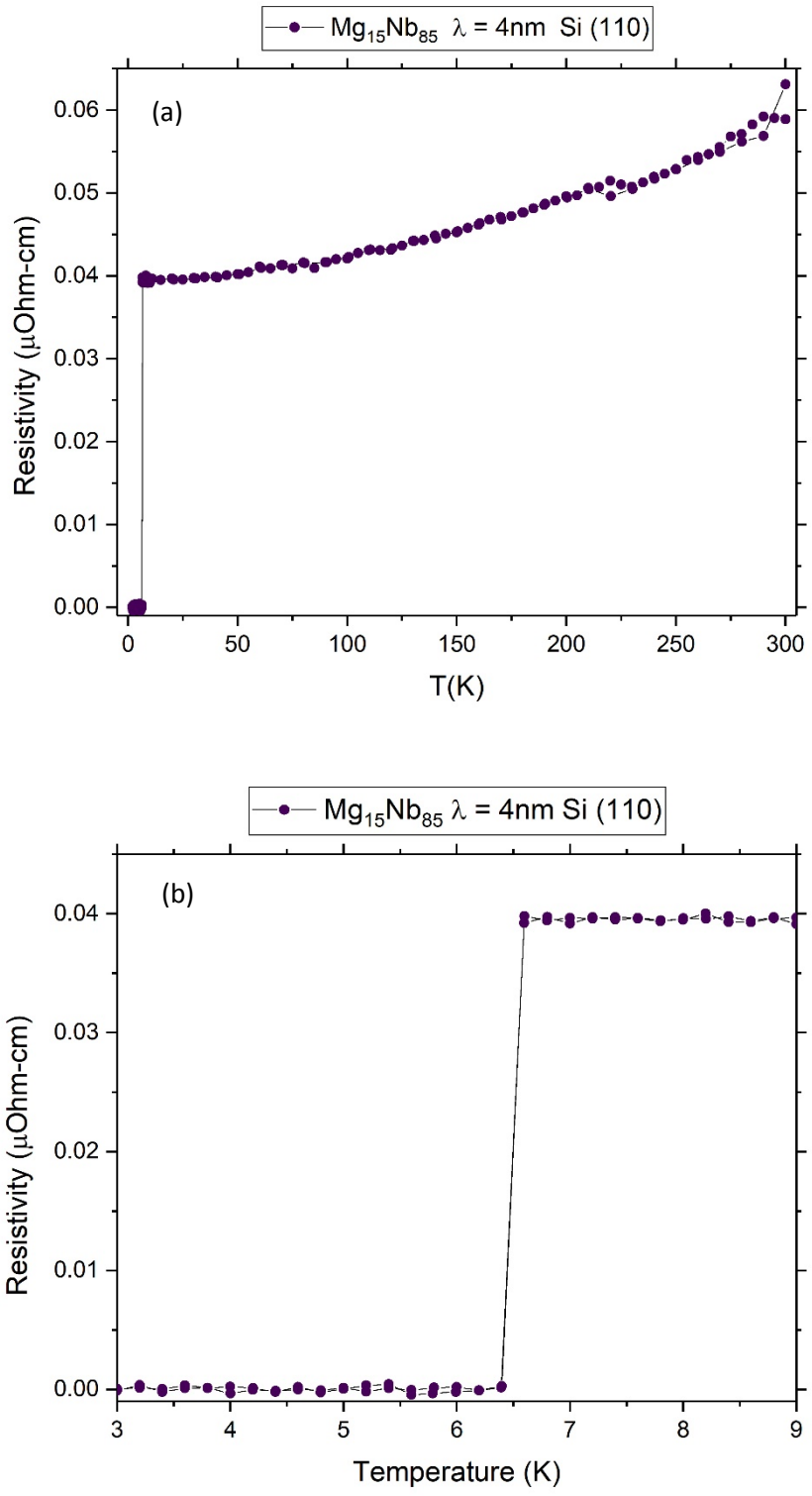

Figure 4.2: (a) Mg(0.6nm)/Nb(3.4nm) film on Si (110). (b) Superconducting transition curve, T_c ~ 6.4K. Sputtered at TAMU.

The $Mg_{15}Nb_{85}$ film deposited on the Si (111), shown in Figure 4.3(a), displays unusual behavior at high temperatures, which is more consistent with a semiconductor material rather than metal materials, as the resistivity increases with decreasing temperature until reaching lower temperatures (~150-80K). This peculiar behavior is noticeable on all films grown on the Si (111) wafer. The resistivity of the bare Si (111) substrate was measured, and it was discovered that it is conducting at temperatures above 100K, at which point it becomes insulating, and the resistivity is due only to the $Mg_{15}Nb_{85}$ film. The T_c (Figure 4.3 (b)) for this film on the Si (111) is the expected 6.4K.

For the fourth substrate, SiO_2, the $Mg_{15}Nb_{85}$ film behaves as expected, Figure 4.4(a), with decreasing resistivity as the temperature decreases until it reaches its transition temperature (Figure 4.4 (b)) at about 6.4K. This is expected since SiO_2 is an excellent insulator.

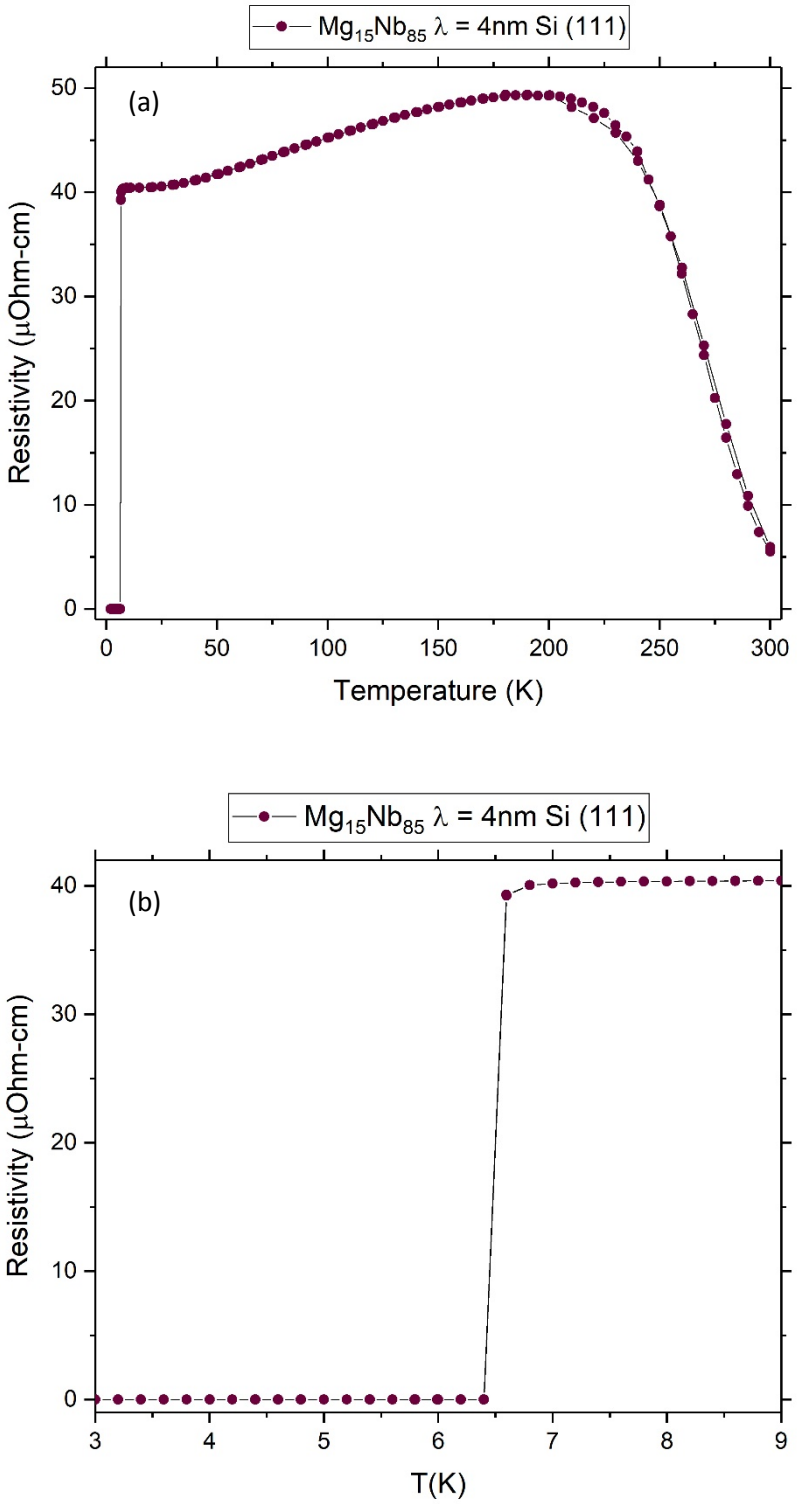

Figure 4.3: (a) Mg(0.6nm)/Nb(3.4nm) film on Si (111). (b) Superconducting transition curve, T_c = 6.39K. Sputtered at TAMU.

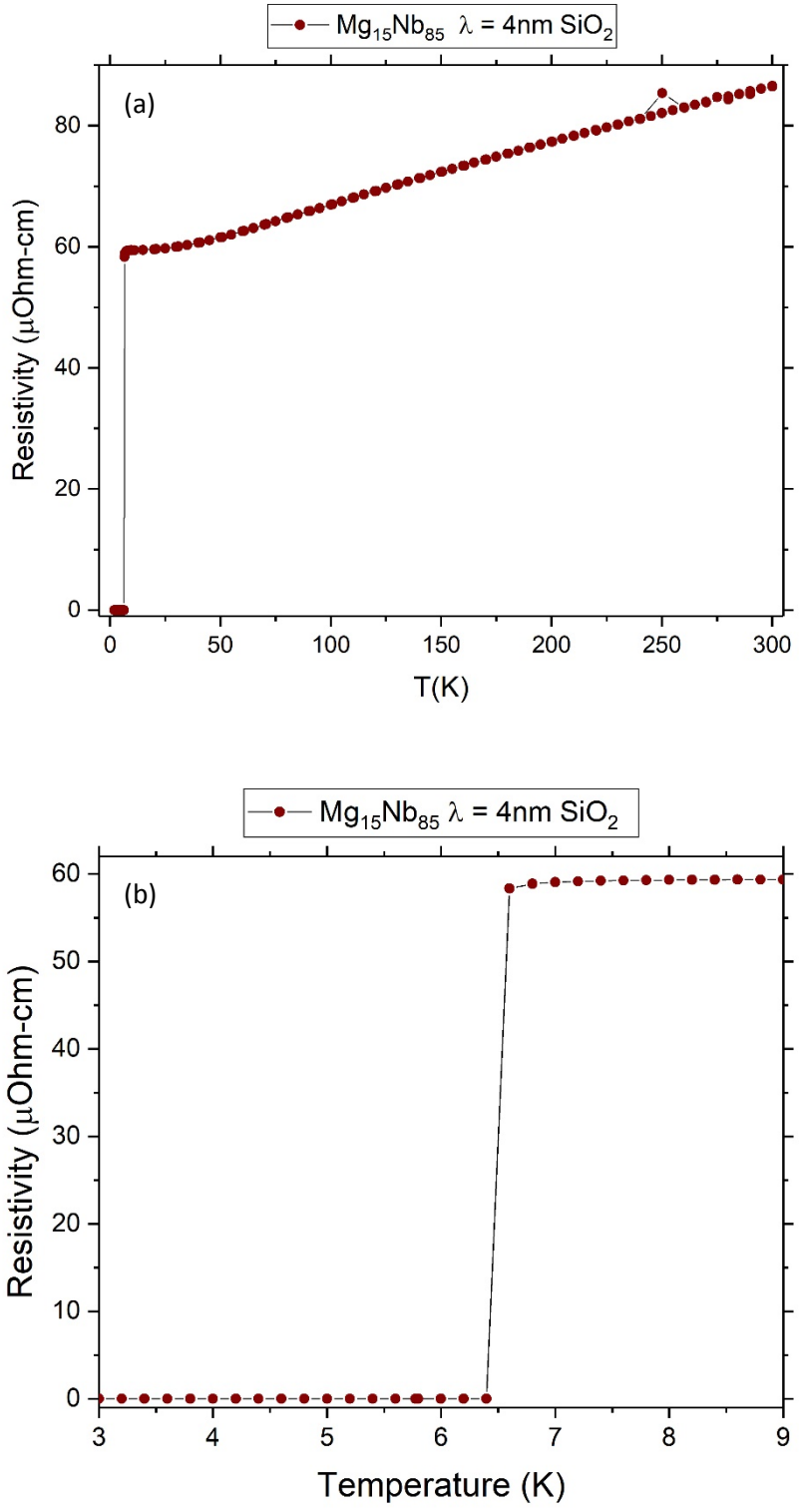

Figure 4.4: (a) Mg(0.6nm)/Nb(3.4nm) film on SiO_2. (b) Superconducting transition curve, $T_c \sim 6.4K$. Sputtered at TAMU.

To highlight the unique behaviors previously discussed, Figures 4.5-4.8 show a comparison of the film compositions with transition temperatures above 1.7K for each of the substrates used. The comparison of the films on the Si(100) substrate, near their transition temperatures, is displayed in Figure 4.5. Figure 4.6 shows the transitions of the films on the Si(110) substrate, while Figures 4.7 and 4.8 exhibit superconducting transitions of the films on the Si(111) and SiO_2 substrates, respectively.

Next, focusing on the film composition $Mg_{50}Nb_{50}$, bilayer thickness 4nm, it is apparent the behavior of this film on each substrate at high temperatures is consistent with that of the prior film composition discussed, $Mg_{15}Nb_{85}$. Figures 4.5-4.8 show that the transition temperature for the $Mg_{50}Nb_{50}$ film is approximately 2.9K on all four of the substrates. The resistivity values are higher than expected for this film when compared with resistivity values of $Mg_{15}Nb_{85}$ and similar multilayers in the literature [20-26], except for the film on the Si (110) which is extremely low, as previously mentioned in the discussion of the $Mg_{15}Nb_{85}$ film. For the subsequent set of samples with same film composition, $Mg_{50}Nb_{50}$, but with a thicker bilayer of 10 nm, the behavior observed on each substrate at high temperatures is consistent with the previous two films. The transition temperature for this film is near 4.3K for each substrate (Fig. 4.5 and 4.8). Finally, with the fourth film, $Mg_{70}Nb_{30}$ with a bilayer thickness of 6 nm, the behavior on each of the four substrates at high temperatures once more reflected that of the previous compositions. The transition temperature for this film is approximately 2.4K on each of the substrates.

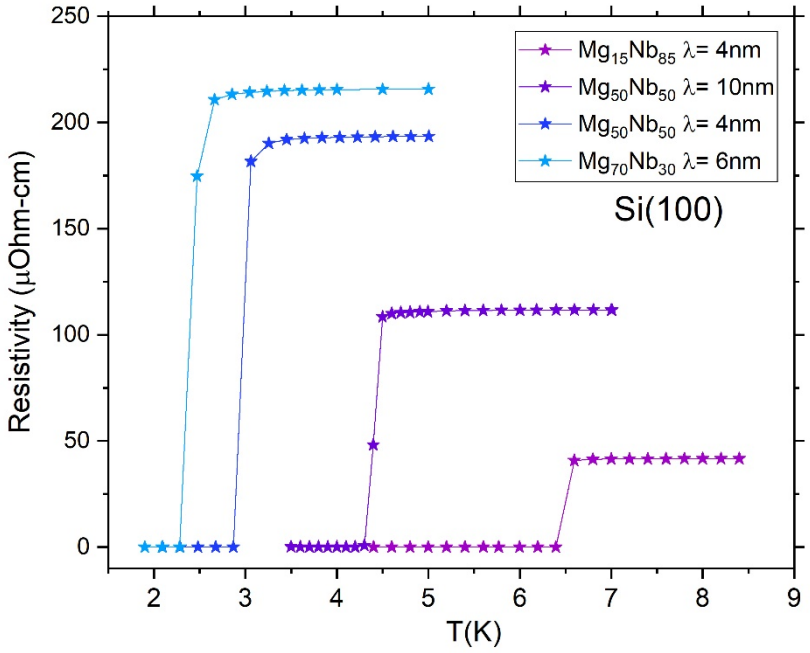

Figure 4.5: Superconducting transition curves for the four films grown on Si(100) substrate, sputtered at TAMU.

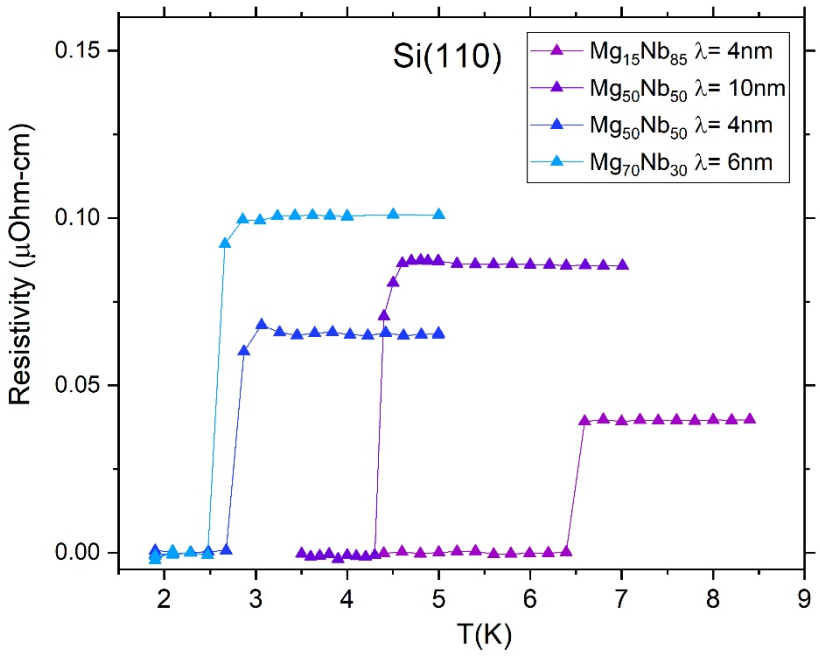

Figure 4.6: Superconducting transition curves for the four films grown on Si(110) substrate, sputtered at TAMU.

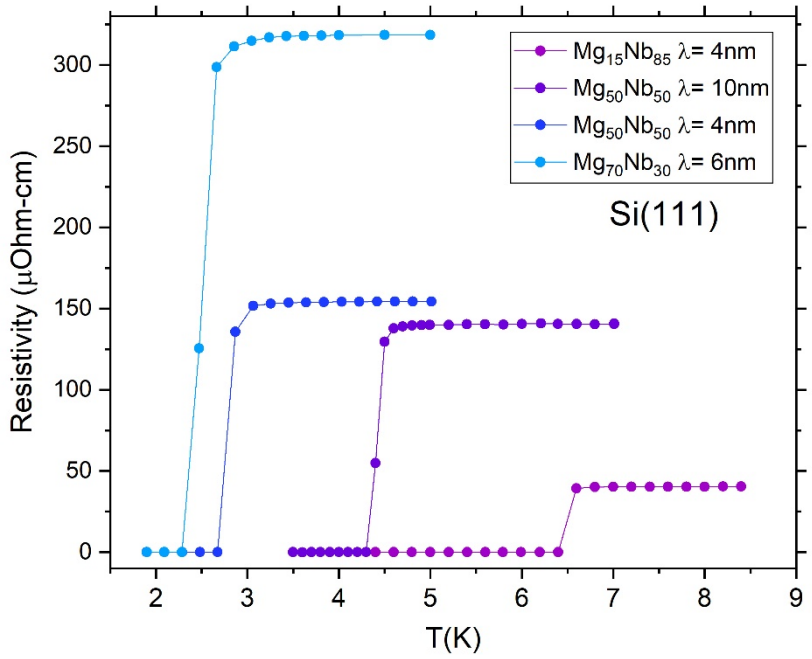

Figure 4.7: Superconducting transition curves for the four films grown on Si(111) substrate, sputtered at TAMU.

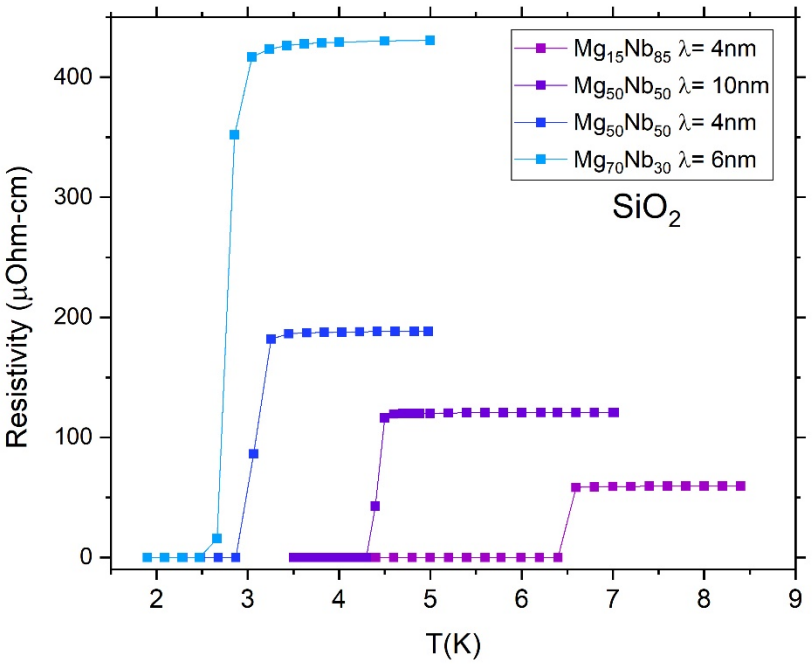

Figure 4.8: Superconducting transition curves for the four films grown on SiO_2 substrate, sputtered at TAMU.

As previously mentioned, copper contact pads were evaporated onto the samples. Due to copper readily oxidizing, and potentially oxidizing the films, some of the films discussed were re-measured using silver contact pads. The results using the silver contacts compared to the copper contacts were varied. For the niobium rich samples up to the 50/50 composition, the results were nearly identical to the measurements with copper contact pads. For example, the $Mg_{50}Nb_{50}$ film with bilayer thickness 10nm had a transition temperature very similar to the measurement of the same film with copper contacts. Conversely, the magnesium rich sample, $Mg_{70}Nb_{30}$ with bilayer thickness 6nm, had a transition temperature of about 1.7K for SiO_2, Si(110) and Si(100), but for the Si(111) the film did not transition to zero above 1.7K. It started to decrease at 1.7K and would most likely have transitioned not far below that. This transition is lower than the previously measured T_c of 2.4K on all four substrates using copper pads. The film showed signs of oxidation, and that is likely the reason for the drop in T_c.

4.1.2 Purdue Sputtered Mg/Nb Multilayers

The following section discusses a second batch of samples sputtered at Purdue University by the same group that grew the first sample set discussed previously. Silver contact pads were evaporated on each of the samples from this growth. As with the first growth, the first layer was niobium followed by a layer of magnesium, and these layers were then repeated until the desired overall thickness is achieved. The last layer is a 3nm cap of niobium to reduce the oxidation of the samples. The compositions grown were:

- Mg_5Nb_{95} bilayer thickness 4nm (Mg 0.2nm, Nb 3.8nm), 3nm Nb cap, total thickness 83nm
- $Mg_{15}Nb_{85}$ bilayer thickness 4nm (Mg 0.6nm, Nb 3.4nm), 3nm Nb cap, total thickness 63nm

- $Mg_{20}Nb_{80}$ bilayer thickness 6nm (Mg 1.2nm, Nb 4.8nm), 3nm Nb cap, total thickness 63nm
- $Mg_{50}Nb_{50}$ bilayer thickness 10nm (Mg 5.0nm, Nb 5.0nm), 3nm Nb cap, total thickness 73nm
- $Mg_{80}Nb_{20}$ bilayer thickness 6nm (Mg 4.8nm, Nb 1.2nm), 3nm Nb cap, total thickness 63nm
- $Mg_{85}Nb_{15}$ bilayer thickness 4nm (Mg 3.4nm, Nb 0.6nm), 3nm Nb cap, total thickness 63nm
- $Mg_{95}Nb_{5}$ bilayer thickness 4nm (Mg 3.8nm, Nb 0.2nm), 3nm Nb cap, total thickness 83nm

Two of the films have the same composition as two from the sample set sputtered at TAMU. This was to allow for an evaluation of the sputtering system at the two locations to see if the films would yield the same results.

Shown first is the film composition Mg_5Nb_{95} on each of the four substrates for bilayer thickness 4nm, 20 bilayer repeats, and total thickness 83nm. As can be seen in Figure 4.9, the film on the Si (100) substrate behaves like a normal superconducting material with decreasing resistivity as the temperature decreases. There is a very slight shift around 200K, comparable to that seen in the films sputtered at TAMU; this could be due to either a phase transition or the substrate being slightly conducting at high temperatures. Review of Figure 4.10 reveals the film on the Si (110) has behavior very similar to that of the Si (100) with almost identical resistivity values, unlike the extremely low resistivity values seen on all measured films sputtered on Si (110) at TAMU.

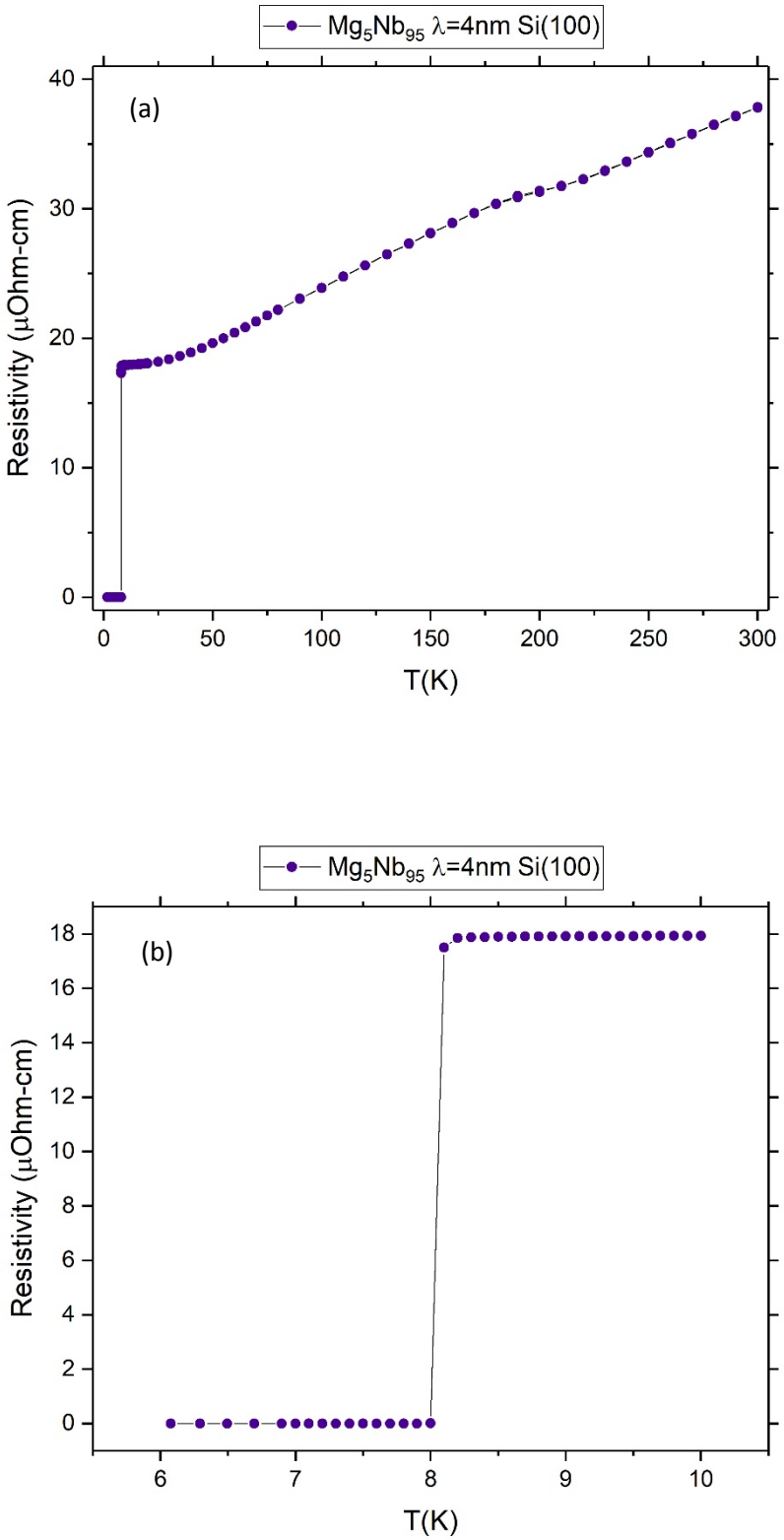

Figure 4.9: (a) Mg(0.2nm)Nb(3.8nm) film on Si(100). (b) Superconducting transition curve, T_c = 8.1K. Sputtered at Purdue.

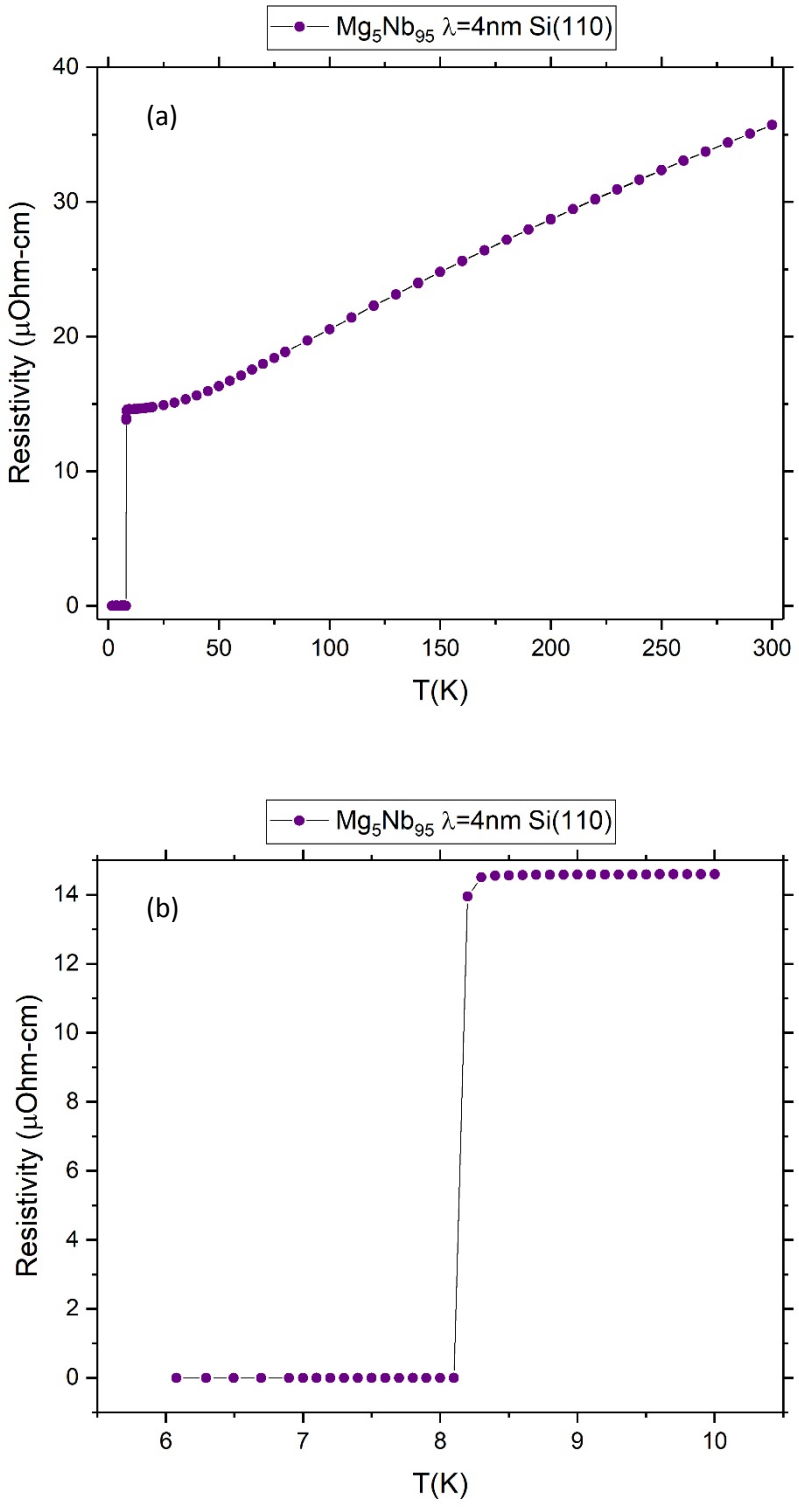

Figure 4.10: (a) Mg(0.2nm)Nb(3.8nm) film on Si(110). (b) Superconducting transition curve, T_c = 8.1K. Sputtered at Purdue.

As expected, the strange behavior seen in films sputtered on Si (111) substrate due to the conductivity of the substrate is seen for this film as well, Figure 4.11a. The transition is shown in detail in Figure 4.11b. The film on the SiO_2 substrate, Figure 4.12, displays behavior similar to the behavior seen for this film on the Si (100) and Si (110) substrates. As seen in Figure 4.12(b), the transition temperature is 8.16K for the Mg_5Nb_{95} film.

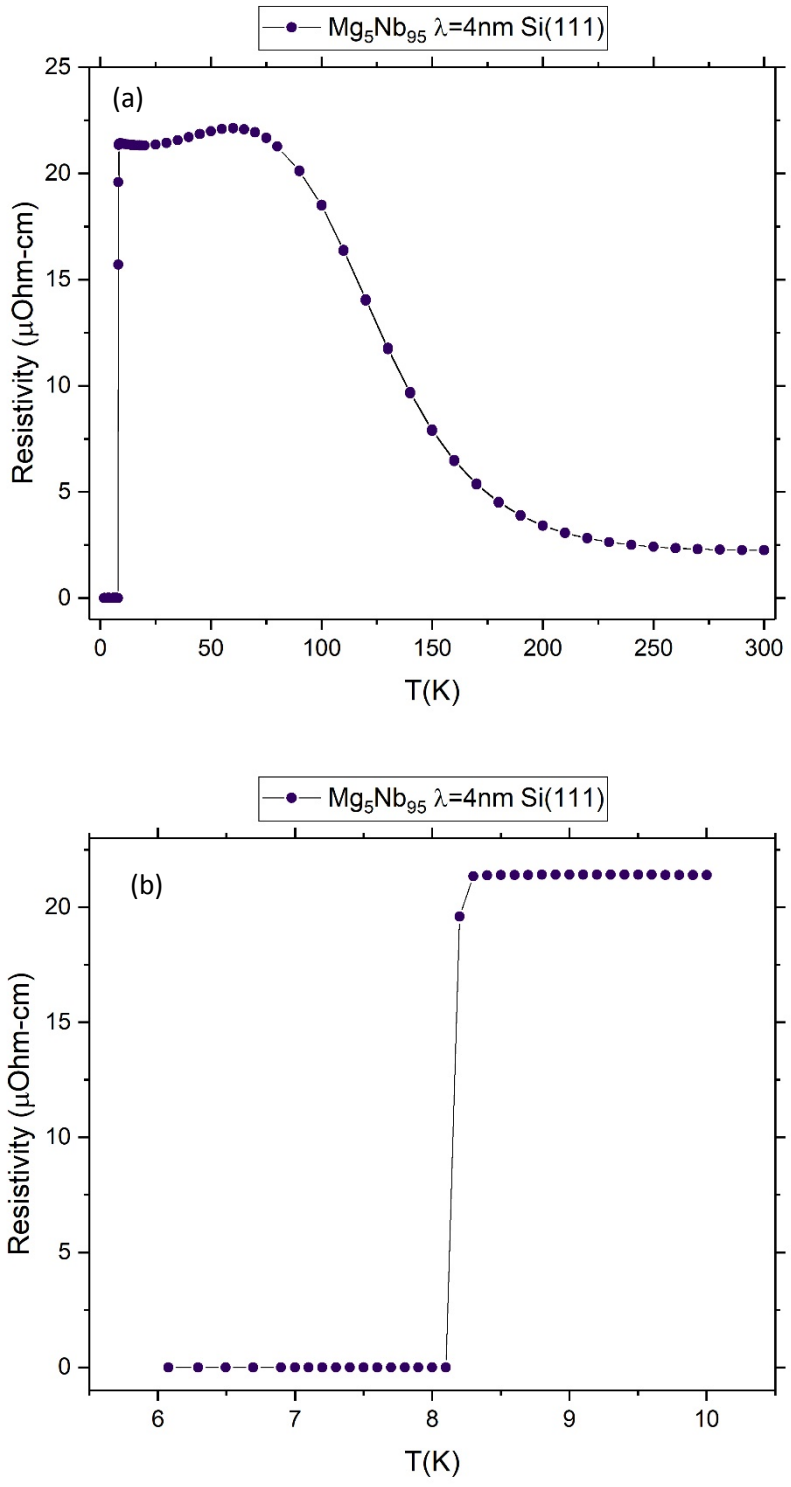

Figure 4.11: (a) Mg(0.2nm)Nb(3.8nm) film on Si(111). (b) Superconducting transition curve, T_c = 8.1K. Sputtered at Purdue.

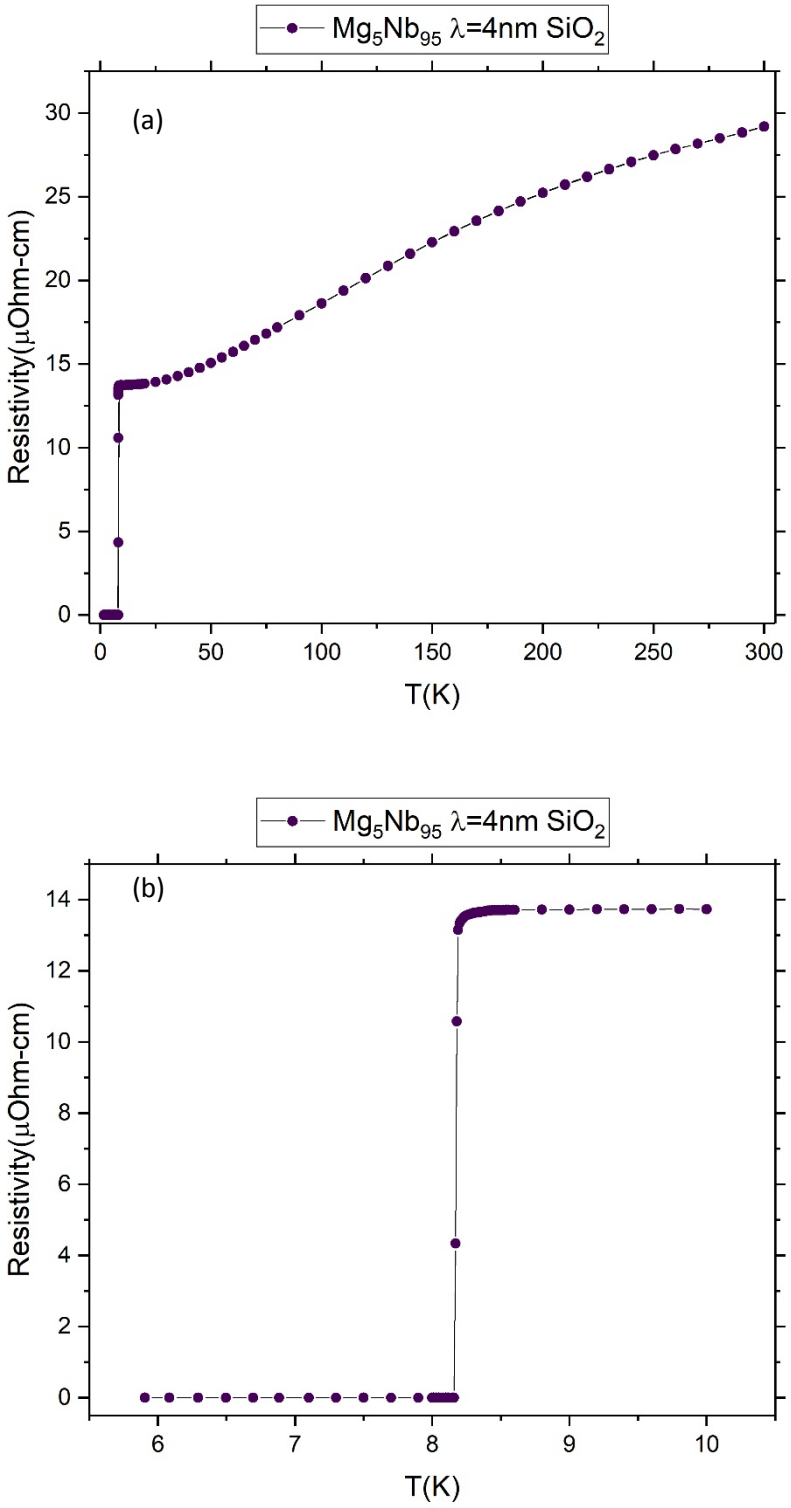

Figure 4.12: (a) Mg(0.2nm)Nb(3.8nm) film on SiO_2 . (b) Superconducting transition curve, T_c = 8.16K. Sputtered at Purdue.

Next, a comparison is presented of all film compositions sputtered at Purdue with transition temperatures above 1.7K on each of the substrates to highlight the consistency of the behaviors discussed previously. In Figure 4.13, a comparison is shown of the films on the Si(100) substrate near their transition temperatures. Figure 4.14 exhibits the transitions of the films on the Si(110) substrate, while Figures 4.15 and 4.16 show superconducting transitions of the films on the Si(111) and SiO_2 substrates respectively. The first film composition, starting on the right, in each comparison is Mg_5Nb_{95}.

The next film composition, moving towards the left, is $Mg_{15}Nb_{85}$, bilayer thickness 4nm, 15 bilayer repeats, and total thickness 63nm. It has a transition temperature of 7.65K. This T_c is a full degree higher than the transition temperature for the same film sputtered at TAMU (6.4K as reported previously). Looking at the film with composition $Mg_{20}Nb_{80}$ on all four substrates, bilayer thickness 6nm, 10 bilayer repeats, and total thickness 63nm, it can be seen that the transition temperature for this film is 7.14K. Continuing the trend of increasing Mg percent, moving to the left, the composition $Mg_{50}Nb_{50}$ is examined on each of the four substrates for bilayer thickness 10nm, 7 bilayer repeats, and total thickness 73nm, including the 3nm Nb cap. Figures 4.13-4.15 show that the transition temperature for this film is 5.36K on three of the substrates. The film on the SiO_2 substrate was marked as not good by the grower, who noted that it might be bad due to the targets possibly shorting out a few times during the sputter process. The film still had a transition, but it occurred at a lower temperature of 4.30K, Figure 4.16. The resistivity values were in an expected range and consistent across the substrates except for the film on the SiO_2 substrate which has a high resistivity (~300μOhm-cm prior to transition). Much like with the $Mg_{15}Nb_{85}$ film composition, the transition temperature of this film composition at 5.36K is a 1K higher than the T_c measured for the same composition sputtered at TAMU, 4.3K.

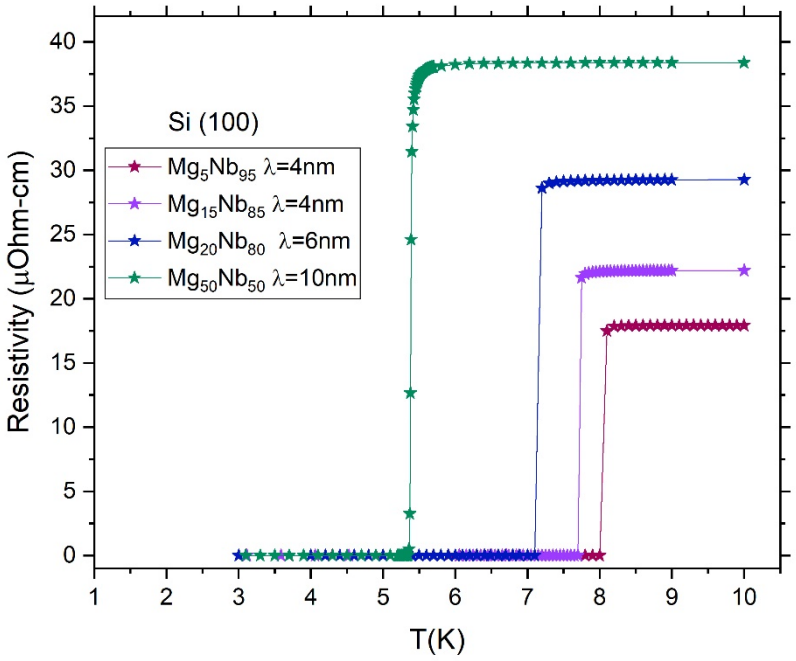

Figure 4.13: Superconducting transition curves for the four films grown on Si(100) substrate, sputtered at Purdue.

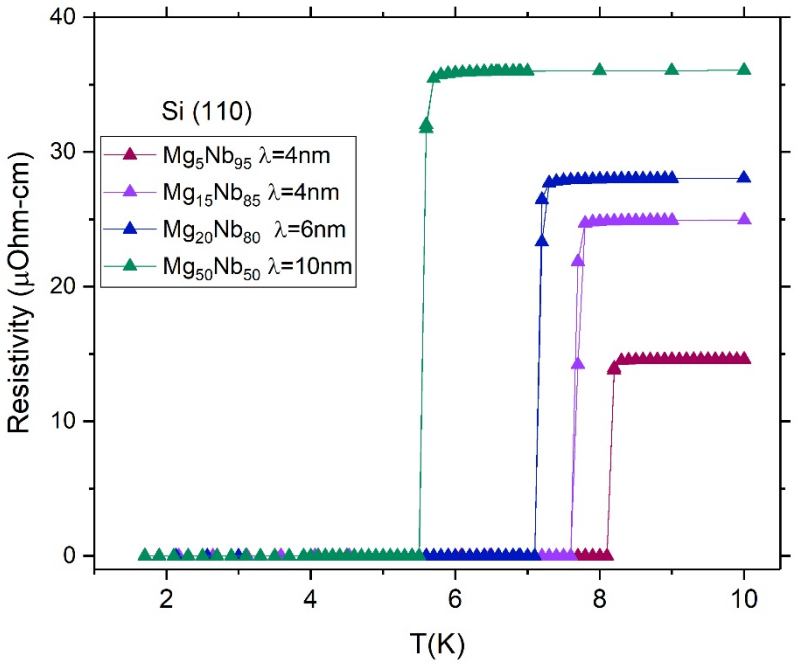

Figure 4.14: Superconducting transition curves for the four films grown on Si(110) substrate, sputtered at Purdue.

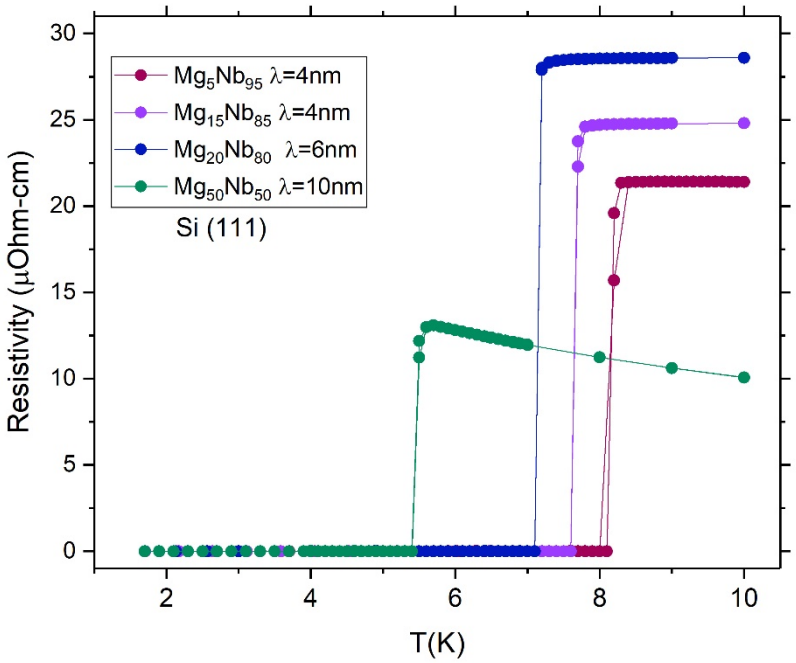

Figure 4.15: Superconducting transition curves for the four films grown on Si(111) substrate, sputtered at Purdue.

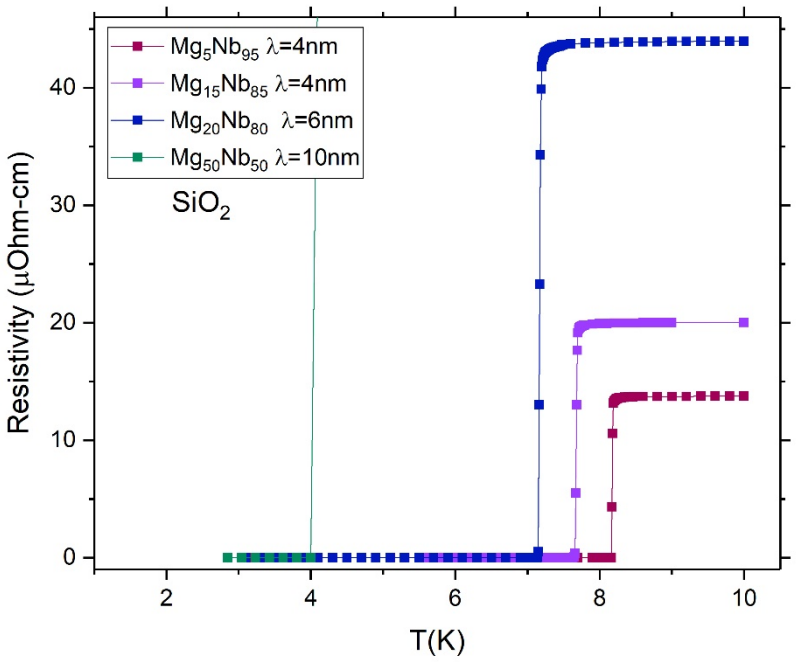

Figure 4.16: Superconducting transition curves for the four films grown on SiO_2 substrate, sputtered at Purdue.

There are obviously some differences in the equipment set-up at Purdue versus when it operated at TAMU, though these differences seemed to have resulted in an improvement in the film quality. The resistivity values are relatively consistent across each of the four substrates for all the films sputtered at Purdue. With the exception of the film composition $Mg_{50}Nb_{50}$ on the SiO_2 substrate, all of the films have reasonable resistivity values in an expected range based on prior proximity effect studies.

Moving on to the magnesium-rich films, the next film presented is composition $Mg_{80}Nb_{20}$, bilayer thickness 6nm, 10 bilayer repeats, and total thickness 63nm. When examined in the PPMS, the film's resistivity started to dip into a transition at 1.7K. Next, the film was measured in a DynaCool He3 system, and as expected, it transitioned just below 1.7K (Figure 4.17).

In comparison, the other two Mg rich films, $Mg_{85}Nb_{15}$ and $Mg_{95}Nb_5$, showed no evidence of a superconducting transition in the limit of the PPMS. The $Mg_{85}Nb_{15}$ was measured in the DynaCool system. A transition was seen around 0.45K (Figure 4.18), which was close to the limit of the DynaCool system. Attempts were made to measure the $Mg_{85}Nb_{15}$ and $Mg_{95}Nb_5$ films in a dilution refrigerator, however there were some equipment issues that did not allow for accurate measurement at this time.

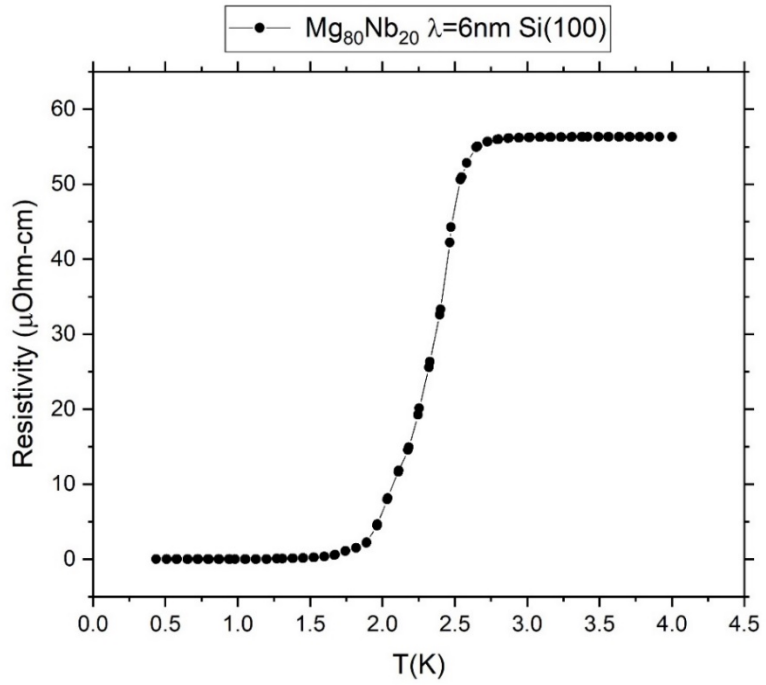

Figure 4.17: Mg(4.8nm)Nb(1.2nm) film on Si(100). Detail of the superconducting transition curve, T_c = 1.5K. Sputtered at Purdue.

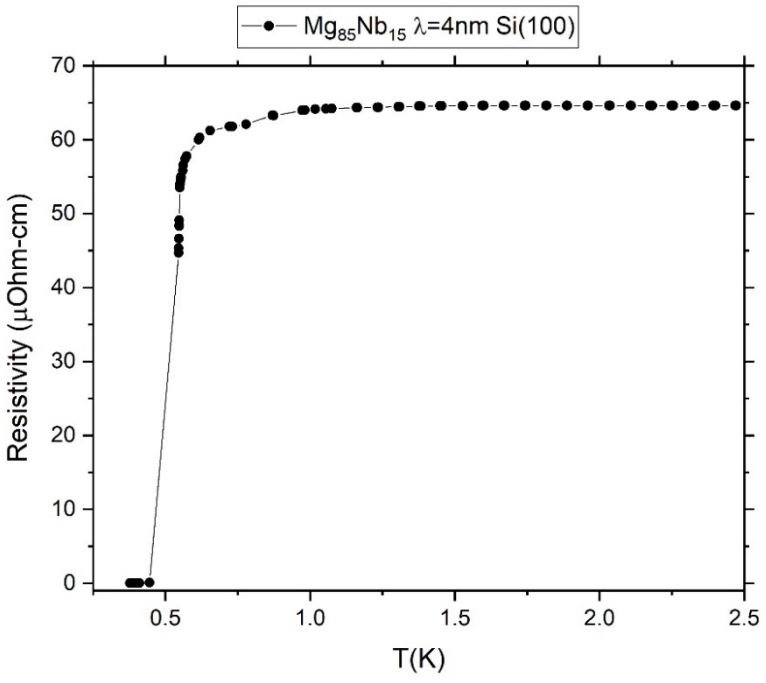

Figure 4.18: Mg(4.8nm)Nb(1.2nm) film on Si(100). Detail of the superconducting transition curve, $T_c \approx 0.45$K. Sputtered at Purdue.

As can be seen from the data presented so far, all of the films, regardless of resistivity values and high temperature behavior, have consistent transition temperatures across the four substrates, example as is shown in Figures 4.19 and 4.20. Therefore, as the substrate is not a factor in the T_c behavior, all subsequent films can be sputtered on only the SiO_2 and Si(100) substrates. From analyzing the resistivity data shown, it is clear that the samples sputtered at Purdue were of higher quality than those sputtered at TAMU with the same system.

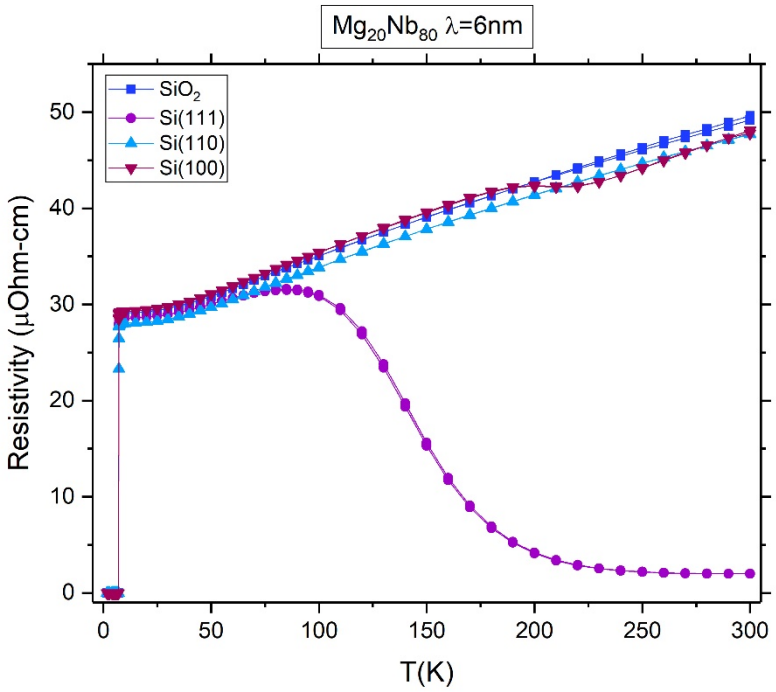

Figure 4.19: Comparison of the Mg(1.2nm)Nb(4.8nm) film, bilayer thickness 6nm and overall thickness 63nm, on all four substrates. Sputtered at Purdue.

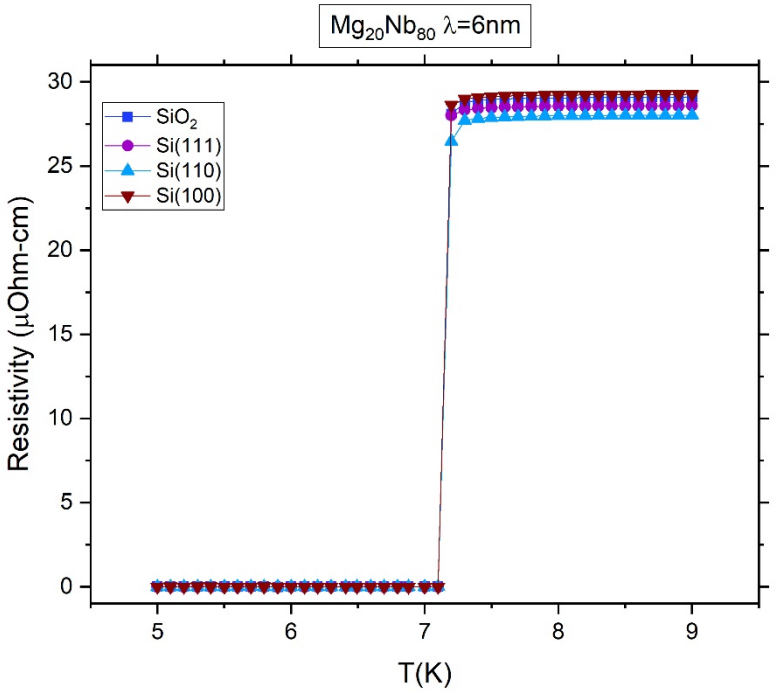

Figure 4.20: Comparison of the Mg(1.2nm)Nb(4.8nm) film, bilayer thickness 6nm and overall thickness 63nm, on all four substrates. Detail of the superconducting transition curve, T_c = 7.14K. Sputtered at Purdue.

4.1.3 Theoretical Comparison

The Cooper-de Gennes proximity effect model was chosen to apply to the films in this study as they fall into the Cooper limit: $d_N \ll \xi_N$ and $d_S \ll \xi_S$. The coherence length of niobium is 38nm [1] and the coherence length of magnesium [57] is 0.0245cm, both of which are much larger than the individual layer thicknesses used in this study, 0.2-5.0nm. Magnesium's coherence length comes from Reference 57. Thorp et al. measured magnesium down to 4mK. They did not observe a superconducting transition, but they believed that this does not completely rule out the possibility that T_c is greater than 4 mK, because the sample may have supercooled. To calculate the coherence length they assumed a T_c of 4mK, $\xi_0^* = 0.18(hv_F^*/k_B T_c)$.

Referring back to Chapter 1, in calculating the T_c values with the Cooper-de Gennes model, the following two formulas were used:

$$T_{cNS} = \frac{\Theta_D}{1.45} exp\left[\frac{-1}{\rho}\right] \quad (24)$$

$$\rho = [n(E_F)V]_{eff} = \frac{V_N n_N^2 d_N + V_S n_S^2 d_S}{n_N d_N + n_S d_S} \quad (25)$$

T_{cNS} is the critical temperature of the bilayer and ρ is the effective attraction parameter 'nV', $n_{S,N}$ is the density of states for the metals, and $V_{S,N}$ is the coupling constant.

The parameters used for calculating the transition temperature of each multilayer system studied are given in Table 4.1 (Refs. 57-60 were used to obtain the parameters). Note that the transition temperature for thin film niobium is used instead of bulk niobium. The bulk transition temperatures and the density of states values were used to calculate the coupling constant of each metal. Then the bulk density of states and calculated bulk coupling constants were used to determine the effective attraction parameter for each film. This value, along with the average Θ_D, was then used to calculate the T_c for each sample.

Table 4.2 lists all of the T_c values calculated and experimentally measured for the Mg/Nb multilayers. In Figure 4.21, a comparison is shown of the T_c's values from Table 4.2 as well as a few additional calculated values of films that were planned for measurement but were not sputtered due to equipment failures. The transition temperature is plotted as a function of the fractional percentage of niobium within the bilayer. The squares are the calculated values from the Cooper-de Gennes model. The spheres are the experimental values from the Purdue batch. And the triangles are the experimental values from the TAMU batch. The comparison shows good

agreement between the calculated values and the T_c's obtained from the films sputtered at Purdue. The difference between the calculated and experimental values (Purdue batch) is about $\pm$0.1-0.3K. One exception to this was the $Mg_{85}Nb_{15}$ film, which had a T_c about 0.4K difference from its calculated T_c. This film is right at the triple point and the possible crystal structure change in Nb could be a potential cause for the larger difference in T_c. The only film that was this close to the calculated value from the TAMU sputtered films was the $Mg_{70}Nb_{30}$ film. The calculated values represented by the solid squares are the films that should fall into the green area of the bi-phase diagram (Figure 3.2) where the materials are in their respective bulk crystal forms. The squares that are half filled vertically are the films that are expected to be in the blue region of the bi-phase diagram where both materials are bcc crystal structure. The square that is half-filled horizontally is for a film that at the triple point. The film that falls into the red region of the bi-phase diagram is represented by a square that is open in the center. Due to the fact that the Mg T_c is an assumed value, the film T_c values were calculated for Mg T_c=0 and plotted in Figure 4.22.

TABLE 4.1. Parameters for the two constituent layers of Mb_xNb_{100-x}.

Layer	T_c(K)	ξ(nm)	Θ_D(K)	$n(E_F)$(states $eV^{-1}atom^{-1}$)
Nb	8.3	38	276	0.91
Mg	0.004	2.45×10^5	403	0.275

TABLE 4.2. Superconducting Transition values for measured Mb_xNb_{100-x} films.

Film	λ (bilayer thickness)	T_c (K) (Calculated)	T_c (K) (Calculated) Mg T_c = 0	T_c (K) (Experiment)
TAMU:				
$Mg_{15}Nb_{85}$	4nm	7.59	7.22	~6.4
$Mg_{50}Nb_{50}$	10nm	5.23	3.78	~4.3
$Mg_{50}Nb_{50}$	4nm	5.23	3.78	~2.9
$Mg_{70}Nb_{30}$	6nm	2.79	1.13	~2.5
Purdue:				
Mg_5Nb_{95}	4nm	7.89	7.78	8.16
$Mg_{15}Nb_{85}$	4nm	7.59	7.22	7.65
$Mg_{20}Nb_{80}$	6nm	7.38	6.87	7.14
$Mg_{50}Nb_{50}$	10nm	5.23	3.78	5.36
$Mg_{80}Nb_{20}$	6nm	1.42	0.24	1.5
$Mg_{85}Nb_{15}$	4nm	0.82	0.049	~0.45
$Mg_{95}Nb_5$	4nm	0.081	$1.44x10^{-7}$	

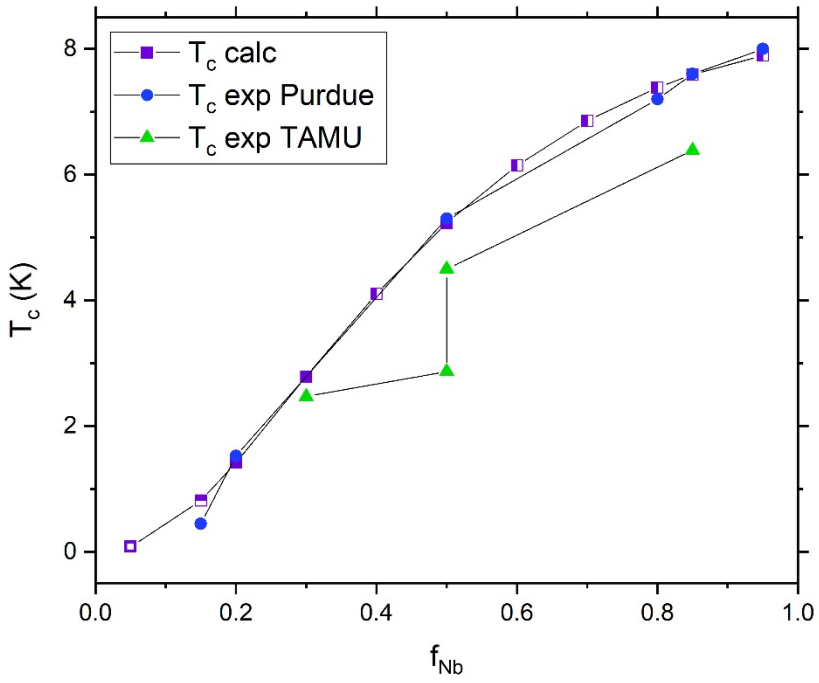

Figure 4.21: Critical temperature vs fractional percentage of Nb in the bilayer. Squares are calculated film T_c's and spheres are the T_c's obtained experimentally from the Purdue batch. Triangles are the T_c's obtained experimentally from the TAMU batch.

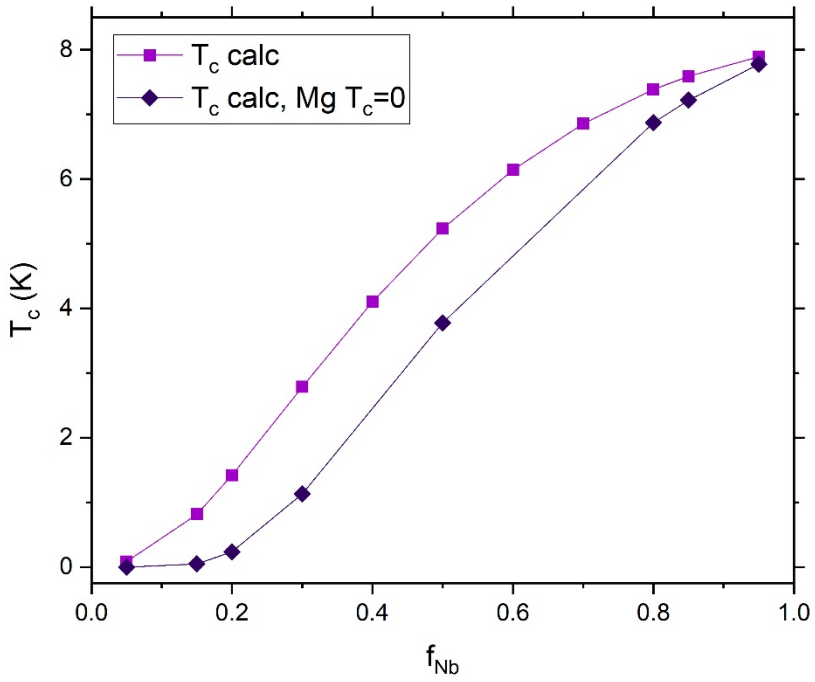

Figure 4.22: Critical temperature vs fractional percentage of Nb in the bilayer. Squares are calculated film T_c's using the values from Table 4.1. Diamonds are calculated using the same values with Mg's $T_c = 0$.

4.2 Upper Critical Field

The upper critical field was measured by the four-point probe technique in the Quantum Design PPMS. The change in the resistivity behavior with increasing perpendicular field was studied, as well as the temperature dependence of the upper critical field both parallel and perpendicular to the film's surface.

Superconducting transition curves are shown for different applied perpendicular magnetic fields for samples Mg_5Nb_{95} λ=4nm (Figure 4.23), $Mg_{15}Nb_{85}$ λ=4nm (Figure 4.24), $Mg_{20}Nb_{80}$ λ=6nm (Figure 4.25), $Mg_{50}Nb_{50}$ λ=10nm (Figure 4.26), and $Mg_{85}Nb_{15}$ λ=4nm (Figure 4.27).

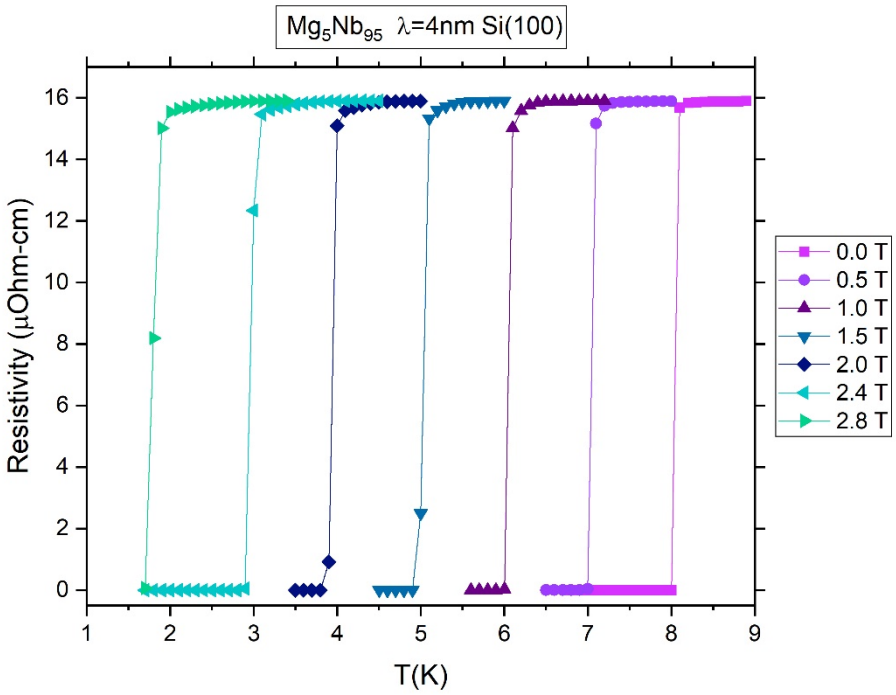

Figure 4.23: Transition curves for increasing perpendicular magnetic fields for sample Mg(0.2nm)/Nb(3.8nm) Film on Si (100).

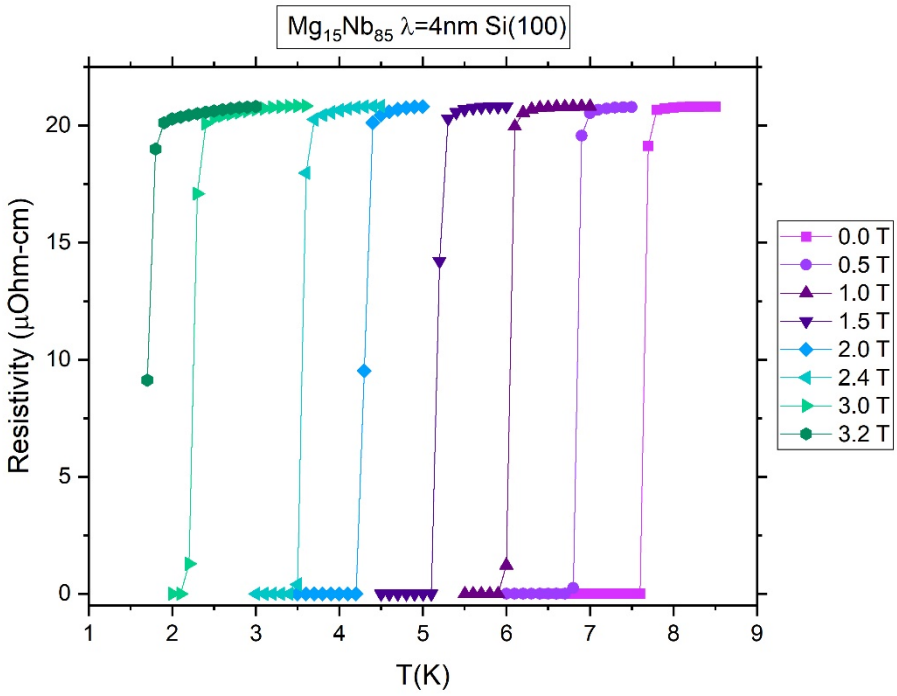

Figure 4.24: Transition curves for increasing perpendicular magnetic fields for sample Mg(0.6nm)/Nb(3.4nm) Film on Si (100).

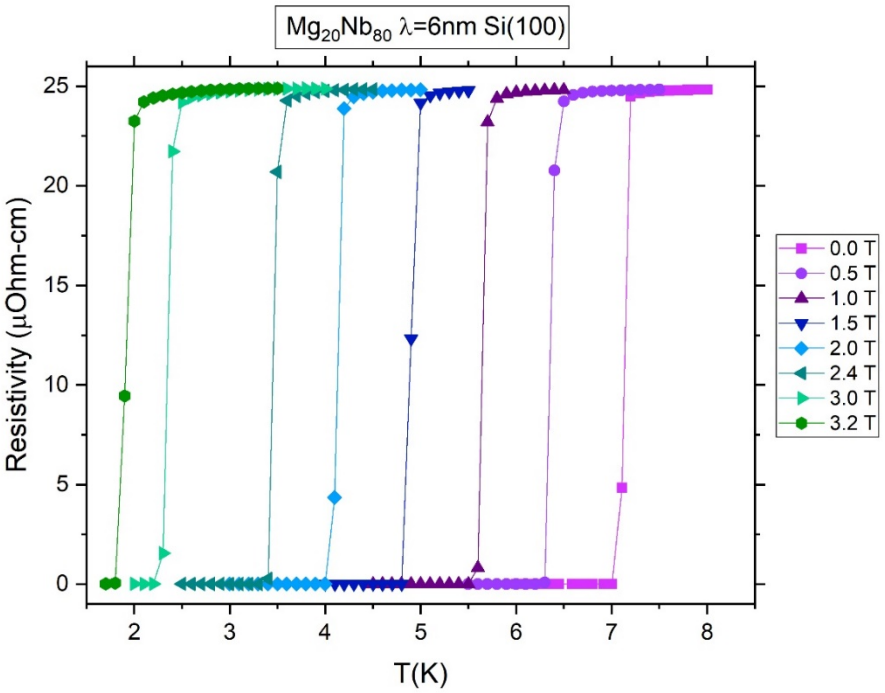

Figure 4.25: Transition curves for increasing perpendicular magnetic fields for sample Mg(1.2nm)/Nb(4.8nm) Film on Si (100).

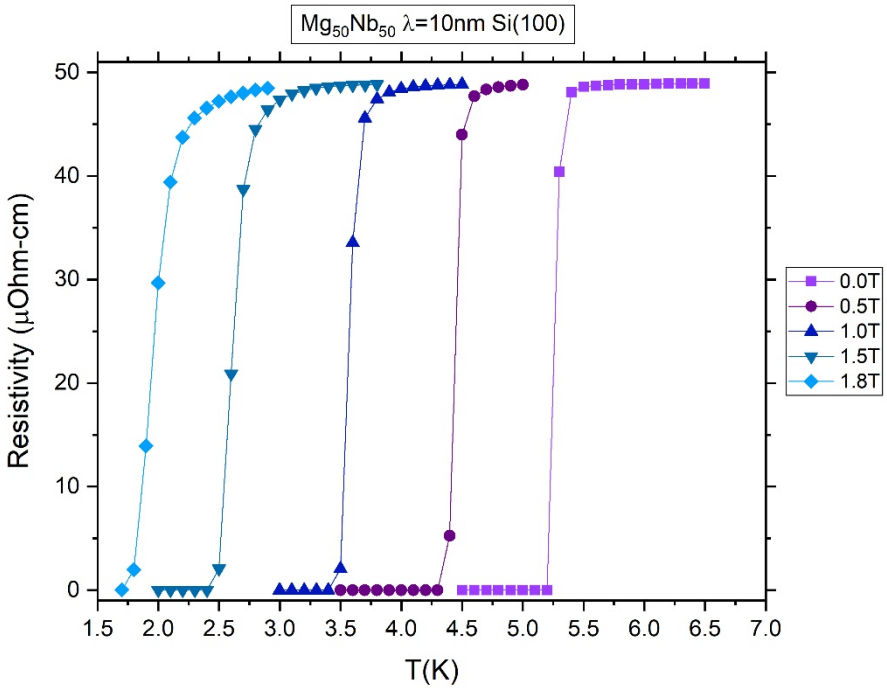

Figure 4.26: Transition curves for increasing perpendicular magnetic fields for sample Mg(5nm)/Nb(5nm) Film on Si(100).

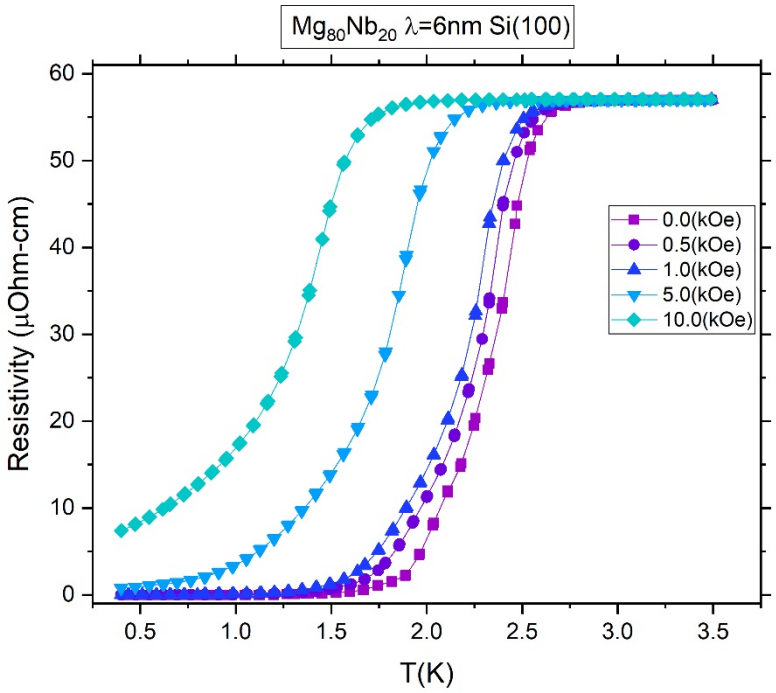

Figure 4.27: Transition curves for increasing perpendicular magnetic fields for sample Mg(4.8nm)/Nb(1.2nm) Film on Si(100).

The temperature dependencies of the parallel and perpendicular critical magnetic fields are presented for samples Mg_5Nb_{95} λ=4nm (Figure 4.28), $Mg_{15}Nb_{85}$ λ=4nm (Figure 4.29), $Mg_{20}Nb_{80}$ λ=6nm (Figure 4.30), and $Mg_{50}Nb_{50}$ λ=10nm (Figure 4.31).

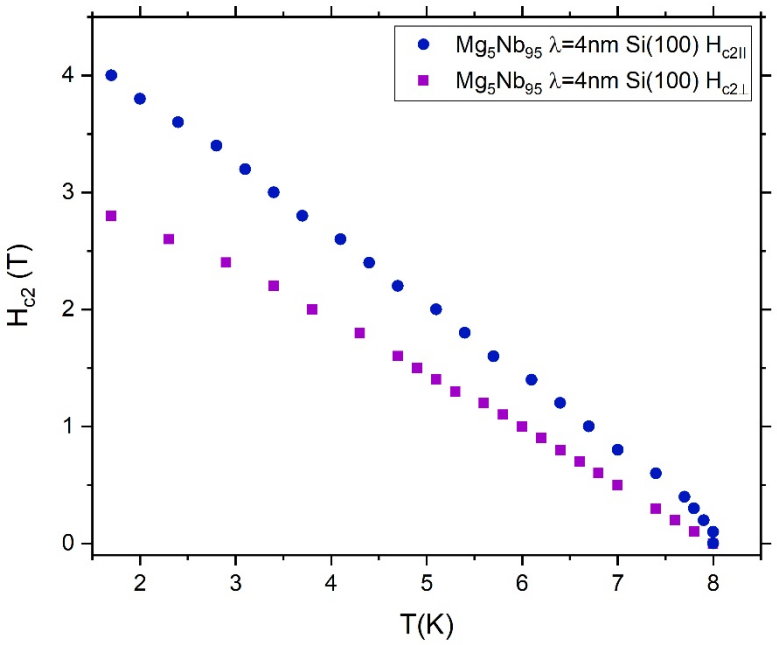

Figure 4.28: Perpendicular (squares) and parallel (spheres) critical fields for the sample Mg(0.2nm)/Nb(3.8nm) Film on Si(100).

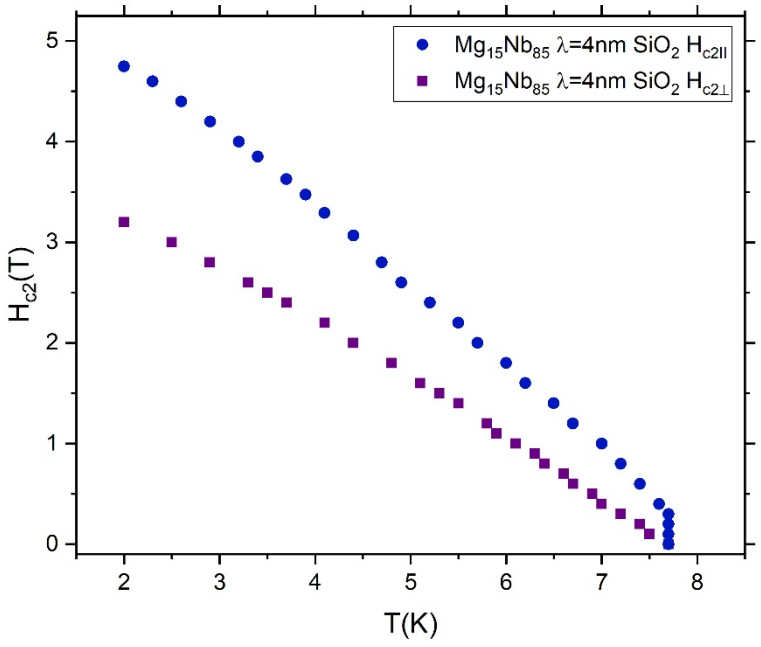

Figure 4.29: Perpendicular (squares) and parallel (spheres) critical fields for the sample Mg(0.6nm)/Nb(3.4nm) Film on SiO_2.

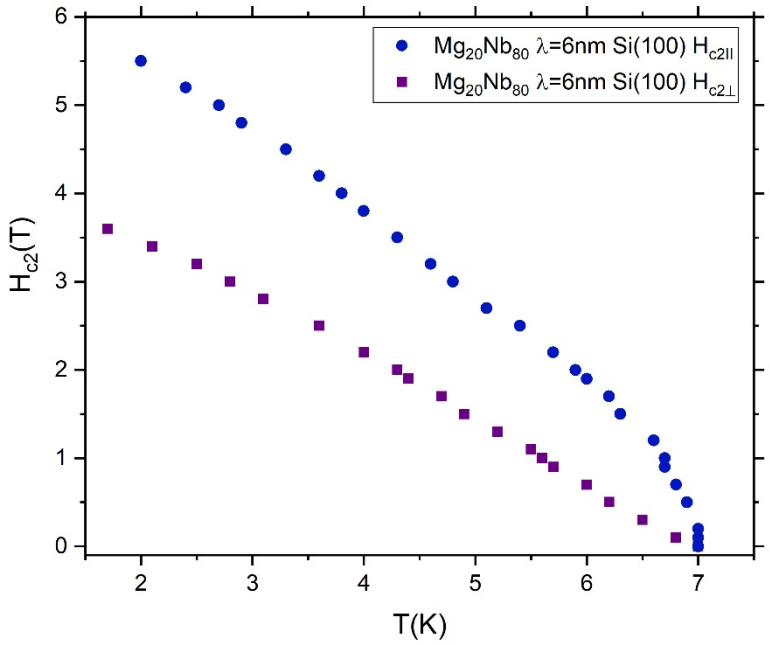

Figure 4.30: Perpendicular (squares) and parallel (spheres) critical fields for the sample Mg(1.2nm)/Nb(4.8nm) Film on Si(100).

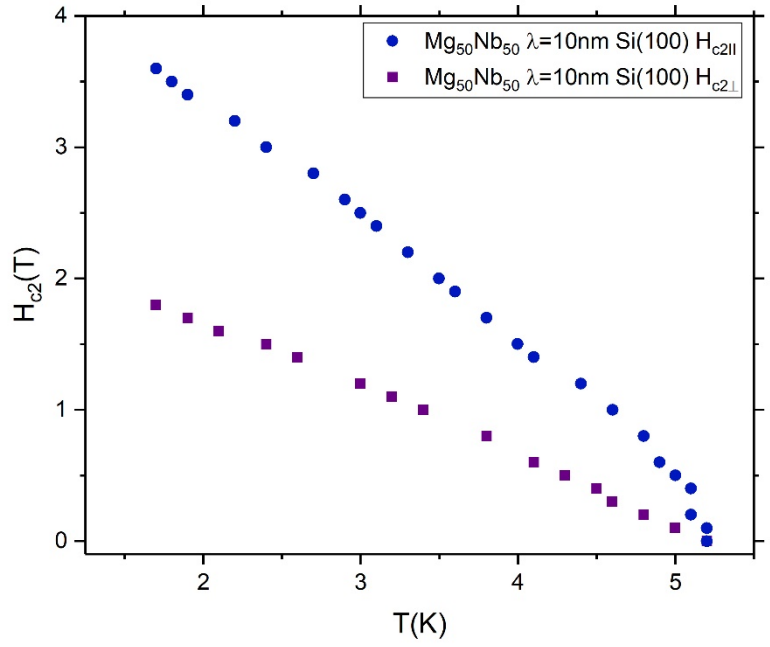

Figure 4.31: Perpendicular (squares) and parallel (spheres) critical fields for the sample Mg(5nm)/Nb(5nm) Film on Si(100).

The angular dependence of the upper critical field was analyzed for each of the films that had transitions above 1.7K using a rotational puck holder. The results are shown in Figures 4.32-4.35. The 3D behavior was plotted using the formula [32, 33, 36]

$$H_{c2}(T,\theta) = \frac{H_{c2\perp}(T)}{[(m/M)\sin^2(\theta) + \cos^2\theta]^{1/2}}$$

where,

$$\frac{M}{m} = \left[\frac{H_{c2\parallel}(T)}{H_{c2\perp}(T)}\right]^2$$

and where θ is the angle between the field direction and the sample normal.

The 2D case was plotted using the formulas developed by Tinkham [35]

$$\left|\frac{H_{c2}(T,\theta)\cos\theta}{H_{c2\perp}(T)}\right| + \left[\frac{H_{c2}(T,\theta)\sin\theta}{H_{c2\parallel}(T)}\right]^2 = 1 \quad .$$

The results point to the films having a 2D nature at low temperatures. When the $\xi_\perp \gg d_N$, the thickness of the normal metal layer, the superconducting layers are coupled, and a 3D behavior is expected. If, instead, $\xi_\perp \ll d_N$ the superconducting layers are decoupled, and a 2D behavior is predicted if the coherence length of the superconducting material, ξ_S, is smaller than its thickness d_S. The theories predict that the crossover occurs when the perpendicular coherence length is approximately equal to the separation between the superconducting layers.

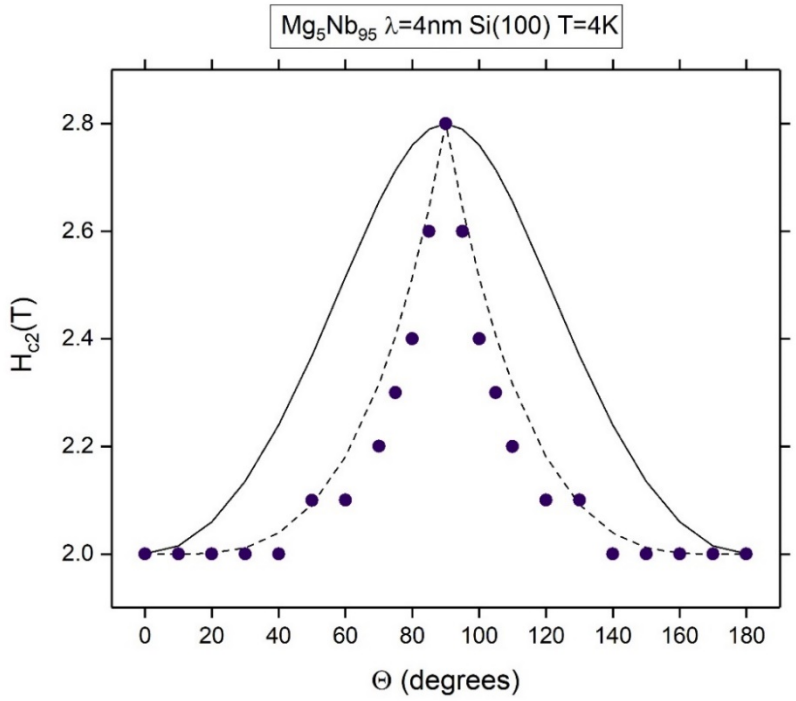

Figure 4.32: Angular dependence of the H_{c2} at 4.0K for the Mg(0.2nm)/Nb(3.8nm) film on Si (100). The solid line is a theoretical fit to the 3D equation for $H_{c2}(\Theta)$. The dashed line is the theoretical fit to the 2D expression.

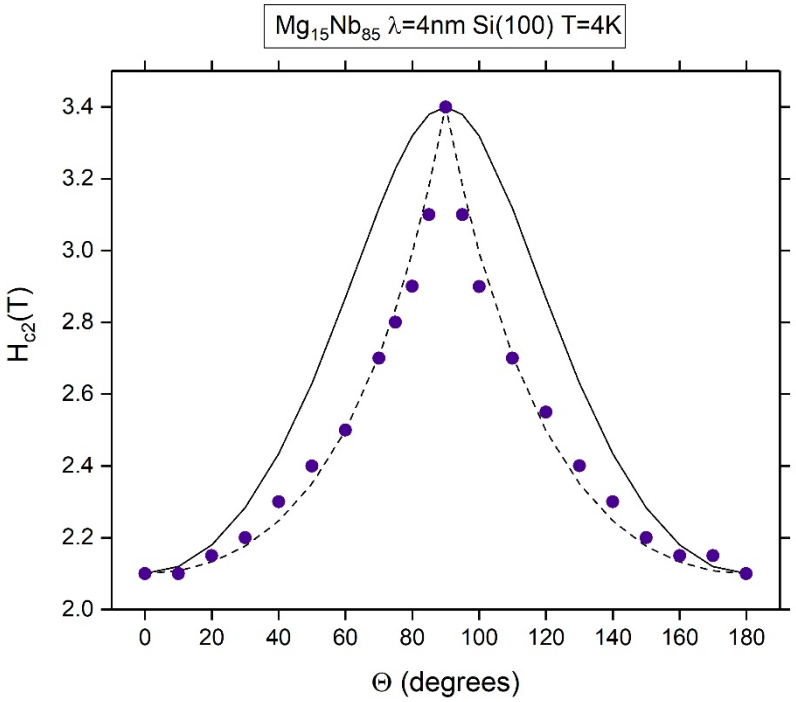

Figure 4.33: Angular dependence of the H_{c2} at 4.0K for sample Mg(0.6nm)/Nb(3.4nm) Film on Si (100). The solid line is a theoretical fit to the 3D equation for $H_{c2}(\Theta)$.The dashed line is the theoretical fit to the 2D expression.

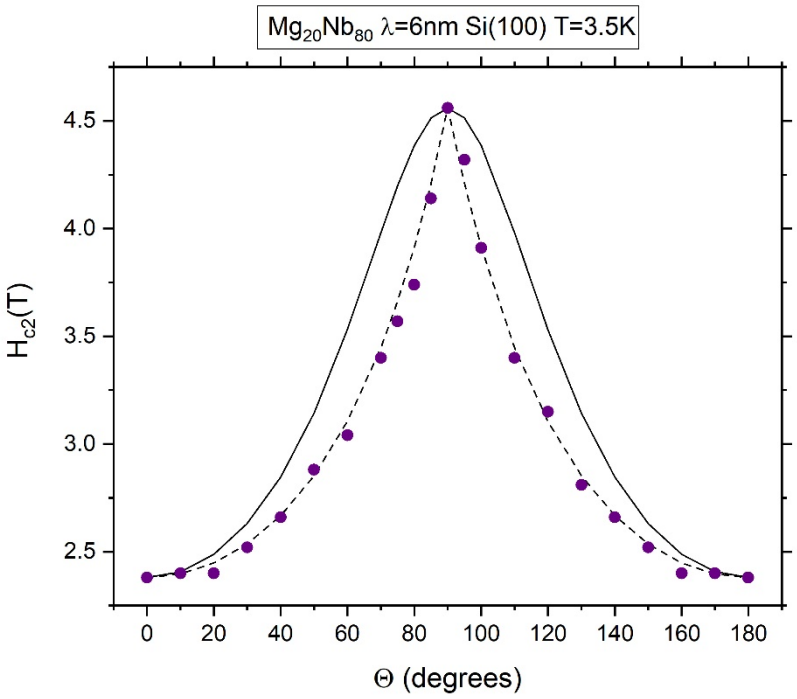

Figure 4.34: Angular dependence of the H_{c2} at 3.5K for sample Mg(1.2nm)/Nb(4.8nm) Film on Si (100). The solid line is a theoretical fit to the 3D equation for $H_{c2}(\Theta)$. The dashed line is the theoretical fit to the 2D expression.

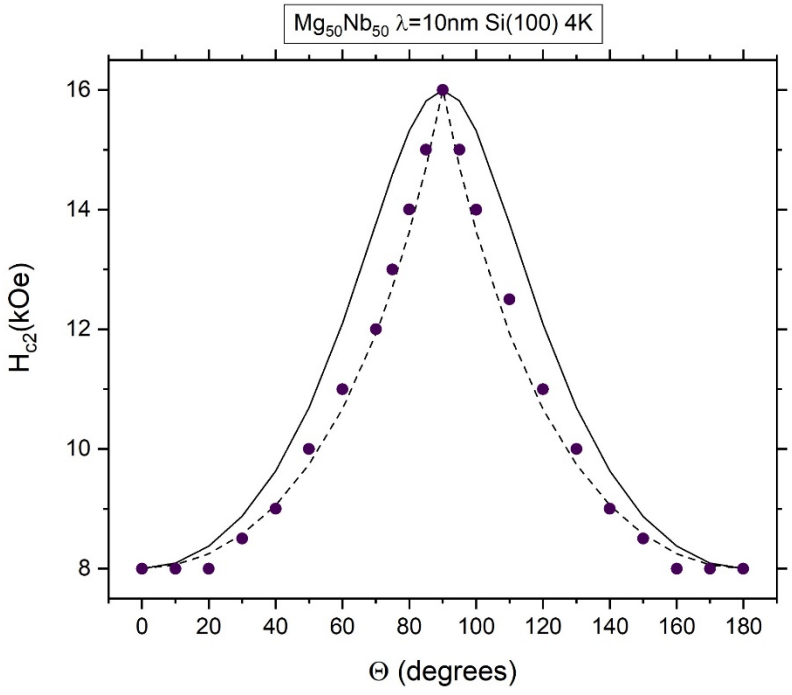

Figure 4.35: Angular dependence of the H_{c2} at 4.0 K for sample Mg(5nm)/Nb(5nm) Film on Si (100). The solid line is a theoretical fit to the 3D equation for $H_{c2}(\Theta)$. The dashed line is the theoretical fit to the 2D expression.

5. CONCLUSIONS AND FUTURE WORK[**††]

5.1 Conclusions

In this study, the proximity effect of Mg/Nb multilayer films grown on four separate substrates (Si(100), Si(110), Si(111), and SiO_2) was carefully studied. Each film was sputtered onto all four substrates simultaneously by magnetron sputtering. X-ray diffraction scans were performed on the Purdue sample batch and compared to the XRD patterns of Reference 19. The XRD data alone is not enough to say with certainty if the films fall into the expected regions of the bi-phase diagram, though it appears at least some of them do. Further studies, mentioned below, will be needed to fully determine the crystal structure of the multilayer films and discover if metastable phases are present. Additional studies will also be needed to determine if the crystal structure plays a part in the proximity effect.

The influence of the proximity effect on the transition temperature and upper critical field were studied through resistivity and magnetoresistance measurements. Both parallel and perpendicular upper critical field were studied as well as the angular dependence.

The resistivity measurements had varying results based on the sputter batch. The experimental results were compared with the theoretical values, calculated using the Cooper-de Gennes proximity effect theory. The sputter batch made at TAMU was the least consistent. Three of the four films that had superconducting transitions in the range of the Quantum Design PPMS (i.e.,

[**] Part of this section, including Figure 5.3, is reprinted with permission from "High strength Mg/Nb nanolayer composites" by B. Ham and X. Zhang, Mater. Scien. Engin.: A, 528 (2011) 2028, Copyright 2013 by Elsevier LTD.
[††] Part of this section is reprinted, including Figure 5.4, with permission from "Tailoring the formation of metastable Mg through interfacial engineering: A phase stability analysis" by A. Junkaew, et al., CALPHAD, 2440 (2014) 145, Copyright 2013 by Elsevier LTD.

above 1.7K) had T_c's quite a bit different from the theoretical calculations. Only the $Mg_{70}Nb_{30}$ film was close to its calculated value. However, all of the films from the Purdue sputter batch were in good agreement with the theoretical T_c's. These films also had more consistency in the resistance values across the substrates. Another determination was that the substrate on which the film was deposited had no effect on the superconducting transition.

For the upper critical field study, only measurements from the Purdue sputter batch were presented, due to the inconsistency of the TAMU sample batch. The change in the superconducting transition as the field was increased, in the perpendicular direction, was presented for several of the films. Parallel and perpendicular fields were compared across four of the seven films, while the other three films (T_c below the 1.7K range of PPMS) were measured with other equipment and full field scans could not be obtained. Only perpendicular field sweeps were obtained for the $Mg_{80}Nb_{20}$, which was measured with a Dynacool He3 system. No field scans were acquired for the $Mg_{85}Nb_{15}$ and $Mg_{95}Nb_5$ films. For the four films measured with the PPMS above 1.7K, the angular dependence of the upper critical field was investigated at temperatures a few degrees below T_c. Comparing the results with the theoretical calculations for 3D and 2D upper critical field, it was found that all four films matched quite well with the 2D expression for the upper critical field.

5.2 Future Work

5.2.1 Additional Proximity Effect Studies

Due to multiple equipment malfunctions recently, the research group who sputtered the films were unable to send additional films for further study. Once their equipment is functioning again, or if another group is found that can produce the films with equal or better quality, there are additional measurements that would be interesting to pursue, as they could provide further insights

to what has been learned from this study. One such experiment would be the examination of the proximity effect on the transition temperature when holding either the Mg or Nb thickness constant and changing the thickness of the other. Such a study would give a better understanding of the effect of the thickness on the T_c. Measurements of the critical field would also need to be done on those films. Graphs of calculated values for a study of the effect on the transition temperature while holding either the Mg or Nb thickness constant are shown in Figures 5.1 and 5.2. The points plotted were calculated using the Cooper-de Gennes proximity effect model and show the expected behavior of the thickness dependence of T_c. This experiment could help to further understand the proximity effect in this system of films.

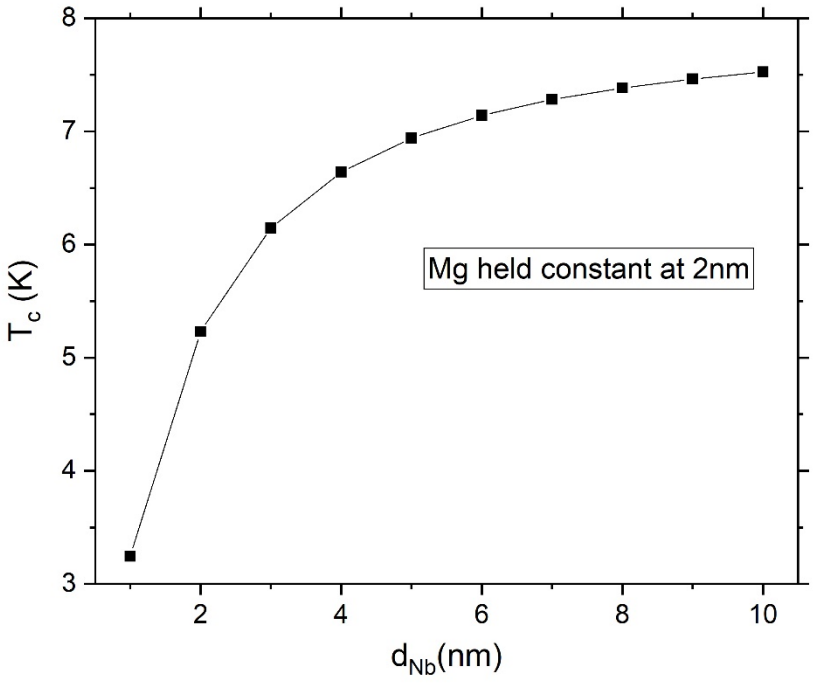

Figure 5.1: Calculated dependence of critical temperature on thickness of Nb in the bilayer while holding the Mg thickness constant at 2nm.

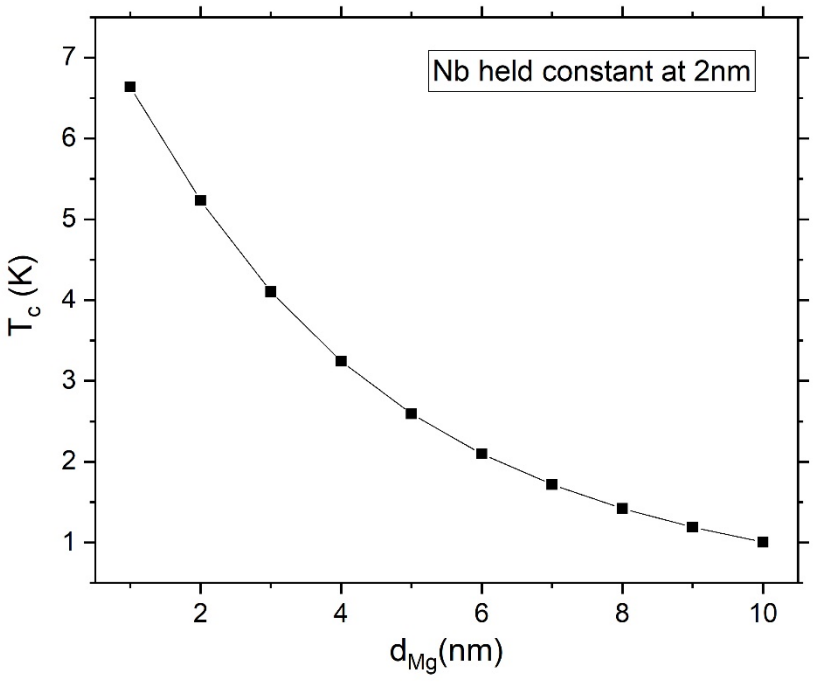

Figure 5.2: Calculated dependence of critical temperature on thickness of Mg in the bilayer while holding Nb constant at 2nm.

5.2.2 TEM

Further examination of the crystal structure of the multilayer films is needed. Besides additional XRD measurements, another way to characterize the crystal structure of the films and to check for coherent interfaces is through transmission electron microscopy (TEM) imaging. For a thorough investigation, high resolution TEM (HRTEM) images, diffraction patterns, and bright and dark field patterns would need to be acquired, as well as Fast Fourier Transform (FFT) images for films measured in this study. A. Junkaew, B. Ham, et al. [29, 61] obtained TEM images for their films when first investigating the Mg/Nb multilayer system. Figures 5.3 and 5.4 show results from their study as an example of what could be expected from TEM measurements of films from

the current study. As can be seen in Figure 5.3, a bright field cross-sectional TEM image of Mg 5nm/Nb 5nm multilayers reveals the discrete layer interface between Mg and Nb. The inserted selected area diffraction (SAD) pattern in Figure 5.3a shows strong Mg (0002) and Nb (110) fiber textures. A cross-sectional TEM micrograph of Mg/Nb 100 nm multilayer, Figure 5.3b, shows weaker texture of the same orientations and a clear interface. Chemically sharp interfaces were also observed in the same specimen as shown in a cross-sectional FESEM micrograph captured in the backscattering mode in Figure 5.3c.

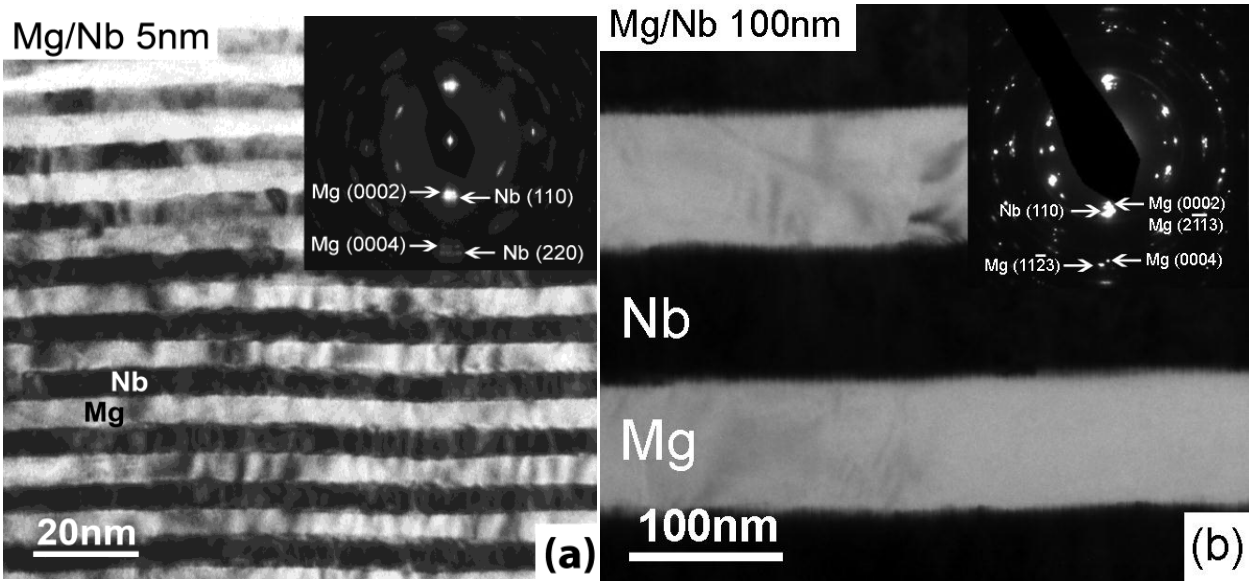

Figure 5.3. (a) Bright field cross-sectional TEM micrograph and inserted select area diffraction pattern of as-deposited Mg/Nb 5 nm multilayers showing orientation relationship between hcp Mg {0002} and bcc Nb {110}. (b) Cross-sectional TEM image and diffraction pattern of as-deposited Mg/Nb 100nm multilayer films showing discrete layer interface. (c) Cross-sectional FESEM micrograph of Mg/Nb 100 nm multilayers taken in backscattering mode confirms chemically sharp interface in the same specimen. Reprinted with permission from [61].

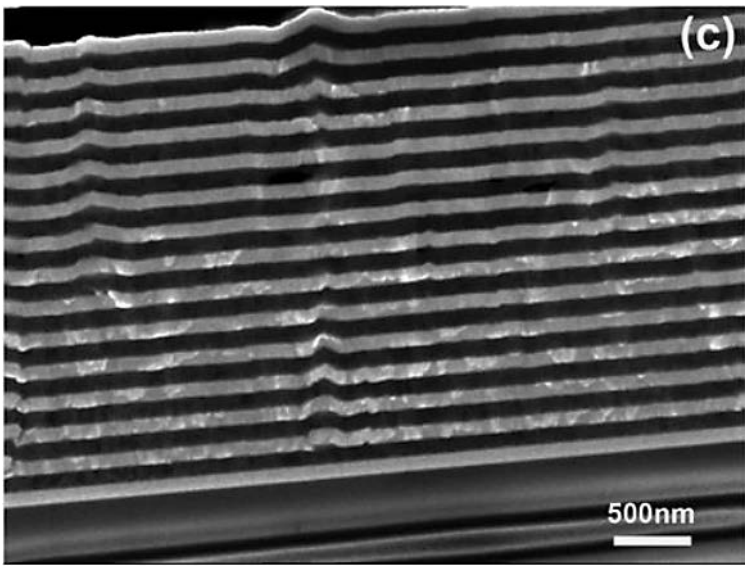

Figure 5.3. Continued

Mg 1.5 nm/Nb 0.5 nm multilayers shown in Fig. 5.4(a) show that a metastable bcc Mg structure formed and the interface was coherent between bcc Mg and bcc Nb. This is consistent with the prediction based on the calculated bi-phase diagram. Mg appears to grow epitaxially on Nb as confirmed by the fast fourier transforms (FFTs) inserts of the image examined along Nb $[\bar{1}11]$ zone axis; also, the layer interface was chemically-abrupt. In the second case, HRTEM micrograph of Mg 1.8 nm/Nb 0.2 nm multilayers (Fig. 5.4(b)) shows that hcp Nb has grown epitaxially on hcp Mg. The orientation of crystals was confirmed by the inserted FFT of the micrograph examined along hcp $[2\bar{1}10]$ zone axis. HRTEM micrograph and FFT patterns of Mg 5nm/Nb 5nm multilayers in (Fig. 5.4(c)) show growth of bcc Nb on hcp Mg.

TEM measurements, as well as additional XRD work, will allow future researchers to gain more insight into the bi-phase diagram of the Mg/Nb system, as well as to better define the boundary lines and aid in further understanding the metastable structures observed.

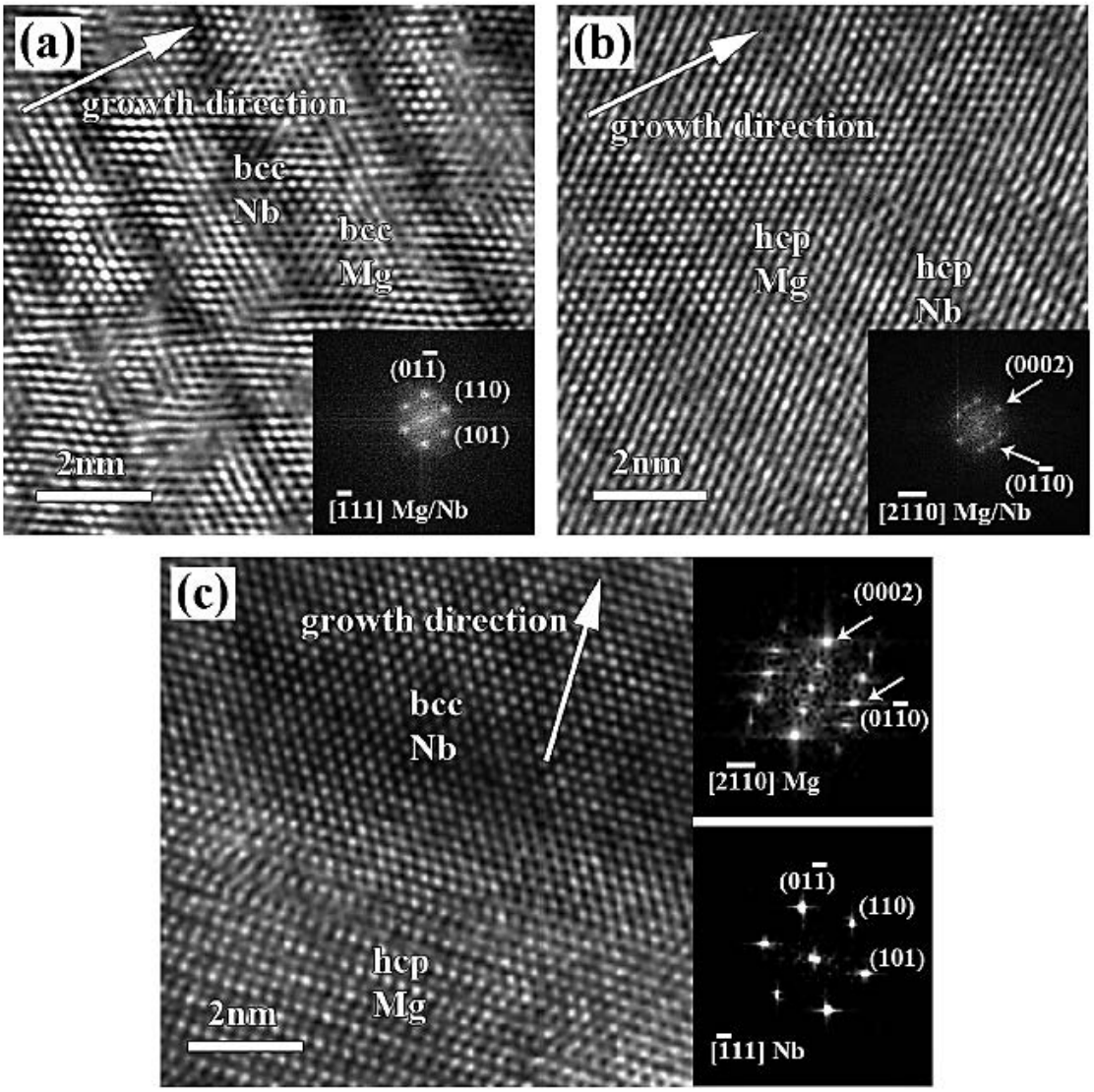

Figure 5.4: (a) High resolution TEM image and corresponding fast Fourier transform (FFT) pattern of Mg 1.5 nm/Nb 0.5 nm multilayers, (b) HRTEM micrograph of Mg 1.8 nm/Nb 0.2 nm multilayers and correlated FFT pattern, and (c) HRTEM micrograph of Mg 5 nm/Nb 5 nm multilayers and correlated FFT patterns in Mg and Nb. Reprinted with permission from [29].

REFERENCES

1. C. Kittel, *Introduction to Solid State Physics*. John Wiley and Sons, Inc. Hoboken, New Jersey (1986).

2. N.W. Ashcroft and N.D. Mermin, *Solid State Physics*. Thomson Learning, Inc. Independence, Kentucky (1976).

3. A.C. Rose-Innes and E.H. Rhoderick, *Introduction to Superconductivity*. Elsevier Science Inc. Tarrytown, New York (1978).

4. P.G. De Gennes, *Superconductivity of Metals and Alloys*. W.A. Benjamin Inc. New York, New York (1966)

5. C. P. Poole Jr., H. A. Farach, R. J. Creswick, R. Prozorov, *Superconductivity 2nd Edition*. Elsevier, Ltd. Oxford, UK (2007)

6. R.D. Parks, *Superconductivity Vol. 2*, Marcel Dekker Inc. New York, New York (1969)

7. W. Meissner, R. Ochsenfeld, Naturwiss. 21 (1933) 787.

8. Wikipedia, *Meissner Effect*, Retrieved on March 5, 2017 from https://en.wikipedia.org/wiki/Meissner_effect

9. SlidePlayer, *Scuola di Dottorato in Ingegneria Industriale*, Retrieved on March 16, 2017 from http://slideplayer.com/slide/5023729/16/images/44/Type+II+superconductors.jpg

10. Starts with a Bang, *Weekend Diversion: Lift me up Quantum Style*, Retrieved March 6, 2017 from http://scienceblogs.com/startswithabang/files/2011/10/vortex.png

11. J. Bardeen, L.N. Cooper, and J.R. Schrieffer, Phys. Rev. 108 (1957) 1175.

12. Subedi, M., Superconductivity and Cooper Pairs. Himalayan Physics, 6, 104-107 (2017).

13. P.G. De Gennes, Rev. Mod. Phys. 36 (1964) 225.

14. P.G. De Gennes, E. Guyon, Phys. Letters 3 (1963) 168.

15. N.R. Werthamer, Phys. Rev. 132 (1963) 2440.

16. H.J. Fink, M. Sheikholeslam, A. Gilbert, J.P. Laheurte, J.P. Romagnan, et al., Phys. Rev. B 14 (1976) 1052

17. Y. Tanaka and M. Tsukada, Phys. Rev. B 37 (1988) 5087

18. P.C. van Son, H. van Kempen, and P. Wyder, Phys. Rev. Letters 59 (1987) 2226

19. G. Bergmann, Phys. Rev. B 72 (2005) 134505

20. W.P. Lowe and T. H. Geballe, Phys. Rev. B 29 (1984) 4961.

21. R. Banerjee, P. Vasa, G.B. Thompson, H.L. Fraser, P. Ayyub, Solid State Commun. 127 (2003) 349

22. O. Bourgeois, A. Frydman, and R.C. Dynes, Phys. Rev. B 68 (2003) 092509

23. I. Banerjee, Q.S. Yang, C.M. Falco, and I. Schuller, Solid State Commun. 41 (1982) 805

24. P. R. Broussard, Phys. Rev. B 43 (1991) 2783

25. P. R. Broussard and D. Mael, Phys. Rev. B 40 (1989) 2321

26. C.J. Kircher, Phys. Rev. 168 (1968) 437

27. J. Aarts, J. Meiresonne, H. Sprey, W. Maj, and P. Zagwijn, Phys. Rev. B 41 (1990) 4739

28. J.C. Li, W. Liu, and Q. Jiang, Acta Mater 53 (2005) 1067

29. A. Junkaew, B. Ham, X. Zhang, and R. Arroyave, CALPHAD 2440 (2014) 145.

30. A. Junkaew, B. Ham, X. Zhang, and R. Arroyave, Comput. Mater. Sci. 108 (2015) 212.

31. L. Cooper, Phys. Rev. Lett. 6 (1961) 689.

32. P.R. Broussard and T.H. Geballe, Phys. Rev. B 35 (1987) 1664

33. P.R. Broussard and T.H. Geballe, Phys. Rev. B 37 (1988) 60

34. D. Neerinck, K. Temst, H. Vanderstraeten, C. Van Haesendonck, Y. Bruynseraede, et al., J. Phys. Condes. Matter 2 (1990) 6287

35. M. Tinkham, Phys. Rev. 129 (1963) 2413

36. C. Cirillo, C. Attanasio, L. Maritato, L.V. Mercaldo, S.L. Prischepa, and M. Salvato, J. Low Temp. Phys. 130 (2003) 509

37. K.R. Biagi, V.G. Kogan, and J.R. Clem, Phys. Rev. B 32 (1985) 7165

38. C. Uher, J. L. Cohn, I. K. Schuller, Phys. Rev. B. 34 (1986) 4906

39. C. S. L. Chun, G.G. Zheng, J.L. Vicent, and I. K. Schuller, Phys. Rev. B 29 (1984) 4915

40. G. Verbanck, C.D. Potter, V. Melushko, R. Schad, V.V. Moshchalkov, and Y. Bruynseraede, Phys. Rev. B 57 (1998) 6029

41. C. Ciuhu and A. Lodder, Phys. Rev. B 64 (2001) 224526

42. Y. Kuwasawa, Y. Kamata, T. Watanabe, S. Nakano and S. Matuba, Physica C 190 (1992) 333

43. Y. Kuwasawa, U. Hayano, T. Tosaka, S. Nakano and S. Matuba, Physica C 165 (1990) 173

44. Angstrom Sciences, *Magnetron Sputtering*, Retrieved on August 15, 2017 from https://www.angstromsciences.com/magnetron-sputtering-deposition

45. Wasa, Kiyotaka. *Handbook of Sputter Deposition Technology : Fundamentals and Applications for Functional Thin Films, Nano-Materials and MEMS*, Elsevier Science Inc. Oxford, UK (2014)

46. Diederik Depla, Stijn Mahieu. (2008) *Reactive Sputter Deposition*, Springer. New York, New York

47. Rigaku Mechatronics Co.,LTD *Sputtering Systems* Retrieved September 1, 2017 from http://en.rigaku-mechatronics.com/case/sputtering-systems.html

48. D. Manova, J.W. Gerlach, and S. Mandl, Materials 3 (2010) 4109

49. Nanometal Group, *Equipment* Retrieved August 2, 2017 from https://sites.google.com/site/xzhanggroup/equipment

50. Quantum Design PPMS User Manual

51. A. Shimamoto, K. Yamashita, H. Inoue, S. Yang, M. Iwata and N. Ike, J. Press. Vess. Tech. 135 (2013) 021501

52. Encyclopedia Britannica, *Crystal,* Retrieved on August 2, 2017 from https://www.britannica.com/science/crystal/images-videos

53. C. Suryanarayana, M. G. Norton. *X-Ray Diffraction A Practical Approach*, Plenum Press, Springer. New York, New York (1998)

54. V. Ramaswamy, *Characterization of Polycrystalline Catalytic Materials using Powder X-Ray Diffraction*, Alpha Science International Ltd., Oxford, UK (2016)

55. Bragg WL. The diffraction of short electromagnetic waves by a crystal. Proceedings of the Cambridge Philosophical Society, 17 (1913) 43.

56. D. Henry, N. Eby, J. Goodge, David Mogk (2016) Geochemical Instrumentation and Analysis, *X-Ray Reflection in Accordance with Bragg's Law*. Retrieved October 28, 2017 from https://serc.carleton.edu/research_education/geochemsheets/BraggsLaw.html

57. T.L. Thorp, B.B. Triplett, W.D. Brewer, M.L. Cohen, N.E. Phillips, et.al. J. Low Temp. Phys. 3 (1970) 589

58. W.M. Lomer and W.E. Gardner Progr. Mater. Science 14 (1969) 141

59. Knowledge Door, *Debye Temperature*, Retrieved on August 3, 2017 from http://www.knowledgedoor.com/2/elements_handbook/debye_temperature.html

60. W.L. McMillan, Phys. Rev. 167 (1968) 331

61. B. Ham and X. Zhang, Materials Science and Engineering A 528 (2011) 2028